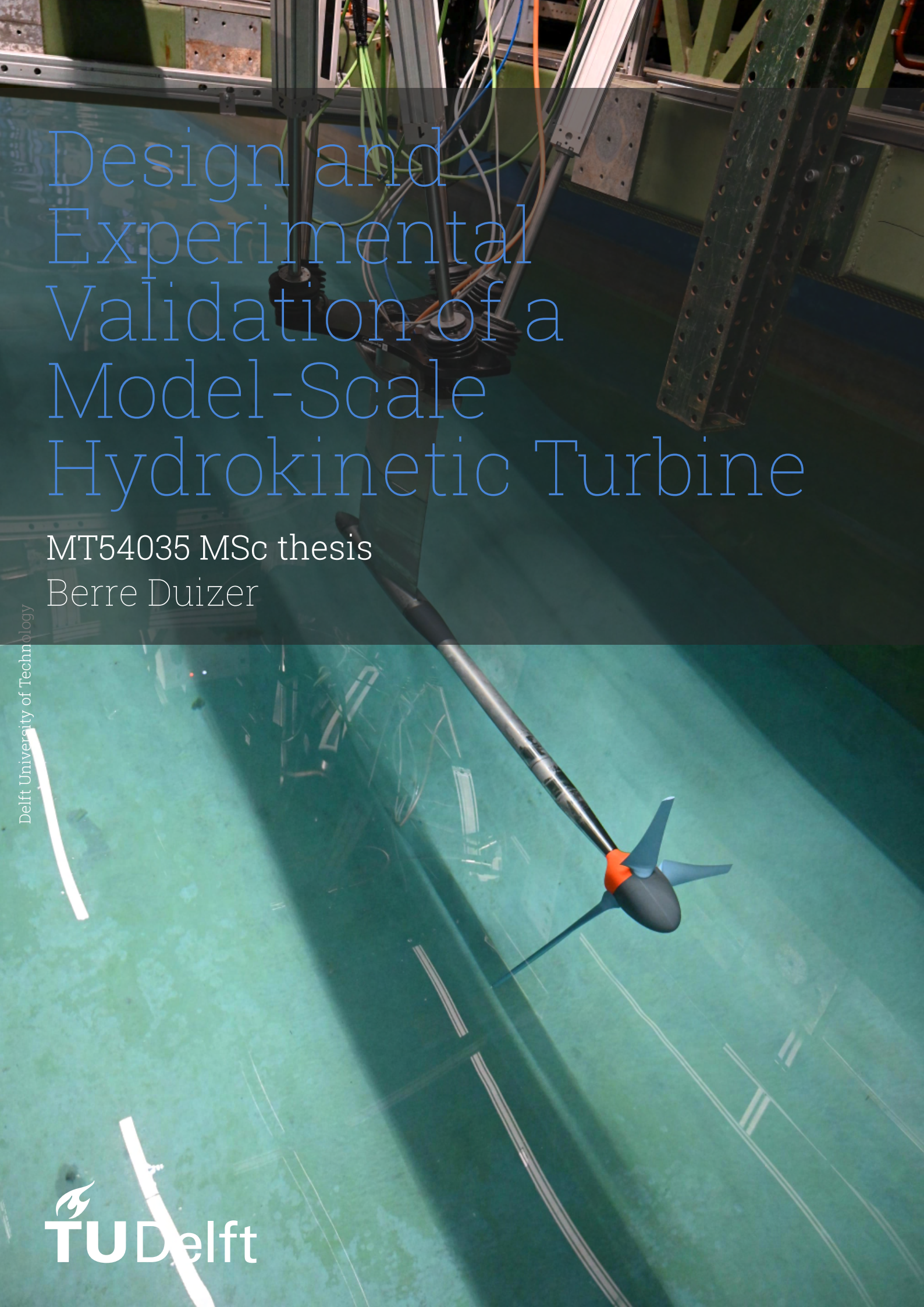

Design and Experimental Validation of a Model-Scale Hydrokinetic Turbine

MT54035 MSc thesis

Berre Duizer

Delft University of Technology

TU Delft

Thesis for the degree of MSc in Marine Technology
in the specialisation of Ship Design and Ship Hydromechanics

Design and Experimental Validation of a Model-Scale Hydrokinetic Turbine

by

Berre Duizer

Performed at
TU Delft

This thesis MT.24/25/057.M. is classified as confidential in accordance with the general conditions for projects performed by TU Delft.

to be defended publicly on Friday 19th of September, 2025 at 2:00 PM.

Thesis exam committee
Chair/Responsible Professor: Dr. D. Fiscaletti
Staff Member: Dr. G. Jacobi
Staff Member: Dr. G. Ricard
Staff Member: Dr. A.J.L.L. Buchner

Author details
Student number: 5401801

Cover: Hydrokinetic turbine in TU Delft towing tank.
An electronic version of this thesis is available at `http://repository.tudelft.nl/`.

TU Delft

Preface

This thesis concludes my Master's degree in Marine Technology at TU Delft. It has been a rewarding journey, both technically and personally, and I am grateful to everyone who supported me along the way.

First of all, I would like to sincerely thank my supervisor, Daniele Fiscaletti. His guidance throughout the project was invaluable as he was always available for questions, quick to provide support when I needed it, and full of ideas that helped me with the research. I also wish to thank Guillaume Ricard and Gunnar Jacobi for their assistance and constructive feedback during this project. Then I also want to thank Abel-John Buchner for sharing his insights and being part of the exam committee. Working with them, and with everyone involved, made the process not only educational but also enjoyable. Designing, building, and testing a turbine was a challenging subject, but I also enjoyed it a lot.

I am also grateful to all the people who assisted with the experiments and the manufacturing of the turbine parts. A special thanks to Peter Poot, Frits Sterk Ton Veer and Pascal Taudin Chabot. Their time, effort, and willingness to help ensured that everything ran smoothly and made this research possible. Finally, I want to thank my family and my girlfriend for their constant encouragement and support, which kept me motivated throughout this project.

Furthermore, for this thesis I have used generative AI to:

- Create parts of the code in Spyder for calculations and analysis performed in this thesis
- Obtain inspiration for the overall structure of the report
- Improve the grammar, style, layout, and/or spelling of the text

In all cases I have reviewed and corrected the work and remain fully responsible for the content of the report.

Berre Duizer
Delft, September 2025

Abstract

Hydrokinetic turbines are increasingly seen as a promising way to generate renewable energy from tidal and river currents, offering high energy density without the ecological costs of dams or large-scale hydropower. Placing turbines close to the free surface allows them to access higher flow velocities and thus greater power potential, but it also makes them more vulnerable to wave-current interactions. Horizontal-Axis Hydrokinetic Turbines (HAHTs) have shown strong potential at full scale, but their development and testing at laboratory scale are still constrained by scaling effects, limited structural data, and an incomplete understanding of unsteady wave-induced loads. Moreover, only a handful of studies document the detailed design process of model-scale turbines, and even fewer investigate the structural performance of 3D-printed blades. To help close these gaps, this thesis presents the design, construction, and experimental testing of a 0.74 m diameter model-scale HAHT developed at the TU Delft.

The design process combined actuator disc theory and Blade Element Momentum Theory (BEMT) to define the blade geometry and expected operational loads. A modular hub concept with adjustable pitch and interchangeable blades was developed, allowing rapid prototyping and cost-efficient manufacturing. The blades were produced using 3D printing, and static tests confirmed that they withstood thrust forces up to 441 N without failure. The nacelle was conceptually designed but not constructed; instead, the existing gondola system was employed for testing.

Experiments in the towing tank under steady and wave conditions showed good agreement with BEMT predictions once Reynolds numbers exceeded 1.1×10^5. The turbine achieved a maximum power coefficient of $C_p \approx 0.44$, comparable to other model-scale studies. Under wave forcing, mean power remained stable, but unsteady loads dominated, with torque oscillations over 100% of the mean. Tip deflections of up to 33 mm were observed during operation, far exceeding static predictions, which underscores the role of deformation in dynamic response.

Overall, the study shows that it is possible to build a reliable and affordable model turbine using 3D printing and modular design, and to validate it experimentally. The results not only demonstrate the feasibility of this approach, but also underline how strongly turbine performance is shaped by Reynolds number effects, wave-current interaction, and fluid-structure dynamics. This makes the turbine a practical platform for future research and development in hydrokinetic energy.

Contents

List of Figures

List of Tables

Nomenclature

Abbreviations

Abbreviation	Definition
BEM	Blade Element Momentum
CFD	Computational Fluid Dynamics
Cp	Power Coefficient
Ct	Thrust Coefficient
Cq	Torque Coefficient
Fr	Froude Number
NACA	National Advisory Committee for Aeronautics
HAHT	Horizontal Axis Hydrokinetic Turbine
NREL	National Renewable Energy Laboratory
ppr	Pulses Per Revolution
PIV	Particle Image Velocimetry
PLA	Polylactic Acid
Re	Reynolds Number
RPM	rotations per minute
SPIV	Stereoscopic Particle Image Velocimetry
TSR	Tip Speed Ratio
UNFCCC	United Nations Framework Convention on Climate Change
ODE	Ordinary Differential Equation

Symbols

Symbol	Definition	Unit
A	Cross sectional area of the channel	[m^2]
A_ω	Wave amplitude	[m]
A_t	Rotor swept area of the turbine (πR^2)	[m^2]
a	Axial induction factor	[-]
a'	Tangential induction factor	[-]
C_p	Power Coefficient	[-]
C_t	Thrust Coefficient	[-]
c	Chord length	[m]
c/R	Chord-to-radius ratio	[-]
d	Beam point load distance	[m]
D	Rotor diameter	[m]
D_n	Nacelle diameter	[m]
E	Modulus of Elasticity	[Pa]
Fr	Froude Number	[-]
F	Force	[N]
g	Gravitational acceleration	[m/s^2]
$\vec{g}$	Gravitational acceleration vector	[m/s^2]
h	Water depth	[m]
I	Second moment of area	[m^4]
k	Wave number	[m]
L_1	Beam length	[m]

Symbol	Definition	Unit
L_n	Nacelle length	[m]
M	Bending moment	[Nm]
N	Number of blades	[-]
P	Pressure	[Pa]
$P_{turbine}$	Mechanical power	[W]
$P_{available}$	Available power [W]	
Q	Torque	[Nm]
R	Rotor radius	[m]
R_b	Radius for the bolts	[m]
r_i	Vertical lever arm of bolt i relative to the neutral axis	[m]
r_j	Lever arm of bolt j used in the summation $\sum r_j^2$	[m]
Re	Reynolds Number	[-]
t	Thickness	[m]
T	Thrust force	[N]
T_ω	Wave period	[s]
U_∞	Free-stream velocity	[m/s]
U_t	Tangential velocity	[m/s]
U_{rel}	Relative velocity	[m/s]
V	Characteristic velocity	[m/s]
W	True (induced) relative velocity experienced by the blade	[m/s]
$\vec{u}$	Velocity vector	[m/s]
r	Radial position along blade	[m]
r/R	Normalized radial position	[-]
z	Hub depth	[m]
λ	Wave length	[m]
σ	Solidity	[-]
ϵ	Blockage ratio	[-]
Ω	Rotational speed (turbine)	[rad/s]
ω	angular frequency (waves)	[rad/s]
α	Angle of attack	[deg]
β	Pitch angle	[deg]
μ	Dynamic viscosity	[Ns/m^2]
ν	Kinematic viscosity (μ/ρ)	[m^2/s]
ϕ	Flow angle	[deg]
ϕ_p	Velocity potential	[m^2/s]
Φ	Amplitude function	[-]
ρ	Water density	[kg/m^3]
θ	Blade twist angle	[deg]
η	Wave elevation	[m]
ε	Wave steepness	[-]
∇	gradient	[-]

1

Introduction and motivation

Climate change mitigation is a defining global challenge of the 21st century, and the transition to renewable energy is critical for reducing greenhouse gas emissions. The United Nations Framework Convention on Climate Change (UNFCCC) underscores the need for expanding renewable technologies, including ocean and riverine energy, to meet the Paris Agreement targets (UNFCCC 2024).

Hydropower is a well-established renewable energy source, accounting for approximately 14.3% of the world's electricity production as of 2023 (REN21 2024). However, large-scale hydropower projects often require dams and reservoirs, which can have significant environmental and social impacts (Yuce et al. 2015). To address these challenges, modern hydrokinetic turbines offer a promising alternative by harnessing the kinetic energy of flowing water without the need for large-scale infrastructure. Unlike conventional hydropower, these systems operate in natural water currents, reducing environmental impact while maintaining high energy potential (Adcock et al. 2020).

Hydrokinetic turbines have diverse applications, including tidal currents (Neill et al. 2018b; Neill et al. 2018a), river currents (Khan et al. 2007), ocean streams, and even as regenerative propellers on ships or other flowing water systems. They combine high efficiency (Ozturk et al. 2009) with scalability. In addition, the high energy density and predictability of resources such as tides (Yuce et al. 2015; Multon 2012) provide significant potential to strengthen energy security (Gordon et al. 2023).

Global tidal stream is estimated to produce between 150 TWh/year (Byrne et al. 2019) and 800 TWh/year (Yuce et al. 2015), exceeding the United Kingdom's annual electricity consumption (Byrne et al. 2019). Worldwide, tidal energy potential reaches approximately $8,800$ TWh/year (Yuce et al. 2015).

Since 2010, the European marine energy industry has deployed 30.2 MW of tidal stream capacity, with 11.5 MW currently operational in European waters (EurObserv'ER 2022). The United Kingdom remains a leader in tidal energy, with over 10 GW of estimated tidal capacity, representing roughly 50% of Europe's total (Byrne et al. 2019). The European Union aims to reach 100 GW of marine energy capacity, including tidal and wave energy, by 2050, which could supply around 10% of Europe's electricity needs (EurObserv'ER 2022).

With growing deployment of tidal energy projects worldwide, hydrokinetic turbines have become a key technology to scale marine energy production. Among turbine designs, horizontal-axis hydrokinetic turbines (HAHTs) have emerged as the leading choice for tidal energy conversion (Ouro et al. 2022). HAHTs have already proven their commercial viability through successful large-scale projects. One notable example is the MeyGen project in Scotland (SIMEC Atlantis Energy 2024), which is one of the largest tidal energy projects in the world. With an installed capacity of 6 MW in its first phase and a total potential of 398 MW, MeyGen's HAHTs have collectively generated over 68 GWh of electricity at the moment of writing. Another example is the Orbital O2, a floating HAHT capable of generating 2 MW of electricity, making it one of the most powerful tidal turbines in operation (Orbital Marine Power (2024)).

Hydrokinetic turbines share many design principles with wind turbines but are adapted to the unique challenges of underwater environments, including higher turbulence, wave loading, potential cavitation,

and structural durability (Adcock et al. 2020, Chen et al. 2015). The density of water, almost 800 times that of air, gives hydrokinetic turbines a distinct advantage over wind turbines (Multon 2012). For the same flow speed, the much higher power density allows smaller systems to generate comparable amounts of energy to larger wind turbines(Yuce et al. 2015).

While various designs exist for hydrokinetic turbines, such as Darrieus, Savonius, and Gorlov configurations, mentioned by Yadav et al. (2023), this review focuses on horizontal-axis turbines. Their demonstrated performance and adaptability to tidal energy conversion make them the most practical and widely adopted configuration.

Installing hydrokinetic turbines in the upper water column, close to the free surface, instead of on the sea bed, simplifies maintenance by increasing accessibility, while also enabling a greater potential energy harvest, as flow velocities in the upper water column are typically up to two to three times higher than those near the seabed (Greenwood et al. 2019). However, this alternative configuration raises the challenge of turbulence and unsteady hydrodynamic forcing of the turbine blades due to wave-induced orbital flow velocities (Polagye et al. 2010, Adcock et al. 2020). This forcing decreases exponentially in magnitude with depth from the free surface and includes both vertical and horizontal velocity components separated by a phase shift, resulting in a complex loading condition characterized by successive changes in flow velocity and direction. These unsteady variations lead to fluctuations in flow acceleration and the angle of attack experienced by the blade (Newman 1977).

Due to the negative impact of unsteady loading on turbine performance and increased fatigue, it is of interest to investigate approaches to control the flow around the blades, with the aim of effectively harnessing high force peaks for energy production, while mitigating the abrupt force fluctuations that may arise from stall or other unsteady flow phenomena. Understanding these unsteady effects is essential for optimizing turbine efficiency, reducing maintenance costs, and improving durability in real-world conditions.

This study focuses on the experimental investigation of hydrokinetic turbines under steady flow conditions and wave forcing. The core of this project involves the design and construction of a model hydrokinetic turbine, which will be tested in the towing tank facility at the Department of Maritime and Transport Technology, TU Delft. After this thesis, the turbine will be available for a wide range of experimental studies. These may include tests in steady flows, wave conditions with different amplitudes and frequencies, or other scenarios aimed at replicating real-world operating environments.

To better understand hydrokinetic turbines as a viable renewable energy solution, this research investigates their design process, providing insights into common practices that can streamline future development of scaled-down models. Addressing the unique challenges of wave-induced forces supports the broader goal of enhancing the reliability and scalability of hydrokinetic energy systems, ultimately contributing to the global transition toward sustainable energy. The first chapter addresses the following sub-question:

"How do past hydrokinetic turbine studies inform the design and testing of a model-scale turbine?"

To answer this, previous research on hydrokinetic turbines is reviewed, with a specific focus on turbine testing methodologies and model-scale design considerations. The chapter begins with a qualitative overview of experimental studies conducted on model-scale HAHT's. Key design parameters are then explored, including blade profile, pitch, chord length, blockage effects, and tank testing conditions. Performance metrics such as the power coefficient, thrust coefficient, tip-speed ratio, and blade root bending moments are analyzed to identify trends across the literature. Based on the literature findings, the main parameters are then defined for the current design. This review ensures alignment with established experimental practices and provides a foundation for future design decisions, while also identifying current research gaps.

1.1. Overview of past research on model-scale testing

The development and performance evaluation of model-scale hydrokinetic turbines have been widely studied in recent decades. Prior work has examined turbine hydrodynamics, wake development, wave-current interactions, efficiency, and structural response. This section reviews experimental studies on model-scale HAHTs to identify commonly used test parameters and assess the performance of comparable designs under controlled conditions. The aim is to extract relevant design values and methodologies that can guide the current study in line with established methodologies.

1.1.1. Trends and gaps in literature

Figure 1.1 shows the distribution of past research topics in this review, categorized by their main area of focus and highlighting the relative attention given to each theme. It should be noted that the categorization is based on the dominant topic of each study. For example, although many papers discuss blockage effects, this topic was not assigned a separate category to avoid overlap. The relatively high share of studies involving wave interaction reflects the current research focus on unsteady loading, as all studies mentioning wave effects were grouped under this heading.

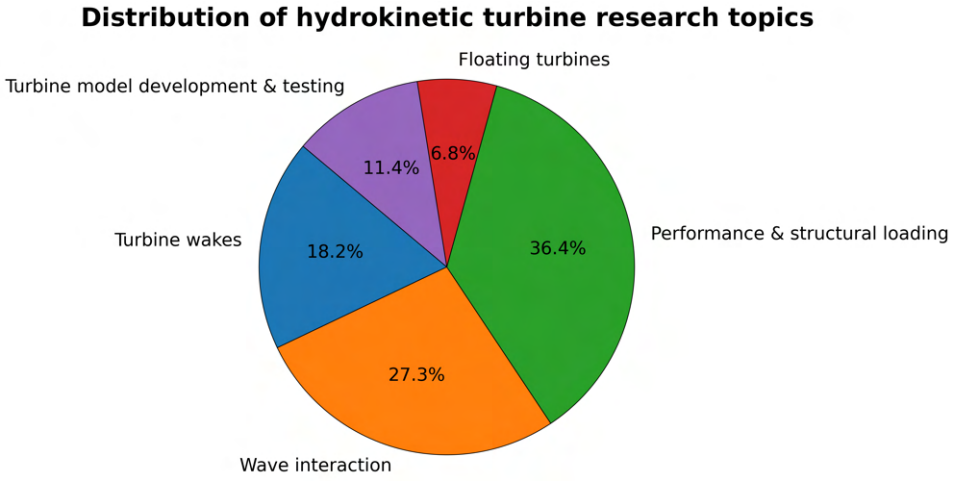

Figure 1.1: The distribution of the different categories of this literature review.

Over the past decades, research on model-scale hydrokinetic turbines has evolved from steady-state performance tests toward investigations of unsteady loads, wake behavior, and wave-current interaction. This evolution has been driven by the need to develop efficient and durable turbines that can operate reliably in real-world marine environments, ideally close to the water surface.

A review of the existing literature on hydrokinetic turbines testing reveals that wave interaction, performance assessment, and structural loading have been the primary areas of focus in experimental model-scale testing. Wake behavior has also been widely studied, as seen in numerous investigations into wake persistence, turbulence development, and wake recovery. In contrast, research on floating turbine systems remains rare, with all existing studies emerging in recent years. Additionally, design- and manufacturing processes are often poorly documented, reducing the reproducibility of results.

Studies such as Payne et al. (2017), Ellis et al. (2018), and Allmark et al. (2020) document turbine development and experimental validation, but they primarily focus on finalized designs rather than the step-by-step decision making involved in component selection, financial limits, structural considerations, and instrumentation integration. A comprehensive overview of past design methodologies could support future research by streamlining the development process, improving reproducibility, and ensuring comparability across studies.

One notable trend is the transition from single-turbine studies to multi-turbine wake interaction analyses. Early works, such as Chamorro et al. (2013a) and Chamorro et al. (2015), examined wake persistence and turbulence characteristics for a single turbine. More recent studies, such as the ones from Nuernberg et al. (2018) and Watanabe et al. (2023), have investigated wake interactions in turbine arrays,

emphasizing the importance of lateral spacing for efficient wake recovery. These studies highlight the growing interest in optimizing turbine spacing and wake mixing strategies for large-scale deployments.

Another research evolution is the increasing focus on wave-current interactions and their impact on turbine performance and structural loads. While Bahaj et al. (2007) provided early steady-state performance references, more recent studies such as Draycott et al. (2019) and Guo et al. (2018) examined how (ir)regular waves influence thrust, power fluctuations, and fatigue loads. These studies found mean power output largely unaffected, but peak loads can double in opposing currents, increasing structural stresses. However, wave-driven dynamic stall effects remain poorly understood, as most work targets global load fluctuations rather than detailed blade-level flow visualization.

Most studies on structural integrity and material selection have focused on metal or composite blades, with limited exploration of alternatives such as 3D printing, only in recent years. Lande-Sudall et al. (2023) is among the few to test 3D-printed blades, providing some details on the fabrication process. Watanabe et al. (2023) and Ferraiuolo et al. (2024) were the only two other studies explicitly mentioning the use of 3D printed blades. However, no extensive research has been conducted on the structural behavior of 3D-printed turbine blades, especially under wave-driven loads. Given the increasing accessibility of additive manufacturing, future research should assess structural loading and manufacturing details.

1.1.2. Research aim and question

The review of existing literature has highlighted key advancements and gaps in hydrokinetic turbine research. Despite several studies on wave-induced power fluctuations and structural loads, there is limited understanding of dynamic stall effects at the blade level under wave conditions. Additionally, the structural performance of 3D-printed blades remains largely unexplored, with only a few studies briefly mentioning their use. Finally, few studies provide details on the turbine design process, making it challenging for new research efforts to develop model-scale setups efficiently.

This research aims to address these gaps by focusing on the design, construction, and analytical assessment of a model-scale hydrokinetic turbine. Unlike many studies that emphasize performance optimization, this work is centered on the practical aspects of developing a structurally robust, efficient and functional turbine for laboratory testing. The study will explicitly document the step-by-step design process, including component selection, nacelle integration, instrumentation, and force measurement implementation, providing a resource for future experimental programs. Analytical predictions of thrust, torque, and hydrodynamic forces are made prior to construction to enable later validation.

Based on the identified research gaps, this thesis addresses the following question:

”How can a model-scale hydrokinetic turbine be designed, constructed, and tested to ensure structural integrity, cost-effectiveness, and compatibility with existing experimental studies while enabling accurate performance evaluation for future research?”

By addressing this question, the thesis aims to contribute to the standardization of experimental hydrokinetic turbine design, ensuring compatibility with past studies while supporting new investigations, for example into wave-induced effects and the durability of 3D-printed blades. To understand what has been studied, a review of earlier model-scale turbine designs is required. Tables 1.1 and 1.3 therefore summarize key design characteristics, test conditions, and performance metrics from past studies, which directly inform the design methodology and parameter choices adopted here.

Before moving to this detailed review, it is useful to outline the structure and purpose of the introductory chapter itself. The following sections highlight the main contributions from earlier work on model-scale hydrokinetic turbines, with a particular focus on experimental studies. The aim is not only to summarize what has been done, but also to identify successful design solutions and highlight limitations that remain. In this way, the literature review provides a solid foundation for the present thesis. By examining how blade and hub geometries, testing setups, and performance predictions have been handled previously, the design choices made in this work can be better motivated and compared against established studies.

1.2. Terminology

A horizontal-axis hydrokinetic turbine extracts energy from currents similarly to a wind turbine, but in a denser medium, yielding higher power density (Multon 2012). The rotor converts the kinetic energy of the flow into shaft power, which a generator converts to electricity (Mohd Badrul Salleh 2019). To ensure consistent comparison across studies, this section defines the terminology used for geometry, performance, and test setups. Typical towing-tank arrangements are shown in figure 1.5.

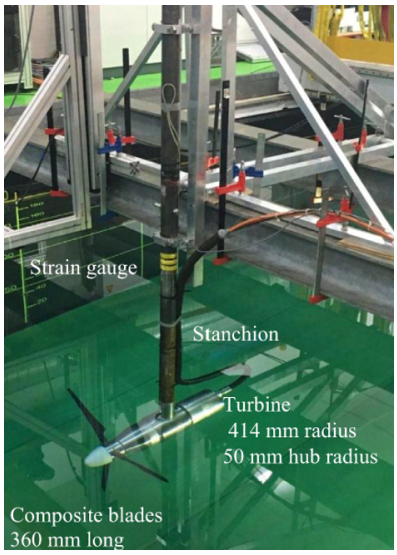

Figure 1.2: Setup 1 (Porter et al. 2020).

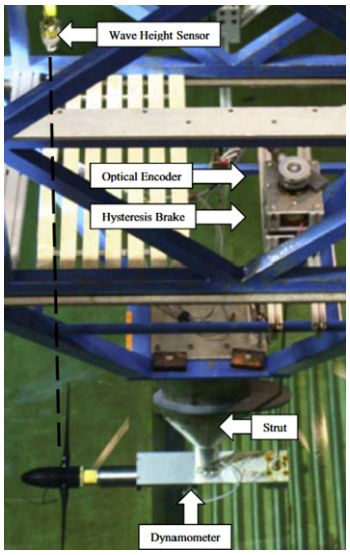

Figure 1.3: Setup 2 (Lust et al. 2013).

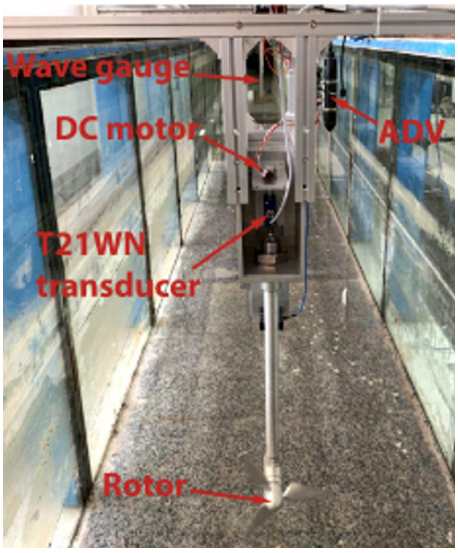

Figure 1.4: Setup 3 (Zhang et al. 2021).

Figure 1.5: Some example setups for hydrokinetic turbine testing on model-scale.

1.2.1. Rotor parameters

The main components that are used in a typical hydrokinetic turbine test are described below and shown in figure 1.6. This should help to understand the terminology that is being used in this research.

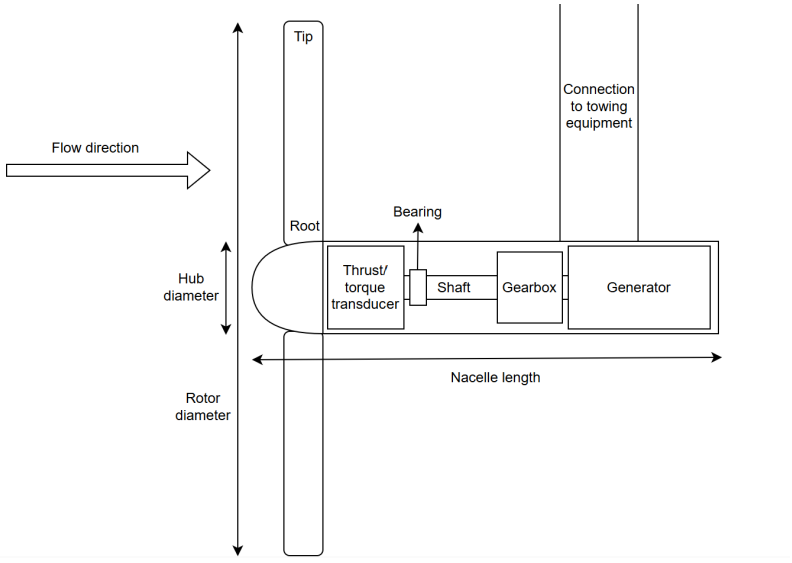

Figure 1.6: Schematic side view of a typical hydrokinetic turbine.

- The **flow direction** is to the right in this case, as the turbine is towed towards the left.
- The **rotor diameter (D)** represents the full span of the turbine blades.

- The **hub diameter (H)** is the central part of the rotor, connecting the blades to the shaft.
- The **root** section of the blade is the part closest to the hub.
- The **tip** section is the outermost part of the blade.
- The **thrust–torque transducer** measures both thrust and torque.
- The **shaft** rotates and transfers the energy from the hub to the generator.
- A **bearing** supports the rotating shaft, in most cases several are needed.
- The **gearbox** converts the slowly rotating shaft of the blades, to a high speed rotation that the generator can handle.
- The **generator** converts the mechanical energy into electrical energy
- The **connection to the towing equipment** holds the turbine in place and can accommodate data transfer cables.
- The **nacelle** is the enclosure housing the drivetrain, measuring equipment and generator.

1.2.2. Blade parameters

Beyond the overall HAHT layout, turbine performance is largely governed by blade design. The cross-sectional shape of the blades uses foil designs that optimize hydrodynamic performance. Figure 1.7 summarizes the foil parameters used in this study. The foil geometry creates a pressure difference between the suction (low pressure) and pressure (high pressure) surfaces, generating lift (Munson et al. 2012).

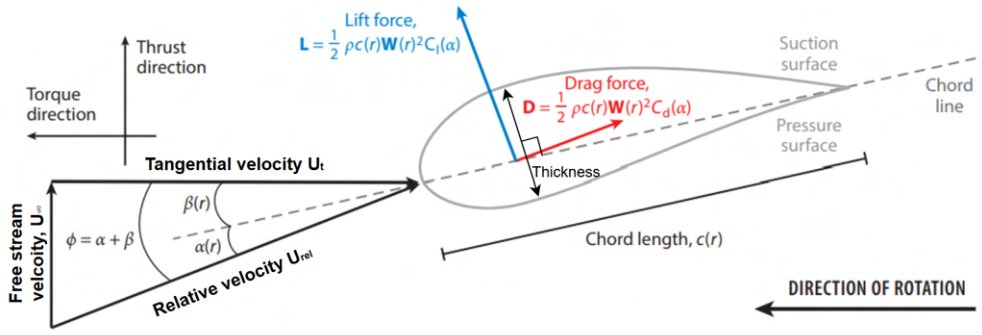

Figure 1.7: Foil terminology, adapted from Adcock et al. (2020)

- The **flow direction** is upwards in this figure, measured as **free stream velocity** U_∞, parallel to the direction of thrust.
- The **direction of rotation** is to the left, parallel to the torque direction.
- The **tangential velocity** U_t is the velocity parallel to the direction of rotation.
- The **relative velocity** U_{rel} is the resultant of the free stream velocity and the tangential velocity.
- $\beta(r)$ is the angle between the chord line and blade travel direction, or the **pitch angle**.
- $\alpha(r)$ is the angle between the hydrofoil chord line and the incident flow vector (U_{rel}), the **angle of attack**.
- ϕ is called the **flow angle**, the summation of the angle of attack and the local **twist angle**.
- The **chord length** $c(r)$ is the distance between the trailing edge and the leading edge.
- The **thickness** is the distance between the upper and lower surfaces of the foil, perpendicular to the chord line.
- The **lift force** acts perpendicular to the relative velocity, resulting from turbine rotation.
- The **drag force** acts parallel to the relative velocity, resulting from turbine rotation.

1.2.3. Performance parameters

As key concepts throughout this thesis, several performance parameters are introduced here to clarify the terminology used in later sections. First of all, the value C_p, which is a measure of the efficiency of the turbine, it is expressed as follows:

$$C_p = \frac{P_{turbine}}{\frac{1}{2} \cdot \rho \cdot A \cdot U_\infty^3} \tag{1.1}$$

Second, the thrust coefficient C_t is defined as the ratio between the thrust force (axial force on the turbine) and the dynamic pressure of the incoming flow:

$$C_t = \frac{T}{\frac{1}{2} \cdot \rho \cdot A \cdot U_\infty^2} \tag{1.2}$$

The last important parameter to introduce at this stage is the tip-speed ratio (TSR). This value represents the ratio between the blade tip velocity and the free-stream velocity:

$$TSR = \frac{\Omega \cdot R}{U_\infty} \tag{1.3}$$

1.3. Dimensional parameters

This section summarizes key geometric and facility parameters reported in model-scale hydrokinetic turbine studies (table 1.1). Performance parameters follow in section 1.4. The goal is to extract concise design ranges and implications for the turbine design. Based on the information from the table, different conclusions can be drawn on what was previously done and why. This analysis not only provides a theoretical foundation for hydrokinetic turbine design, but also helps to identify gaps in the reported values, highlighting aspects that may require additional attention during the design process.

1.3.1. Number of blades

Blade number is a key early design choice. While no strict formula exists (Yadav et al. 2023), insights are largely drawn from wind energy studies (Badshah et al. 2017; Yadav et al. 2023).

Performance

Theoretically, more blades can have a higher maximum power coefficient for the same tip-speed ratio as explained by Manwell et al. (2009), also see figure 1.8. However, fewer bladed turbines often operate at higher tip-speed ratios, and thus increased power coefficient, which results in the fact that in real life, there is only little difference in actual achievable C_p (Manwell et al. 2009).

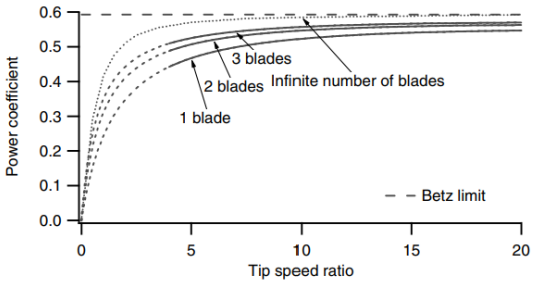

Figure 1.8: Effect on maximum attainable C_p for different amount of blades, as a function of tip-speed ratio (Manwell et al. 2009).

Two-bladed turbines are suitable for high TSR values, because a smaller surface area leads to reduced drag, allowing faster rotational speeds in high-velocity flows (Delafin et al. 2016, Badshah et al. 2017, Adeyeye et al. 2021). Conversely, three-blade turbines balance TSR and torque, making them more suitable for a broader range of flow conditions (Manwell et al. 2009). Increasing to four blades reduces TSR but enhances torque, which is beneficial in low-flow environments (Brasil et al. 2019, Badshah et al. 2017, Adeyeye et al. 2021).

Table 1.1: Model-scale hydrokinetic turbine datasets extracted from literature. T/F indicates towing tank (T) or flume tank (F), and TD (L×B×H) gives the tank dimensions in meters. Other abbreviations are defined in the nomenclature.

Ref	N	D(mm)	D_nxL_n(mm)	Blade profile	$\theta(^\circ)$	t(mm)	c(mm)	ϵ(%)	T/F	TD(LBH)(m)
Chamorro et al. 2013a Chamorro et al. 2015	3	500	.x389	NACA 44XX	20-0	13-2	60-22	4	F	85x2.75x1.8
Chamorro et al. 2013b	3	126	80x390		34-1	4-1	11-4	3.6	F	10x0.5x0.7
Chen et al. 2017a	3	300			30-15		45-30	16	F	14.4x0.8x0.54
De Jesus Henriques et al. 2014	3	500						18	F	3.7x1.4x0.76
Draycott et al. 2019,Payne et al. 2017	3	1200	120x1030	NACA 63-8XX	23-5		44-29	16	F	18x4x2
Farhoody et al. 2023	3	1150	250x510	NACA 63–8xx	19 -5	25-12	120-40	19	T	11x3x1.85
Doman et al. 2015	3	762	178x.	NREL S814	28-7		60-20	4.7	T	76x4.6x2.5
Faudot et al. 2012	2	1475						3.5	T	260x10x4.9
Galloway et al. 2014	3	800		NACA 48XX				7	T	60x3.7x1.8
Gaurier et al. 2013	3	900	46x720	NACA 63418	30-5	27-8	113-27	7.9	F	18x4x2
Gaurier et al. 2015	3	700	46x720	NACA 63418	30-5	20-6	88-20	3.3	B	76x4.6x2.5
Guo et al. 2018	3	800	100x.	NACA 63-8xx	20-0	32-4	67-32	3	T	130x6x3
Bahaj et al. 2007	3	800	100x.	NACA 63-8xx	15-0	12-3	50-20	7.5	T	60x3.7x1.8
Kolekar et al. 2015	3	280		SG6043	10		16.7	16	F	1.98x0.61x0.61
Luznik et al. 2013	3	460		E387	20		50-25	4.6	T	37x2.4x1.5
Milne et al. 2013	3	780	120x.	NREL S814	28-5	16-7	65-30	4.7	T	76x4.6x2.23
Stallard et al. 2015	3	270			38-3		30-13	2.5	F	26x5x0.45
Tian et al. 2018	3	1200		W FF-77-W	15-3		57-48	5	T	132x10.8x2
Wang et al. 2007,Shi et al. 2016	3	400	80x.	S814	27-2		65-30	13	C	.x1.2x0.8
Zhang et al. 2021	3	300	50x170	NREL S8XX	14-0	15-4	48-15	9.8	F	4.4x1.2x0.6
Watanabe et al. 2023	3	400	60x400	NACA 4412	34-4		78-30	2.5	T	65x5x1
Alamian et al. 2020	3	1150	320x510	NACA 63-8XX	20-6	25-12	120-25	12	T	11x3x3
Allmark et al. 2020, Ordonez-Sanchez et al. 2019, Ellis et al. 2018	3	900	130x.	W FX63-137	27 -8		109-58	2.8	T	220x9x3.5
Jing et al. 2024,Mei et al. 2024	2	700	100x240	NREL S809	26-0	19-8	90-38	24	F	75x1.6x1
Lande-Sudall et al. 2023	3	700	96x760	NACA 63-418	30-5	17-5	75-17	5.8	T	50x3x2.2
Huang et al. 2022	3	1000	100x.	NACA 63-910	32-7	20-3	85-25	1.9	T	192x10x4.2
Lust et al. 2013	2	800		NACA 63-618	20-9		70-25	1.3	T	116x7.9x4.9
Nuernberg et al. 2018	3	280	60x558	NREL S814	23-6		42-21	1.3	F	8x3x0.56
Porter et al. 2020	3	828	100x.	NREL S814	29-8		64-13	6.7	F	18x4x2
Schmitt et al. 2022	3	1050	350x.	W FX 63-137				6.9	T	76x4.6x2.5
Seo et al. 2016	3	400		NACA 63-418	17-2		34-14	0.45	T	110x8x3.5
Shahsavarifard et al. 2015	3	198	37x.	H0127 blade	30-4	7-2	47-23	8.4	F	1.8x0.61x0.6
Slama et al. 2021	3	676	55x720					5.1	F	18x4x2
Song et al. 2012	3	700		NACA 63-418	17-2		60-24	1.4	T	100x8x3.5
Gambuzza et al. 2025	3	1200		NACA 63-8XX	18-5	32-11	134-88	14	F	10x3.6x2.25
Barber et al. 2017	3	450	110x910	NACA 44xx	16-3	79-4	79-23	22	F	13x0.98x0.73
Ferraiuolo et al. 2024	3	236	25x.	EPPLER 818				45	F	3.5x0.30x0.5

At the literature-average TSR of 5.1, Manwell's design guideline points to a three-bladed rotor as optimal. In addition, three blades reduce torque fluctuations compared to two, with only diminishing benefits for a fourth (Delafin et al. 2016, Yadav et al. 2023), which is mainly relevant for hydrokinetic turbines operating in wave conditions.

The amount of blades also strongly influences the solidity, a key parameter in turbine design, which is the ratio between blade area and swept area.

$$\sigma = \frac{N \cdot c}{2 \cdot \pi \cdot R} \tag{1.4}$$

Where N is the number of blades, c the chord length, and R the rotor radius. Higher solidity increases energy extraction at low velocities, but can reduce efficiency at higher velocities due to drag (Abutunis et al. 2022). Studies on tidal turbines show that increasing blade count from two to three improves the power coefficient by about 1.5%, while moving from three to four yields only a 0.2% gain (Badshah et al. 2017; Manwell et al. 2009).

Structural implications and costs

Increasing the number of blades helps distribute the loads more evenly across the turbine, reducing peak stresses on individual blades. For instance, two-bladed designs often exhibit increased blade root bending moments compared to three-bladed designs (Badshah et al. 2017). By contrast, three or more blades reduce these stresses, enhancing durability, albeit at higher material and manufacturing costs. From an economic perspective, reducing blade numbers can lower manufacturing, transportation, and installation costs. As mentioned, turbines with less blades typically operate at higher TSRs, which also results in a smaller chord and a smaller gear box, which reduces material cost (Badshah et al. 2017). However, this cost sensitivity is mainly relevant for utility-scale machines; for model-scale experiments with 3D-printed blades, the difference in production cost between two and three blades is marginal. The findings are summarized in table 1.2.

More Blades	**Less Blades**
Higher costs	Lower costs
Higher torque, beneficial for low flow	Lower torque, less effective at low flow
Lower TSR, less efficient in high flow	Higher TSR, suited for high flow
Higher efficiency at low flow	Better efficiency at high flow
Reduces stress per blade	Higher stress per blade
Smoother torque, stable operation	More fluctuations, less stable
Minimal thrust changes	Uneven thrust, potential instability

Table 1.2: Comparison of turbines with more blades vs. less blades.

1.3.2. Diameter

Together with determining the number of blades, the choice of turbine diameter is another critical consideration in the early design phase of model-scale hydrokinetic turbines. A larger diameter increases the rotor swept area, directly enhancing torque and thrust following momentum theory:

$$T = \frac{1}{2} \cdot \rho \cdot \pi \cdot C_t \cdot U_\infty^2 \cdot R^2 \tag{1.5}$$

$$Q = \frac{1}{2} \cdot \rho \cdot \pi \cdot C_q \cdot U_\infty^2 \cdot R^2 \tag{1.6}$$

where R represents the rotor radius, indicating the relationship between thrust, torque, and radius.

However, larger diameters also pose challenges, including depth constraints, increased wave loading near the free surface, support structure limits, and larger root bending moments (Grogan et al. 2013).

In towing-tank testing, the primary limitation is tank size. To avoid blockage (section 1.3.8), the rotor diameter must remain a small fraction of the tank cross-section to preserve open-water flow conditions. Within facility limits, maximizing diameter reduces scaling effects and improves similarity to full-scale operation (Payne et al. 2017). The average turbine diameter reported in the literature is 0.68 m.

1.3.3. Hub and nacelle dimensions

Almost 70% of the studies in this review report the hub diameter, while only 39% include the nacelle length. Using the available data, the hub diameter can be estimated from the rotor diameter, as shown in figure 1.9a, with larger rotors generally having larger hubs due to higher structural loads (see 1.3.2).

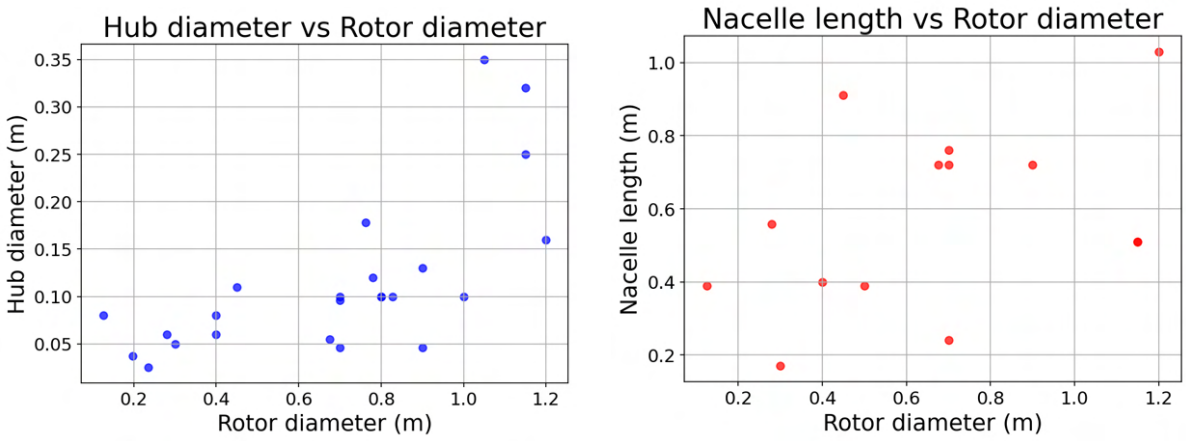

(a) Hub diameter as a function of rotor diameter

(b) Nacelle length as a function of rotor diameter

Figure 1.9: Geometric turbine parameters as a function of rotor diameter

As turbine size increases, other components within the nacelle such as the shaft, gears, and measuring equipment, also grow. Consequently, nacelle length is expected to scale with rotor diameter. Although figure 1.9b suggests a weak correlation, the data is too limited and scattered to draw definitive conclusions. Nacelle length ultimately depends on specific equipment requirements and design constraints.

1.3.4. Blade profile

Foil selection directly affects turbine efficiency, structural performance, and operating range (Batten et al. 2005). At model-scale, Reynolds numbers are relatively low, which increases viscous drag and reduces lift (Gupta et al. 2020). While lift rises roughly linearly at small angles of attack, stall causes a rapid drop. Thin foils generally yield higher efficiency (Muratoglu et al. 2015), whereas thicker foils are required near the root for strength and cavitation resistance (Ahmed 2012).

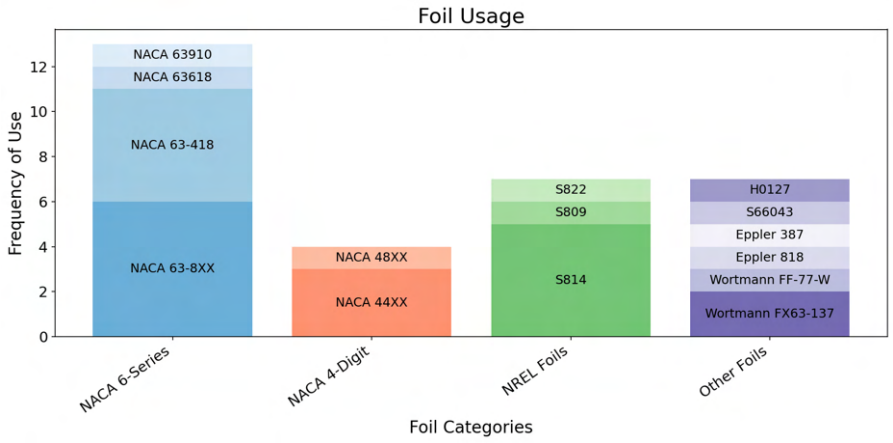

Figure 1.10: The usage of different foils in previous research

Figure 1.10 summarizes the frequency of foil usage in previous studies, showing that blade profiles are most often NACA 6-series foils. This series is designed for extended laminar flow (Abbott et al. 1959; Manwell et al. 2009) and high lift, but with higher drag outside their optimal range (Yadav et al. 2023). NACA 4-digit sections have also been used for their simplicity, robustness, and stable stall behavior, despite generally lower lift-to-drag ratios (Abbott et al. 1959; Yadav et al. 2023). Barber

et al. (2017) also noted their effectiveness under low Reynolds number conditions. Some studies adopted thick NREL designs such as the S814, optimized for strength and low sensitivity to blade roughness (Tangler et al. 1995). Other profiles appear less frequently, including Eppler (Selig et al. 2012), Wortmann (Tian et al. 2018), Selig (Gigue're et al. 1998), and custom designs, like the H0127 profile from Shahsavarifard et al. (2015).

Foil shapes visualized

To illustrate geometric differences, figure 1.11 compares the four most common foils across root, mid-span, and tip thickness ratios. The NREL S814 is visibly thicker and suited for root regions, while thinner foils such as NACA 44XX prioritize hydrodynamic performance at the tip. These plots highlight the trade-off between structural strength and efficiency that guides final foil selection in this study.

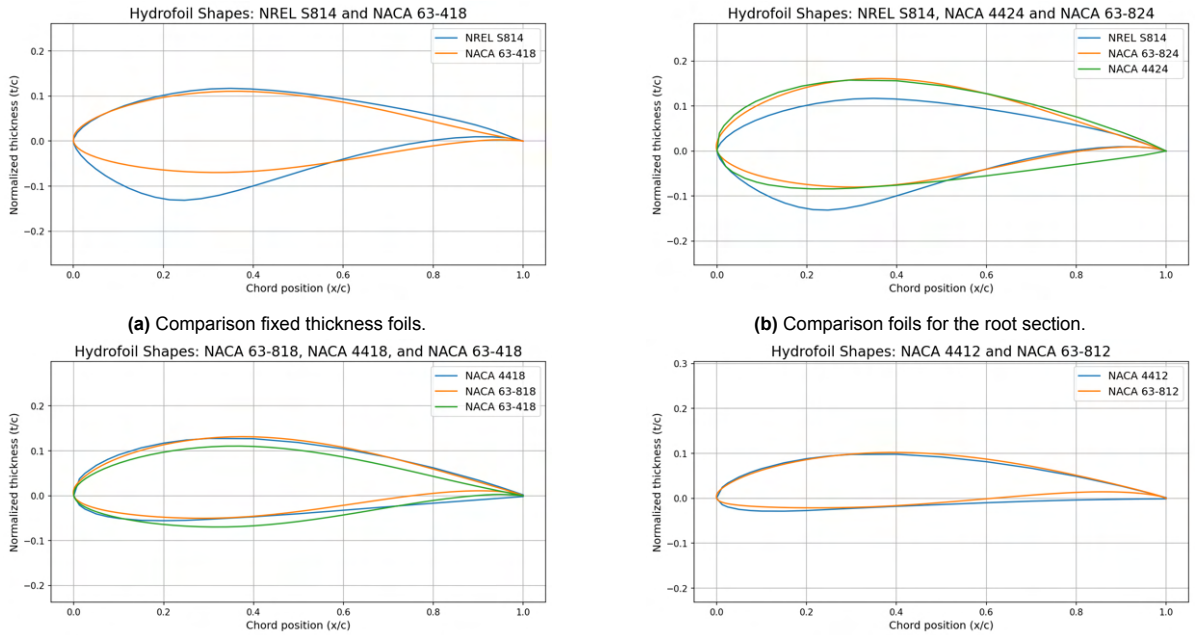

(a) Comparison fixed thickness foils.

(b) Comparison foils for the root section.

(c) Comparison foils for the mid-section

(d) Comparison foils for the tip section.

Figure 1.11: Comparison of foil shapes

1.3.5. Pitch and twist

After choosing a foil profile, the blade must be pitched and twisted for optimal performance. Twist (θ) is defined here as the local pitch angle along the span, while pitch (β) is the angle between the chord line and the rotor plane (aligned with U_t, see figure 1.12). Some authors define pitch at 2/3 span, where values of $5°$-$10°$ are typical, as illustrated in figure 1.13.

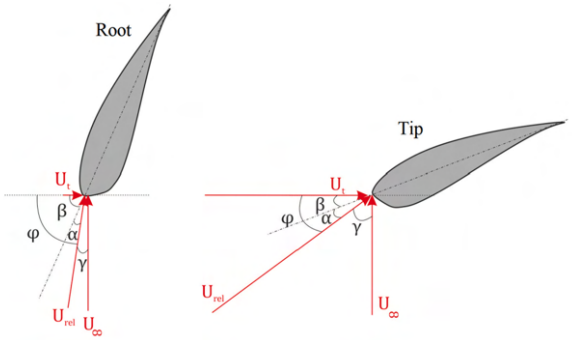

Figure 1.12: Flow differences between the root and tip section of the blade (Muratoglu et al. 2020).

Figure 1.13 shows the reported twist distributions. Across all studies, the twist angle decreases towards the tip of the blade. The rate of decrease along the blade span is relatively uniform among the designs.

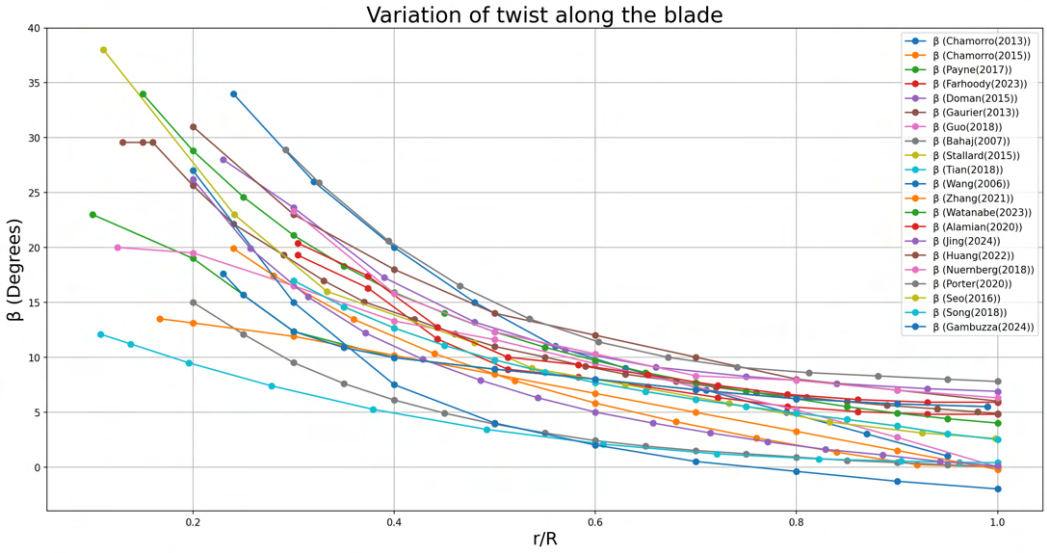

Figure 1.13: Twist distribution along the normalized blade radius

In some cases, the optimal twist angle becomes negative (for Wang et al. 2007 and Zhang et al. 2021). This happens when the angle of relative velocity becomes smaller than the optimal angle of attack of the foil, as also shown by Khchine et al. (2018). Another reason for a slight negative twist angle might be to reduce turbulence and noise coming from the tip of the blade, as Wang et al. (2007) and Zhang et al. (2021) are both focusing on this in their research. Significant variation in the reported twist angles are reported near the root. This variability likely arises from differences in performance requirements like the optimal TSR.

1.3.6. Chord

Another important parameter for blade shape is the chord length, which in many studies defines the scaling of the blade profile, with other parameters being expressed as a percentage of the foil chord (see 1.3.4 and 1.3.7). Figure 1.14 shows the non-dimensional chord distribution c/R along the blade radius for different studies.

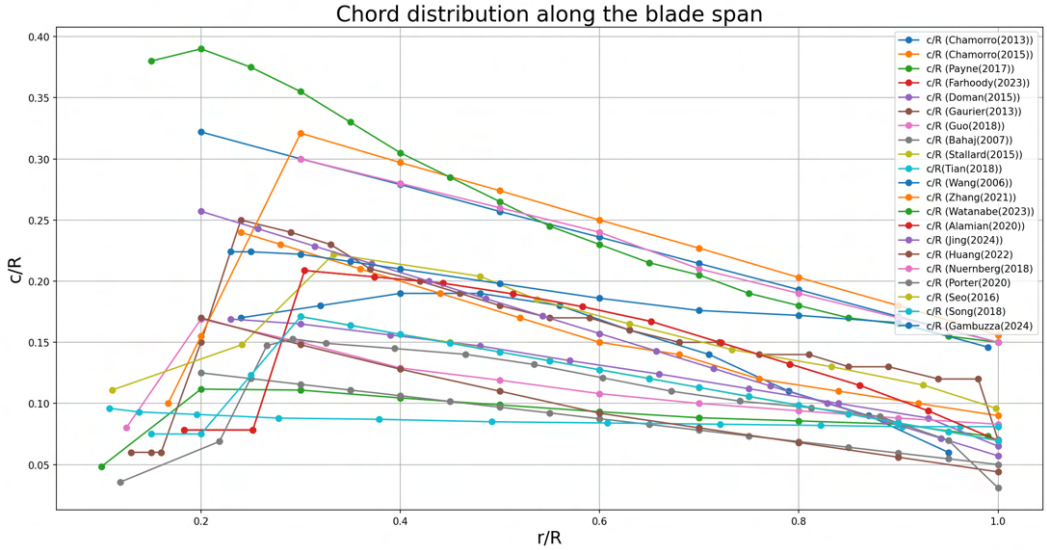

Figure 1.14: Chord length normalized by the rotor radius (C/R) as a function of the radial position along the blade (r/R).

Most designs follow a similar taper, though root values range from 10-15% up to over 30%. In general, larger chord lengths at the root provide structural strength and maintain lift at low local TSR, while shorter tip chords reduce drag-related tip losses (Gasch et al. 2012). Some declining c/R trends also reflect circular root sections (see section 1.3.7).

1.3.7. Thickness

The final important parameter defining the shape of the blade is the thickness. Blade thickness distribution (t/c) balances structural strength and hydrodynamic efficiency. Unlike twist and chord, relatively few studies report detailed thickness data, since many foils use a fixed t/c along the span.

However, some studies feature varying t/c distributions, as shown in figure 1.15. The different studies have similar trends of t/c along the blade. Except for Alamian et al. (2020) and Farhoody et al. (2023) (of which is one not visible because they have the exact same values) and Gaurier et al. (2013), all thickness ratios converge from $t/c \approx 20 - 24\%$ at the root, to around 12% at the tip. The increase in t/c near the tip can be attributed to a decrease in chord length, while the thickness remains similar. Some studies also report a circular root section with t/c reaching up to 100%, reflecting structural priorities over hydrodynamic performance. The actual thickness ranges in millimeter are given in table 1.1. Additional zoomed thickness distributions are provided in Appendix A.

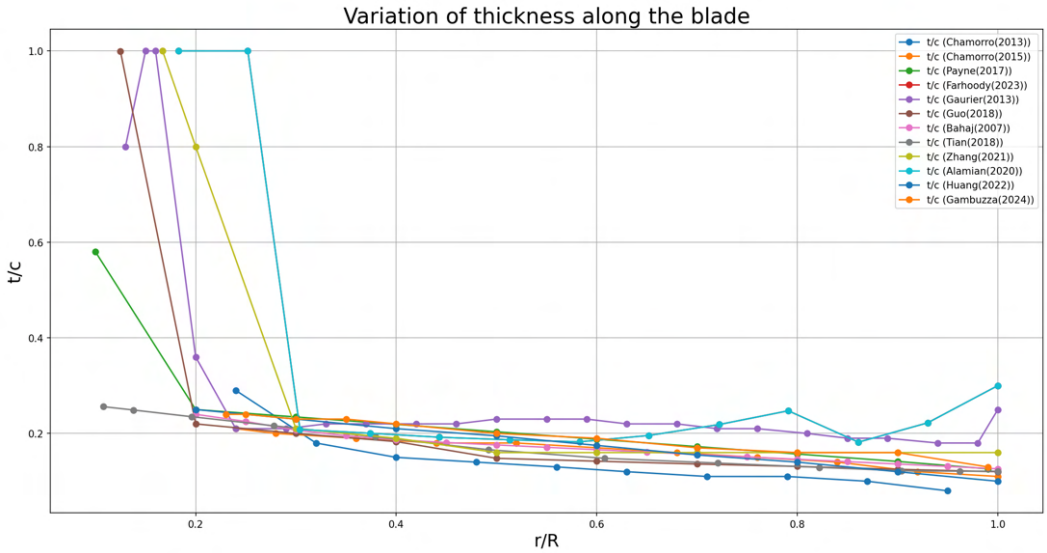

Figure 1.15: Thickness distribution along the normalized blade radius.

Circular root

The use of a circular root section can offer several advantages. One primary advantage is the modularity it provides, enabling blade exchanges and possibly pitch adjustments during experiments. This design is particularly useful for testing different blade profiles, diameters, materials, or pitch angles, which is essential for investigating turbine behavior under varying angles of attack (Payne et al. 2017).

Several studies adopt circular root sections to enable blade interchange and pitch adjustment (Bahaj et al. 2007; Farhoody et al. 2023; Gambuzza et al. 2025). These designs accommodate active or passive pitch mechanisms (examples in Appendix A). The circular geometry makes the blade thick in the flow direction, where flapwise bending moments dominate. Edgewise loads are generally less critical (Manwell et al. 2009), see section 1.4.8 for more details. This is also shown during experiments by for example Galloway et al. (2014) and Doman et al. (2015).

Although it does not generate lift, a circular root provides clear experimental and structural advantages. To minimize penalties, the circular region is typically limited to the hub connection (Payne et al. 2017), while the remainder of the blade follows foil-based thickness distributions optimized for performance and durability.

1.3.8. Blockage

When testing hydrokinetic turbines at model-scale, blockage is an important parameter linked to rotor diameter and the facility size. In confined environments such as flumes or towing tanks, channel walls can accelerate the flow, artificially increasing power and thrust compared to open-water conditions (Kinsey et al. 2017). Corrections are therefore required for meaningful comparison to full-scale performance.

Blockage values from the reviewed studies are listed in table 1.1. Some were reported directly, others calculated, but all use the same definition (Kinsey et al. 2017):

$$\epsilon = \frac{A_t}{A} \tag{1.7}$$

where A_t is the swept area of the turbine, and A is the cross sectional area of the channel.

For a blockage ratio above 5-10% (Ross et al. 2020 Kolekar et al. 2015), the theoretical maximum efficiency of the turbine can exceed the Lanchester-Betz limit (Garrett et al. 2007). Garrett et al. (2007) is still a widely referenced research, showing the power coefficient can increase with increasing blockage by a factor $(1-\epsilon)^{-2}$. The main reason for applying a blockage correction in the current research is to accurately model full-scale conditions (Ross et al. 2020). Full-scale tidal turbines can also experience blockage effects, in this case it would be necessary to do tests in comparable high blockage conditions.

The impact of blockage ratio on the water flow was demonstrated in a CFD simulation by Vogel et al. (2017), where differences in flow velocity and pressure coefficients between a low blockage condition ($\epsilon = 0.0507$) and a high blockage condition ($\epsilon = 0.196$) (figure 1.16) resulted in increased rotor performance. The C_p value increases from 0.53 for the low blockage scenario, to 0.74 for the high blockage scenario. The C_t value increases for the same scenarios from 1.04 to 1.36.

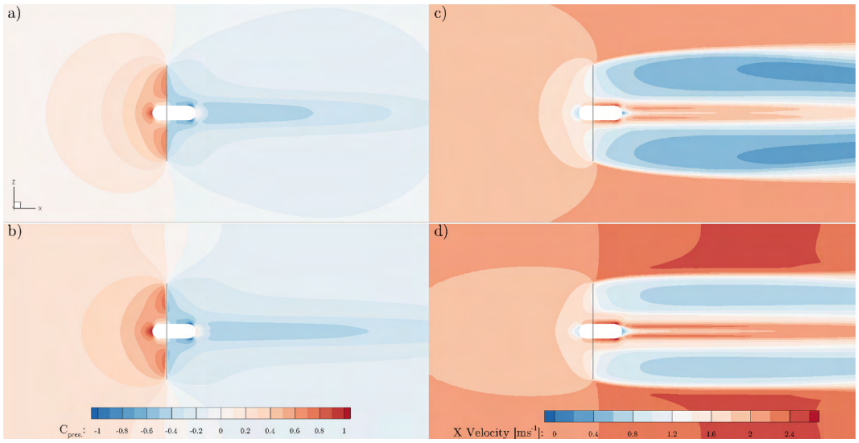

Figure 1.16: The pressure coefficient (a and b) and the stream wise velocity, for a blockage of 0.0507 (a and c) and 0.196 (b and d), tip-speed ratio of 5 and free stream velocity of 2 m/s (Vogel et al. 2017).

To avoid the major distortions that can be caused by blockage effects, the present experiments will be conducted at $\epsilon < 0.05$, representing open-water conditions. When comparing to high-blockage studies, corrections need to be applied to ensure consistent performance metrics.

1.3.9. Tank type and dimensions

The final dimensional parameter of table 1.1 concerns the test facility. Hydrokinetic turbines are mainly studied in flume tanks (18 studies) and towing tanks (19 studies), with no clear preference. A single study used a cavitation tunnel, but this is specific to cavitation research and outside the present scope.

Comparison of Flume and Towing Tanks

Flume tanks and towing tanks each have unique advantages and limitations, as highlighted by Gaurier et al. (2015). Flume tanks generate flow by recirculating water past a stationary turbine, while towing tanks create relative motion by towing the turbine through stationary water.

The following key differences and considerations emerge from Gaurier et al. (2015):

- Flume tanks generally have higher turbulence levels due to recirculation, causing larger fluctuations in torque and thrust measurements. In contrast, towing tanks tend to provide more uniform flow conditions, but are subject to potential vibrations or disturbances from the towing carriage.
- Blockage is often more pronounced in flume tanks due to their smaller cross-sectional areas. Towing tanks, with typically larger dimensions, experience less blockage effects, providing results closer to open-water conditions. Recirculation tanks are more representative of real tidal currents, but are often too small to scale with real-life conditions.
- Flume tanks allow for longer acquisition times, as the turbine remains stationary, while towing tanks are constrained by the tank length, which limits the duration of steady-state measurements.

Despite these differences, both methods produced comparable results for key performance parameters, such as power and thrust coefficients, when corrected for blockage and turbulence effects.

Tank depth is also critical, Kolekar et al. (2015) recommend at least $0.5R$ submergence from the tip to the free surface and $1R$ clearance to the floor, giving a minimum depth of $3.5R$.

1.4. Performance parameters

This section builds on table 1.1 by shifting from dimensional to performance parameters. Table 1.3 summarizes the reported values. The number of decimals per column reflects the original measurement accuracy and the precision needed to distinguish between studies.

1.4.1. Power coefficient

The primary performance parameter for a HAHT is the power coefficient C_p, defined as the fraction of available kinetic energy converted into mechanical power (Kumar et al. 2016), see equation 1.1. Consequently, C_p provides insight into the turbine's efficiency and is used as a performance metric. The theoretical maximum efficiency for a confined turbine is widely known to be 59.3% according to the Betz limit, although this limit can be exceeded in a confined environment, see chapter 2.

All values presented in table 1.3 correspond to the optimal C_p. As C_p depends on parameters such as the tip-speed ratio (see section 1.4.3), the TSR values in table 1.3 indicate the conditions at which maximum efficiency was obtained. Similarly, the reported flow velocity and C_t also correspond to this operating condition. However, most studies considered a range of operating conditions, which is not indicated in the table.

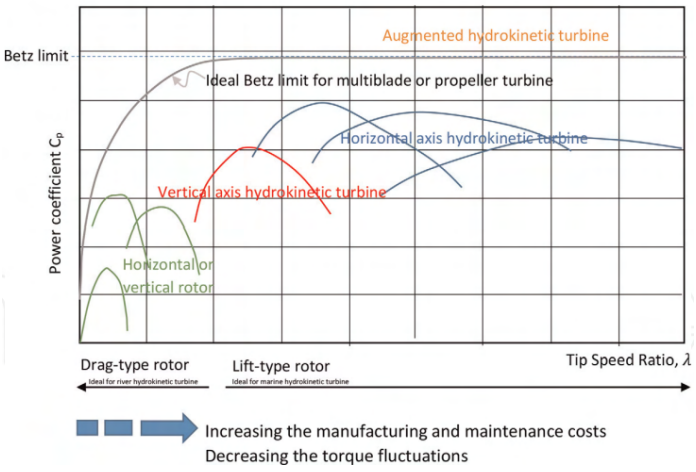

Figure 1.17: Power coefficients for different type of rotors (Kumar et al. 2016).

As illustrated in figure 1.17, horizontal-axis turbines are among the most efficient rotor types (Kumar et al. 2016), operating at relatively high TSRs compared to alternatives. Their C_p curves exhibit the typical peak at one TSR, with efficiency dropping at lower and higher values.

Table 1.3: Performance parameters summary

Ref	C_p	C_t	TSR	U_∞ (m/s)	Fr	Re	T (N)	Q (Nm)	M_{root} (Nm)
Chamorro et al. 2013a Chamorro et al. 2015	0.45		5.8	0.40	0.12	$1.7 \cdot 10^5$			
Chamorro et al. 2013b			4.7	0.20	0.13	$2.5 \cdot 10^4$			
Chen et al. 2017a	0.31	0.39	3.5	0.59	0.26	$3.2 \cdot 10^5$	5	0.17	
De Jesus Henriques et al. 2014	0.38	0.99	3.9	0.50	0.18	$2.5 \cdot 10^5$			
Draycott et al. 2019, Payne et al. 2017	0.50	0.88	6.7	0.81	0.18	$2.5 \cdot 10^5$	385	18.00	44.0/4.0
Farhoody et al. 2023	0.21		7.2	1.00	0.24	$5.8 \cdot 10^5$	70	5.80	
Doman et al. 2015	0.29	0.45	3.5	1.00	0.20	$1.2 \cdot 10^5$	84	6.80	3.6/1.9
Faudot et al. 2012	0.43		7.0	0.67	0.10	$4.9 \cdot 10^5$	320	17.00	
Galloway et al. 2014	0.50	0.80	6.0	0.90	0.21	$3.6 \cdot 10^5$	135	8	15.0/3.0
Gaurier et al. 2013	0.40	1.00	4.5	0.80	0.18	$3.6 \cdot 10^5$			
Gaurier et al. 2015	0.36	0.85	3.5	1.00	0.20	$2.8 \cdot 10^5$			
Guo et al. 2018	0.44	0.95	5.8	0.68	0.13	$1.5 \cdot 10^5$	110	3.50	
Bahaj et al. 2007	0.46	0.80	6.0	1.73	0.41	$6.9 \cdot 10^5$			
Kolekar et al. 2015	0.30		5.9	0.50	0.20	$1.4 \cdot 10^5$			
Luznik et al. 2013	0.38	0.80	5.5	0.60	0.15	$9.4 \cdot 10^4$		0.44	
Milne et al. 2013	0.35	0.65	3.6	0.89	0.19	$3.5 \cdot 10^5$			6.0/-
Stallard et al. 2015	0.30	0.80	4.5	0.46	0.22	$3.0 \cdot 10^4$			
Tian et al. 2018	0.33		5.4	0.50	0.24	$3.0 \cdot 10^5$			
Wang et al. 2007,Shi et al. 2016	0.37		3.6	2.00	0.71	$1.4 \cdot 10^5$			
Zhang et al. 2021	0.33	0.80	3.9	0.40	0.16	$1.2 \cdot 10^4$			
Watanabe et al. 2023	0.45		3.5	0.50	0.25	$2.0 \cdot 10^5$			
Alamian et al. 2020	0.27		7.0	0.56	0.10	$3.2 \cdot 10^5$			
Allmark et al. 2020, Ordonez-Sanchez et al. 2019, Ellis et al. 2018	0.38	0.8	3.5	1.00	0.17	$8.4 \cdot 10^4$	250	14.00	24.0/6.0
Jing et al. 2024,Mei et al. 2024	0.40	0.85	5.5	1.00	0.32	$3.5 \cdot 10^5$			
Lande-Sudall et al. 2023	0.40	0.90	3.5	0.60	0.13	$2.1 \cdot 10^5$		2.90	
Huang et al. 2022	0.46	0.86	8.0	1.50	0.23	$7.5 \cdot 10^5$			
Lust et al. 2013	0.44	0.89	7.0	1.68	0.26	$6.7 \cdot 10^5$			
Nuernberg et al. 2018	0.44	0.95	4.0	0.80	0.12	$1.2 \cdot 10^5$			
Porter et al. 2020	0.28	0.45	4.0	0.80	0.18	$6.6 \cdot 10^5$	80		
Schmitt et al. 2022	0.35		4.0	2.00	0.40	$6.1 \cdot 10^5$			
Seo et al. 2016	0.28	0.55	3.5	1.43	0.29	$2.9 \cdot 10^5$			
Shahsavarifard et al. 2015	0.40	0.50	4.0	1.10	0.22	$2.2 \cdot 10^5$			
Slama et al. 2021	0.45	0.90	5.0	1.40	0.28	$4.3 \cdot 10^5$			
Song et al. 2012	0.45		5.0	1.40	0.28	$6.3 \cdot 10^5$			
Gambuzza et al. 2025	0.30	0.65	7.0	0.50	0.10	$3.0 \cdot 10^5$	145	11.50	
Barber et al. 2017	0.45	0.90	6.0	0.50	0.10	$2.0 \cdot 10^5$	6	0.80	3.0/0.1
Ferraiuolo et al. 2024	0.75		5.5	0.68	0.14	$8.0 \cdot 10^4$			

The average maximum C_p from the model-scale tests is 0.39, over 30% below the Betz limit. The only value above this is Ferraiuolo et al. (2024), explained by a 45% blockage ratio. At the lower end, Farhoody et al. (2023) reports $C_p = 0.21$, likely prioritizing structural optimization, as the tests were done for different pitch angles and in waves. Porter et al. (2020) shows similar reductions under wave loading. Another example is Gambuzza et al. (2025), which achieved only $C_p = 0.30$ despite a detailed design, reflecting its focus on passive pitch control. These cases highlight how design requirements and test conditions can shape performance outcomes.

1.4.2. Thrust coefficient

The thrust coefficient C_t expresses the axial force on the rotor relative to the dynamic pressure of the inflow (Manwell et al. 2009), see equation 1.2. Across the reviewed studies, the average value at maximum C_p is 0.77. The thrust force is the axial force exerted by the fluid on the turbine rotor, which can be measured experimentally using a force transducer. By rewriting formula 1.2, it can be seen that the thrust force will mainly depend on the inflow velocity and the rotor swept area. The C_t value is reported in fewer studies than the C_p value, which suggests that more studies are focused on energy extraction efficiency rather than structural forces acting on the turbine.

It is not uncommon for the thrust coefficient to surpass one, see De Jesus Henriques et al. (2014) and Guo et al. (2018) for example. According to actuator disc theory, an ideal turbine at the Betz limit yields $C_t = 1.0$ in unconfined flow. However, higher values can occur in confined facilities, where pressure build-up invalidates the simple dynamic pressure assumption.

1.4.3. Tip-Speed Ratio (TSR)

The tip-speed ratio (TSR) is defined as the ratio of blade tip velocity to free-stream velocity (Manwell et al. 2009), see equation 1.3. It is a key parameter influencing both C_p and C_t, and turbines are typically designed to maximize efficiency at a specific TSR.

In most experiments, TSR is the primary variable: C_p, C_t, thrust, and torque are plotted as functions of TSR by varying either inflow velocity or the rotational speed of the rotor by applying a load to the shaft.

The average tip-speed ratio for which the turbine models in table 1.3 reach their maximum efficiency is 5.1, with a range between 3.5 and 8.0, meaning the blade tip travels roughly five times the inflow speed under optimal conditions. The wide range of optimal TSR values reflects differences in turbine design, such as blade geometry or operating environments.

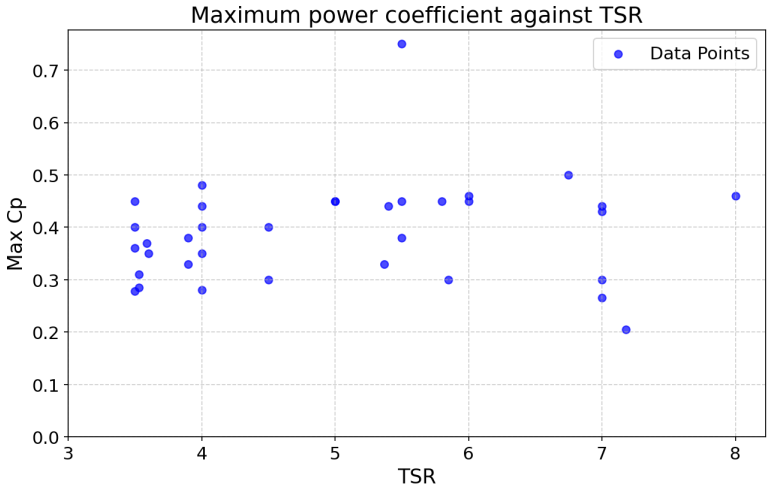

Figure 1.18: Maximum C_p values against their corresponding TSR values from the literature.

The TSR is consistently reported across all studies. Figure 1.18 presents the maximum C_p values against their corresponding TSR values from the literature. More information on the structural implications are discussed further in section 1.4.7.

1.4.4. Flow velocity

While TSR characterizes turbine efficiency across different rotational speeds, the inflow velocity U_∞ directly determines the available kinetic energy and, consequently, the power output of the turbine. The available power scales with the cube of velocity (Manwell et al. 2009):

$$P_{available} = \frac{1}{2} \cdot \rho \cdot \ A \cdot U_\infty^3 \tag{1.8}$$

where ρ is the water density and A_t the rotor swept area. Even small velocity changes therefore cause large differences in performance.

Across experimental studies, the average inflow velocity at which optimal C_p was achieved is about 0.89 m/s. Most tests, however, explored a wider range of velocities to map turbine behavior, but in table 1.3 only the optimal points are summarized.

The flow velocities used in flume and towing experiments are not representative for real-world conditions for which the turbines are designed. The results from these tests must be appropriately scaled to reflect the velocities encountered in natural environments, such as tidal currents or river flows. Average flow velocities for tidal currents, which have the greatest potential from hydrokinetic energy resources, range between 1 m/s and 3 m/s (Yuce et al. 2015), with peaks of up to 5 m/s (Adcock et al. 2020).

Several studies apply Froude scaling to relate model and prototype velocities, ensuring gravitational and free-surface effects are consistent. Equation 1.10 can be used to calculate the flow velocities to use for experimental testing, by setting the Froude number of the the real-world scale turbine equal to the Froude number of the model turbine:

$$Fr_{model} = Fr_{real-world} = \frac{U_{model}}{\sqrt{g \cdot L_{model}}} = \frac{U_{real-world}}{\sqrt{g \cdot L_{real-world}}} \tag{1.9}$$

Where g is the gravitational acceleration, U_∞ is the flow velocity and L is the characteristic length, which is either the diameter of the turbine or the water depth for shallow water conditions in the case of a turbine model test (see 1.4.5). Rewriting this leads to:

$$U_{model} = U_{real-world} \cdot \sqrt{\frac{L_{model}}{L_{real-world}}} \tag{1.10}$$

Reported scaling factors from earlier studies are summarized in table 1.4. The average real world representative turbine from this analysis is found to be 16 m.

Field measurements have demonstrated that tidal stream flow speeds vary with depth, creating a vertically sheared flow profile (Greenwood et al. 2019), mainly influenced by seabed roughness (Horwitz et al. 2017). Additionally, surface interactions, such as wind shear, can further reduce or increase flow velocities near the free surface (Adcock et al. 2020).

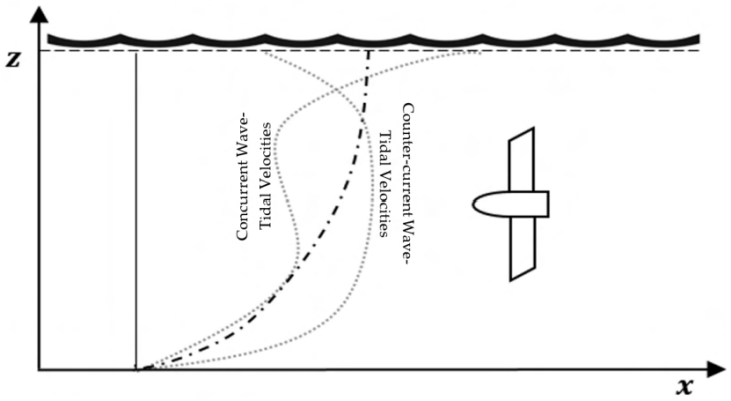

Figure 1.19: Measured flow velocity profiles for a hydrokinetic turbine in a typical flow environment (Encarnacion et al. 2019).

Table 1.4: Scaling factors with the average real life diameter.

Reference	Scale	Real life D
Draycott et al. 2019, Payne et al. 2017	15	18
Farhoody et al. 2023	6	7
Doman et al. 2015	20	15
Faudot et al. 2012	13.5	20
Galloway et al. 2014	20	16
Gaurier et al. 2013	20	18
Gaurier et al. 2015	20	14
Guo et al. 2018	25	20
Wang et al. 2007, Shi et al. 2016	50	20
Zhang et al. 2021	50	15
Watanabe et al. 2023	50	20
Allmark et al. 2020, Ordonez-Sanchez et al. 2019, Ellis et al. 2018	20	18
Nuernberg et al. 2018	70	20
Porter et al. 2020	20	17
Seo et al. 2016	20	8
Slama et al. 2021	28	19
Song et al. 2012	11.43	8
Average		**16.0**

As the available kinetic energy flux scales with the cube of the flow speed (equation 1.8), the upper regions of the water column typically contain the highest energy densities. This makes shallower turbine submersion depths attractive to developers aiming to maximize energy capture. However, while these upper layers offer greater energy potential, they also subject turbines to higher loading forces, as structural loads scale with the square of the flow speed (Adcock et al. 2020). Furthermore, the upper water column is influenced by wave- and current-induced velocity fluctuations, which increases the likelihood of dynamic stall (Adcock et al. 2020). Figure 1.19 shows three characteristic velocity profiles from site measurements, illustrating the influence of waves and currents as an example of a flow in nature (Encarnacion et al. 2019). Greenwood et al. (2019) also provides flow velocity profiles from real life measurements.

1.4.5. Froude number

The Froude number (Fr) is a dimensionless parameter describing the ratio of inertial to gravitational forces in free-surface flows (Munson et al. 2012). It is particularly relevant in the study of hydrokinetic turbines operating in free-surface flows, where gravity influences the velocity profile and wave interactions:

$$Fr = \frac{U_\infty}{\sqrt{gL}}, \tag{1.11}$$

with U_∞ the inflow velocity, g gravitational acceleration, and L the characteristic length. The choice of L depends on the study: some use water depth (Chamorro et al. 2013a; Luznik et al. 2013), others turbine diameter (Watanabe et al. 2023). For surface wave tests, water depth is most appropriate (Galloway et al. 2014). With deep-water conditions (Newman 1977), rotor diameter is commonly used instead.

The average Froude number in the literature survey is found to be 0.37, indicating that most studies operate in a subcritical flow condition ($Fr < 1$), where gravitational effects dominate (Munson et al. 2012). Since many studies did not report Fr, values were recalculated here using the same equation (1.11) with rotor diameter as the characteristic length to ensure consistency.

1.4.6. Reynolds number

The Reynolds number (Re) characterizes the ratio of inertial to viscous forces in the flow (Munson et al. 2012):

$$Re = \frac{\rho \cdot V \cdot L}{\mu} = \frac{V \cdot L}{\nu} \tag{1.12}$$

where ρ is the density of the water, V is the characteristic flow velocity, L is the characteristic length, μ is the dynamic viscosity of the fluid and ν is the kinematic viscosity.

There are two common choices for characteristic length in turbine design, the first being the chord length typically taken at 75% blade length (local), and secondly the rotor radius (global). For a radius based Reynolds number, the characteristic velocity will be the free-stream velocity U_∞, whereas for a chord based Reynolds number, it will be the relative velocity U_{rel}. The equation for relative velocity is:

$$U_{rel} = \sqrt{U_\infty^2 + (\Omega \cdot r)^2} \tag{1.13}$$

where Ω is the rotational speed and r the radial position (usually $0.75R$). This means the relative velocity experienced by the blade depends on both the inflow velocity and the rotational velocity of the blade.

Scaling

Reynolds number scaling is one of the most relevant scaling techniques for hydrokinetic turbines, as it directly affects blade dynamics and flow separation. However, achieving Reynolds similarity is often impractical in model-scale tests due to the high velocities required (Doman et al. 2015).

Effects on performance

The lift and drag coefficients are largely dependent on the Reynolds number, see Whelan et al. (2011), where the performance is improved for larger Reynolds numbers (decreased drag and increased lift). Because full-scale turbines operate at much higher Re, it is important that the results of testing are representative of those expected for a full-scale tidal turbine (Draycott et al. 2019). It is therefore advantageous to operate in Reynolds independent conditions when performing model tests (Mason-Jones et al. 2012), where C_p and C_t are stable with little changes in inflow velocity (Porter et al. 2020). While the exact Reynolds independence threshold varies between designs (Munson et al. 2012), previous studies provide useful guidelines. For a 0.828 m rotor, independence was reached at $Re \approx 5 \times 10^5$ (Porter et al. 2020), suggesting this as a practical benchmark for similar scales.

Although global Re (based on diameter and U_∞) is useful for scaling, local chord-based Re is more relevant for blade section hydrodynamics. Increasing inflow velocity helps achieve representative Re and reduces scaling discrepancies.

1.4.7. Thrust and torque

Torque (Q) and thrust (T) are the key loads governing turbine performance and structural behavior. Torque is the moment generated by blade lift and drag, producing power through:

$$P_{turbine} = Q \cdot \Omega \tag{1.14}$$

with Ω being the rotational rotor speed.

Thrust is the axial force from the flow on the rotor, arising from the lift and drag components aligned with the inflow direction. It affects axial loading, structural stability, and wake development (Manwell et al. 2009). The direction of the forces is visible in figure 1.20, which highlights how torque and thrust can be measured with a transducer. On blade level, the torque and thrust direction are highlighted in figure 1.7.

1.4.8. Blade root bending moment

The blade root bending moment represents the hydrodynamic loading moment at the blade root (Manwell et al. 2009). It peaks near the root, where flapwise (thrust-driven) forces dominate over edgewise (torque-driven) forces (figure 1.7 and 1.6). Only a few studies provide quantitative values, summarized in table 1.3, where the first value represents the flapwise bending moment and the second value is the edgewise bending moment. These indicate that flapwise moments scale primarily with inflow velocity,

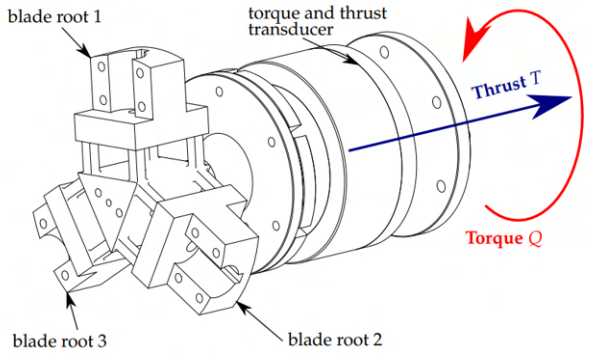

Figure 1.20: Torque and thrust transducer from Martinez et al. (2021).

while edgewise moments depend mainly on rotor speed. Waves can increase the blade loadings even further as demonstrated by Galloway et al. (2014) and Draycott et al. (2019).

Direct measurement of bending moments requires specialized force transducers, which likely explains why such data are scarce. These loads are mainly of interest for structural rather than performance assessment.

1.5. Summary and research questions

Section 1.1.2 introduced the main research aim and highlighted specific gaps in the literature, such as the limited understanding of wave-induced effects, the lack of structural data for 3D-printed blades, and the absence of detailed turbine design documentation. The subsequent review in this chapter provided a broader context, quantifying design and performance trends across 37 model-scale studies and identifying recurring limitations.

From this review, several key patterns emerge. Most studies employed three-bladed rotors with an average diameter of 0.68 m, typically using NACA 6-series or NREL S814 foils. Parameters such as pitch, chord, and thickness were examined, along with hub and nacelle dimensions, blockage effects, and tank size. Performance data showed an average maximum C_p of 0.39 and C_t of 0.79, typically at tip-speed ratios between 3 and 7. These values provide realistic benchmarks for the design and testing of the present turbine.

Scaling laws are a key limitation of model-scale testing. While Froude similarity is usually maintained to capture free-surface effects, Reynolds similarity is rarely achieved because model tests operate below the Reynolds-independence threshold. Structural data remain sparse: only 10 of 37 studies reported torque or thrust values, and blade root bending moments were seldom measured. Together, these findings emphasize the need for a model-scale turbine that not only achieves efficient hydrodynamic performance, but also allows systematic evaluation of structural loads.

Research questions and thesis structure

The goal of this thesis is to design and experimentally validate a model-scale hydrokinetic turbine for future experiments. The main research question is repeated here:

How can a model-scale hydrokinetic turbine be designed, constructed, and tested to ensure structural integrity, cost-effectiveness, and compatibility with existing experimental studies while enabling accurate performance evaluation for future research?

To address this main question, the following sub-questions are formulated:

1. *What role can actuator disc theory and BEMT play in estimating turbine performance parameters, and how can these predictions guide the design process?*
2. *How can the nacelle be designed to ensure mechanical stability, structural robustness, and practical integration with the measurement system, while remaining cost-effective and adaptable to future testing needs?*

3. *Which blade and hub design choices best balance structural integrity and hydrodynamic efficiency, and what is their impact on turbine performance?*
4. *How can the constructed turbine blades and hub be tested and evaluated to validate structural integrity and assess the accuracy of performance predictions, ensuring readiness for future experiments?*

The thesis is organized as follows. Chapter 1 reviews past model-scale turbine studies, defines terminology, and compiles the dimensional and performance parameters used later. It then formulates the research question, approach, and design requirements. Then chapter 2 develops the actuator disc and momentum theory framework for hydrokinetic turbines, describes the Python implementation, compares it to reference data, and validates QBlade. It ends with defining motor and sensor requirements. Chapter 3 describes the sensor and motor integration, cost constraints, nacelle design, and preliminary structural checks. Chapter 4 specifies the hub interface, blade geometry and design iterations, presents performance predictions based on this and introduces the wave inflow theory used later. It also presents structural experiments performed on the 3D printed blade. Chapter 5 describes the experimental procedure and results. It start with describing the facility, model and instrumentation, control protocol, and data processing. Then it presents the results under steady current and wave conditions, including the tip deflection observations. Afterwards, the main findings are discussed and evaluated. Finally, the conclusion chapter answers the research question and outlines recommendations for future work.

1.6. Design requirements and dimensioning

Based on the literature review, key parameters for the turbine can now be defined. These form the basis for performance predictions using actuator disc theory and allow early specification of nacelle components. This ensures that the detailed design can proceed while waiting for certain parts to be delivered.

1.6.1. Design requirements

The goal is to design a model-scale HAHT that operates under both steady and wave conditions, while remaining adaptable for future tests and comparable to past research. The design is subject to requirements grouped by performance, structural, and experimental criteria. These serve as references for decision-making throughout the design process and are numbered for later use.

Performance requirements

Previous studies reported an average optimal TSR of 5.1 (section 1.4.3), with most turbines operating between 3 and 7. This range is therefore adopted here, with the lower bound also supported by recent tests on large 3D-printed blades by Lande-Sudall et al. (2023), who had an optimal TSR of 3.5. Within this range, the target efficiency is set to $C_p > 0.35$ and $C_t > 0.7$, to be at least within 10% of the optimal performance of literature averages. To ensure scalability, the turbine should operate in a regime of global Reynolds number independence ($Re \geq 5 \times 10^5$, see section 1.4.6), while maximizing local Reynolds numbers where possible.

1.1 The turbine must operate optimally at a TSR between 3 and 7.

1.2 The target power coefficient (C_p) should exceed 0.35.

1.3 The target thrust coefficient (C_t) should exceed 0.7.

1.4 The turbine must operate in a regime where (global) Reynolds number independence is achieved.

Structural requirements

The blades will be manufactured using 3D printing to allow rapid, low-cost prototyping and replacement. Sufficient stiffness is required to prevent excessive deformation and ensure consistent hydrodynamic behavior. The blades must be detachable and feature an adjustable pitch mechanism for testing flexibility. The nacelle must be watertight to protect drivetrain and instrumentation, and both nacelle and tower must withstand operational loads without significant pitch or yaw motion. Compatibility with the TU Delft towing carriage and mounting interface is also required.

2.1 The turbine blades must be 3D-printed and must not fail under expected operational loads.

2.2 Blade deformation should stay within acceptable limits to maintain consistent hydrodynamic behavior.

2.3 The hub must allow for easy detachment and replacement of the blades.

2.4 The blade pitch must be adjustable to accommodate various test conditions.

2.5 The nacelle must be watertight to protect internal drivetrain and instrumentation.

2.6 The tower and nacelle must be able to withstand forces with minimal movement.

2.7 The turbine must be compatible with the TU Delft towing carriage and mounting interface.

Measurement and experimental requirements

The turbine must allow accurate measurement of torque and rotational speed, enabling determination of C_p and TSR. Thrust is less critical and may initially be omitted to save costs, or measured indirectly using existing equipment. The drivetrain must provide speed control across the full operating range. Blockage must remain below 5% (section 1.3.8). Finally, the system must mount rigidly to the TU Delft towing carriage for repeatable testing.

3.1 The system must allow accurate torque measurement and, if within budget, thrust as well.

3.2 Rotational speed must be measurable with sufficient precision.

3.3 The drivetrain must support speed control over the full range to maintain the desired TSR.

3.4 The blockage ratio in the tank must remain below 5%.

1.6.2. Dimensioning

With the design requirements established, the next step is to define the main dimensional and operational parameters: rotor diameter, number of blades, inflow velocity, and tip-speed ratio. These govern hydrodynamic forces, structural loading, power output, and are needed as the inputs for early performance predictions using actuator disc theory and BEMT. They also specify drivetrain components that must be ordered in advance due to long delivery times.

Number of Blades

The number of blades is a fundamental design choice, influencing turbine performance, wake structure, and structural loading. Based on the literature review (section 1.3.1), a three-bladed rotor is selected for this design.

Three blades are the most commonly used configuration in hydrokinetic turbine research (table 1.1), ensuring alignment with previous studies. This amount provides a good balance between efficiency and mechanical smoothness by reducing torque ripples compared to two-bladed rotors, while avoiding the complexity and increased loading of four or more blades. Balanced shaft loading also enhances stability during torque and thrust measurements, which is important for experimental reliability.

Reported performance for three-bladed turbines typically yields C_p values between 0.30 and 0.50 (table 1.1, figure 1.18), aligning with the target efficiency of this design. While additional blades can further reduce bending moments on individual blades, they also introduce higher costs and manufacturing complexity. Two-bladed rotors, though simpler, often experience greater unsteady loading and torque fluctuations.

Finally, the use of 3D printing lowers production cost and allows flexibility in blade replacement, reducing the penalty of testing alternative blade numbers. Nevertheless, a three-bladed rotor provides the most suitable compromise between performance, structural integrity, comparability with past research, and practical feasibility.

Rotor diameter selection

Rotor diameter is the next critical design choice, as it governs power output, hydrodynamic forces, structural loading, and experimental feasibility. Based on the literature review and the TU Delft towing tank constraints, several factors are considered.

From momentum theory, power and thrust scale with R^2, while torque scales with R^3. A larger diameter therefore increases energy capture but also structural loads, which is a concern for 3D-printed blades.

Blockage effects further constrain the design: with a towing tank depth of 2.3 m and cross-sectional area $A = 9.71\,\text{m}^2$, the 5% blockage criterion limits the rotor to about $0.78\,\text{m}$. Figure (1.21) is provided, where the intersection between the dashes lines gives a point that lies in the middle of what other researchers have done in towing tank experiments. The vertical dashed line represents the maximum allowable diameter based on the 5% blockage threshold. The horizontal line represents the cross-sectional area of the towing tank.

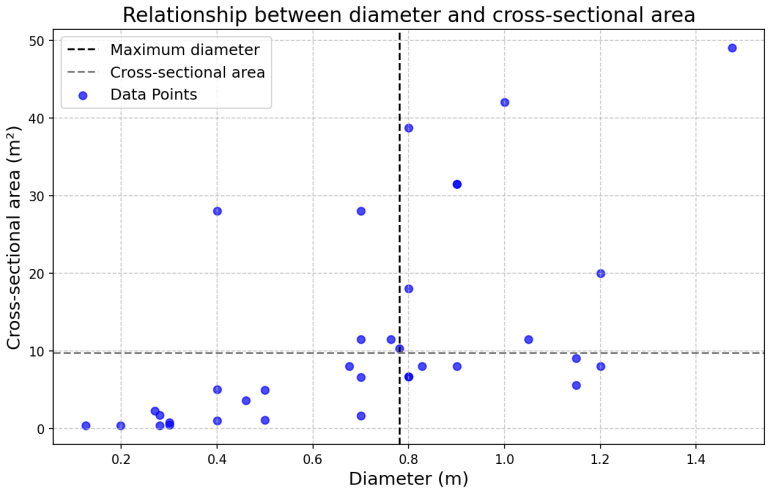

Figure 1.21: Maximum diameter based on cross-sectional area and maximum blockage ratio of 5%.

Structurally, longer blades produce higher bending moments and potential deformation. While 3D printing allows rapid prototyping and modularity, stiffness imposes an upper limit. This effect will be verified experimentally, but for now maximizing rotor diameter within blockage limits follows common practice (Guo et al. 2018).

Facility constraints are also relevant. Adequate clearance must be maintained, at least one radius above the bottom and half a radius below the free surface (Kolekar et al. 2015). With a $0.74\,\text{m}$ rotor, this requirement is satisfied without approaching tank limits. When testing with waves waves in the future, the submergence depth might change.

The rotor diameter affects the global Reynolds number directly, which is a key parameter for achieving Reynolds number independence (see 1.4.6). A larger diameter will also indirectly increase the local Reynolds number, by enlarging the chord length. The target of $Re > 5 \cdot 10^5$ can be met for this diameter range as discussed in section 1.4.6, depending also on the inflow velocity. To reach the Reynolds independence based on global Reynolds number, the inflow velocity will have to be at least 0.68 m/s for a diameter of 0.74 m.

In summary, a rotor diameter of $0.74\,\text{m}$ is selected. This value balances performance potential, Reynolds similarity, and structural feasibility while keeping the blockage ratio at 4.4% for maximum tank depth, comfortably below the 5% threshold.

Hub diameter and nacelle length

The hub diameter must balance internal space for drivetrain components (shaft, motor, torque sensor, and wiring) with minimal efficiency loss from increased blockage. Oversizing reduces the effective swept area, while undersizing compromises structural strength. Literature values for similar rotor sizes range from approximately 0.05-$0.13\,\text{m}$, averaging about $0.10\,\text{m}$ (see figure 1.9a), which is therefore the target range.

Small variations in hub size have little effect on performance, since the root region contributes minimally to thrust and torque (sections 1.3.6 and 1.3.7). Structural integrity is the main criterion here, rather than hydrodynamics. Once the hub diameter is finalized, the strength and structural behavior of the hub-blade assembly will be validated to ensure safe and stable operation under expected loading conditions.

The nacelle length is dictated by internal mechanics and component layout, with little impact on turbine efficiency. Previous studies show no clear trend (figure 1.9b), though most remain below 1 m. A nacelle shorter than this is preferred to reduce forces on the strut and material use.

Flow velocity

The inflow velocity sets the available kinetic power and directly influences Reynolds number, turbine loading, and performance ($P_{available} \propto U_{\infty}^3$). Small changes in velocity therefore have a large effect on thrust, torque, and power.

Using Froude scaling with a representative full-scale diameter of 16 m (average from table 1.4) and the present rotor of 0.74 m gives a scale factor of 21.5. This corresponds to model velocities of 0.22-1.08 m/s for real-world currents of 1-5 m/s (section 1.4.4). Figure 1.22 shows the relation between the velocities on full scale compared to the velocities at model-scale, for different turbine sizes.

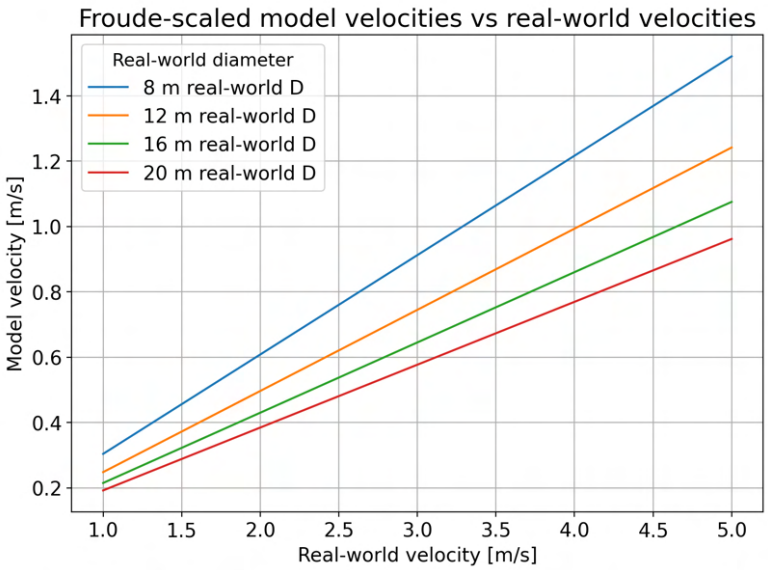

Figure 1.22: Comparison between real-world and model-scale velocities for different turbine sizes.

These inflow velocities align with the literature, where most studies tested between 0.4 and 1.2 m/s. For this design, a range of 0.5-1.0 m/s is chosen. This is representative of real-world currents of 2.3-4.6 m/s, matches literature practice, and remains feasible for TU Delft's facility. It also avoids excessive hydrodynamic loads on 3D-printed blades.

The BEMT analysis in combination with experimental testing of the blades will determine what will be the maximum allowable speed from a structural point of view. Going lower in minimum inflow velocity is still possible based on this analysis, but the Reynolds number will then become increasingly lower as will become clear later on.

Tip-speed ratio

The turbine will be optimized for a TSR of 5.0, ensuring that geometry and loading conditions fall within experimentally validated regions, and aligning with previous research (see section 1.4.3). For varying inflow velocities, this implies adjusting the rotational speed to maintain desired TSR. A broader test range of TSR between 3 and 7 will also be explored to characterize off-design performance and possible mismatches between the predictions and the experimental outcomes. Figure 1.23 shows the different rotational speeds that can be expected for the turbine, for the different flow velocities and tip-speed ratios that will be investigated.

Selecting a TSR of 5 balances efficiency and structural loading. Higher TSRs reduce inflow angles and allow thinner blade profiles, but increase centrifugal loads. Lower TSRs increase torque and angle of attack, raising the risk of dynamic stall. If in the end the blade turns out to be too thin for a TSR of 5, lowering the optimal TSR could help design a thicker blade, while still being efficient for a different optimal TSR.

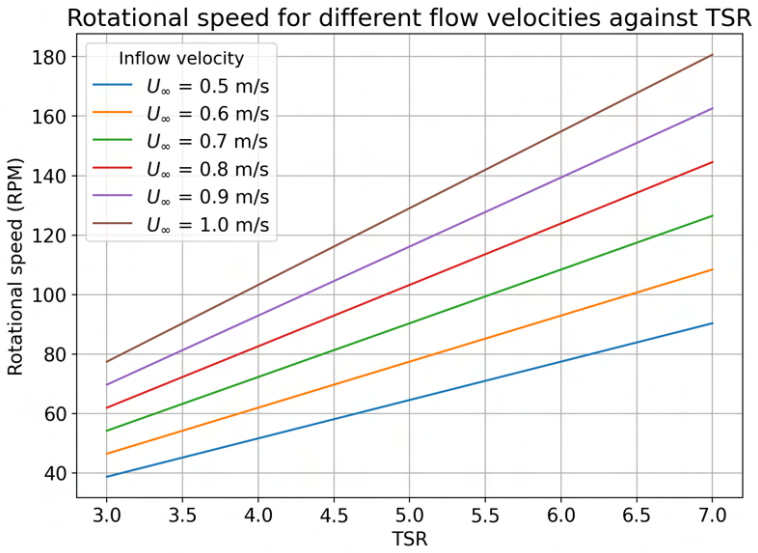

Figure 1.23: Relation between rotational speed and tip-speed ratio of a 0.74 m diameter rotor.

Summary

Below is a summary of the key design parameters from this chapter, which form the basis for further turbine development and component selection. Some of the values may still change during the design process. An additional column has been added showing linearly scaled full-scale values using a scale factor of 21.5. While parameters such as (hub) diameter and nacelle length are scaled geometrically, these values are only indicative and may not reflect practical real-world dimensions.

Table 1.5: Summary of main design parameters

Parameter	**Model value**	**Full-scale value (scale: 21.5)**
Number of blades	3	3
Rotor diameter D	$0.74\,\mathrm{m}$	$16\,\mathrm{m}$
Blockage ratio	4.4%	-
Hub diameter aim	$\sim 0.10\,\mathrm{m}$	$\sim 2.15\,\mathrm{m}$
Nacelle length aim	$< 1\,\mathrm{m}$	$< 21.5\,\mathrm{m}$
Inflow velocity U_∞	$0.5 - 1.0\,\mathrm{m/s}$	$2.3 - 4.6\,\mathrm{m/s}$
Design tip-speed ratio TSR	5.0	5.0
Operating TSR range	$3.0 - 7.0$	$3.0 - 7.0$
Target power coefficient C_p	> 0.35	> 0.35
Target thrust coefficient C_t	> 0.70	> 0.70
Reynolds number (global)	$> 5 \cdot 10^5$	$> 1.1 \cdot 10^7$
Blade material	3D print	Composite / Steel
Pitch control	Manually adjustable	Active pitch control
Compatibility	TU Delft towing tank	Real-world deployment

2

Performance prediction

After evaluating the existing literature on hydrokinetic turbines, this chapter introduces performance prediction methods. First, the working principles of a hydrokinetic turbine are examined using actuator disc theory, providing initial estimates of thrust and torque. These results are then refined with Blade Element Momentum Theory (BEMT), which accounts for the actual blade geometry. Together, these methods guide the preliminary turbine design by predicting the main forces acting on the rotor. This chapter will answer the following research question:

What role can actuator disc theory and BEMT play in estimating turbine performance parameters, and how can these predictions guide the design process?

2.1. Actuator disc theory

One of the most widely used simplified approaches to describe the behavior of axial-flow turbines is the actuator disc theory. In this model, the turbine rotor is idealized as a uniformly loaded, porous disc that imposes a distributed resistance to the incoming flow (Chen et al. 2019). It assumes steady, incompressible, inviscid flow with no drag, an infinite number of blades, uniform thrust, a non-rotating wake, and equal static pressure far upstream and downstream (Manwell et al. 2009). Although first developed for wind turbines, the same principles apply to hydrokinetic turbines, with adaptations for confinement and free-surface effects (Garrett et al. 2007).

Figure 2.1 illustrates the control volume associated with actuator disc theory. It shows a streamtube passing through the disc, with also showing flow velocity and pressure changes across the disc plane. The incoming velocity U_∞ slows down to U_D at the disc and further to U_w in the wake. This reduction in velocity forms the basis for deriving thrust, power, and efficiency using conservation of mass and momentum.

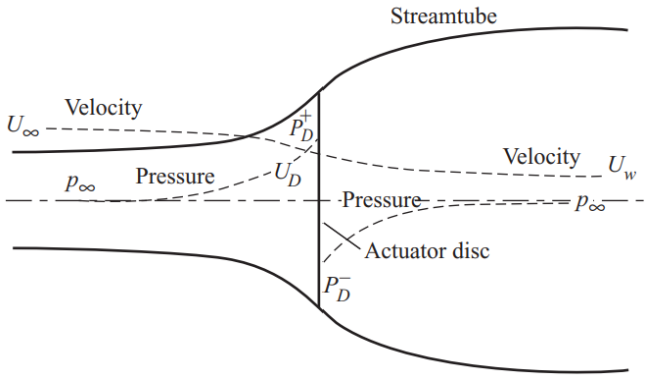

Figure 2.1: Velocity and pressure distribution across an actuator disc (Burton et al. 2011).

The following analysis follows the explanation of Burton et al. 2011. Firstly, continuity can be applied assuming constant density, giving:

$$\rho A_D U_D = \rho A_\infty U_\infty = \rho A_w U_w$$

From the continuity equation, it follows that the mass flow rate is constant through the stream tube. To determine how pressure changes relate to velocity changes, Bernoulli's equation is applied to the control volume, upstream and downstream of the actuator disc (but not across it, since energy is extracted):

$$p_\infty + \frac{1}{2}\rho U_\infty^2 = p_D^+ + \frac{1}{2}\rho U_D^2 \tag{1}$$

$$p_\infty + \frac{1}{2}\rho U_w^2 = p_D^- + \frac{1}{2}\rho U_D^2 \tag{2}$$

Subtracting (2) from (1) then gives the pressure jump across the disc:

$$(p_D^+ - p_D^-) = \frac{1}{2}\rho(U_\infty^2 - U_w^2) \tag{3}$$

The pressure difference across the disc produces a net thrust force, which can be expressed either from the pressure difference over the disc area (Newton's second law) or from the momentum change across the control volume:

$$T = (p_D^+ - p_D^-)A = \frac{1}{2}\rho A(U_\infty^2 - U_w^2) \tag{4}$$

Using momentum theory, thrust is also related to the change in velocity, where $\dot{m}$ represents the mass flow rate in kg/s:

$$T = \dot{m}(U_\infty - U_w) = \rho A_D U_D (U_\infty - U_w) \tag{5}$$

Equation (4) and (5) are explained in Manwell et al. 2009, combining these two equations leads to:

$$U_D = \frac{1}{2}(U_\infty + U_w) \tag{6}$$

This equation demonstrates that the velocity at the rotor plane, U_D, lies exactly halfway between the upstream velocity U_∞ and the far-wake velocity U_w. This motivates the definition of the axial induction factor a, which quantifies the flow reduction at the disc and enables the derivation of performance parameters such as the power and thrust coefficients, including the theoretical maximum power coefficient known as the Betz limit. From equation (6), the far-wake velocity can be expressed in terms of a and the inflow velocity:

$$U_D = U_\infty(1-a) \quad \Rightarrow \quad U_w = U_\infty(1-2a) \tag{7}$$

Substituting this into the power expression using equation (5) and (7), gives the absolute power:

$$P = T \cdot U_D = 2\rho A U_\infty^3 a(1-a)^2 \tag{8}$$

Normalizing this by the available power, the power coefficient can be defined as:

$$C_p = \frac{P}{\frac{1}{2}\rho A U_\infty^3} = 4a(1-a)^2 \tag{2.1}$$

Taking the derivative of this equation with respect to the axial induction factor and setting this to zero to gain the maximum value, $\frac{1}{3}$ is found as a solution. Filling this in gives:

$$C_p = \frac{16}{27} = 0.593$$

This represents the theoretical maximum efficiency of an ideal turbine in an unbounded flow and is well-known as the Lanchester-Betz limit. This limit will in practice never be reached due to rotation of the wake behind the rotor, finite number of blades with tip losses and non-zero drag values (Manwell et al. 2009).

The thrust coefficient can also be defined as a function of the axial induction factor:

$$C_t = \frac{Thrust}{\frac{1}{2}\rho U_\infty^2 A} = 4a(1-a) \tag{2.2}$$

Figure 2.2 shows the variation of C_P and C_T with axial induction factor a. The model is valid for $a \leq 0.5$; beyond this, the model is not valid anymore due to wake effects and non-physical predictions. Corrections such as the Glauert model are then required (Burton et al. 2011). In practice, this limit is not restrictive, since maximum power output occurs at $a = \frac{1}{3}$.

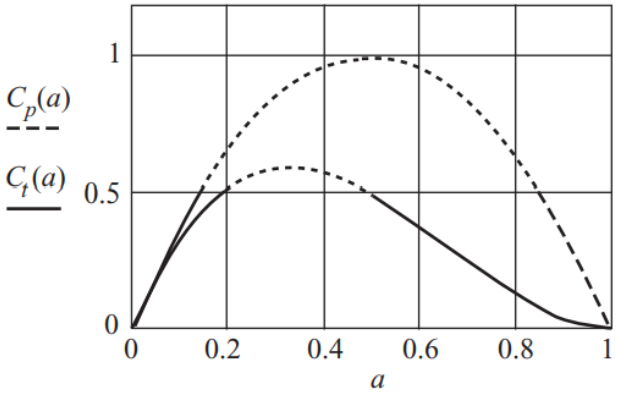

Figure 2.2: Variation of C_P and C_T with axial induction factor a. (Burton et al. 2011)

2.2. Angular momentum theory

The actuator disc model does not account for rotor-induced swirl, and therefore cannot predict torque. To account for rotational effects in an axial-flow turbine, the one-dimensional momentum theory is extended with angular momentum theory in Burton et al. (2011). This addition introduces the angular induction factor a', which accounts for the rotational velocity imparted to the flow due to the rotor blades. The relation between a and a' can be expressed as follows according to Manwell et al. (2009), it only holds for maximum power in each angular ring:

$$a' = \frac{1-3a}{4a-1} \tag{2.3}$$

The angular momentum theory evaluates the change in angular momentum across an annular ring at radius r, through which mass flows with a certain swirl induced by the turbine. The torque δQ generated by a differential element then follows from conservation of angular momentum:

$$\delta Q = 2\pi r \delta r \rho U_\infty (1-a) \cdot 2a' r^2 \Omega \tag{2.4}$$

Similarly, the axial thrust acting on the same annulus is given by:

$$\delta T = 2\pi r \delta r \rho U_\infty^2 (1-a) \cdot 2a \tag{2.5}$$

These expressions assume steady, inviscid, axisymmetric flow and neglect viscous losses and wake rotation. In this thesis, they are implemented in a custom Python model to estimate local thrust and torque distributions along the blade (see Appendix B). By integrating these quantities over the span, global loads and performance can be obtained, providing a first-order prediction of turbine behavior. This approach enables rapid estimation of thrust, torque, and power across a range of tip-speed ratios, even before detailed blade geometry is defined. The corresponding ideal power output is then calculated as:

$$P = Q \cdot \Omega \tag{2.6}$$

2.3. Hydrokinetic turbine differences

Although actuator disc theory was originally developed for wind turbines, its principles are frequently applied to hydrokinetic turbines as well. Water's density is about 800 times greater than that of air, so small turbines can generate comparable amounts of energy as larger wind turbines (Yuce et al. 2015). Flow conditions are also often more unsteady due to wave-current interactions, leading to fluctuating loads and possible dynamic stall (Polagye et al. 2010, Adcock et al. 2020).

A more fundamental limitation of classical actuator disc theory is that it assumes operation in an unbounded flow. In reality, hydrokinetic turbines often operate in confined environments such as rivers, tidal channels, or laboratory flumes, where the flow cannot expand freely around the rotor. This introduces blockage effects (see chapter 1.3.8). For blockage ratios above about 5%, corrections are needed since confinement alters local velocities and increases the theoretical maximum power extraction.

To address this, Garrett et al. (2007) introduced a modified actuator disc formulation that accounts for blockage. The power coefficient C_p becomes:

$$C_p = \frac{16}{27}(1 - B)^{-2} \tag{2.7}$$

This results in an increased power coefficient for an increasing blockage ratio. More advanced frameworks for tidal channels have been suggested by for example Vennell (2013) and Chen et al. (2019). Additionally, Bahaj et al. (2007) proposed a method for correcting confined test results to equivalent free-stream values, enabling better comparison across experimental setups and theoretical models.

These extensions highlight the limitations of the classical actuator disc model in realistic or confined environments. However, for model-scale blade design under controlled, low-blockage conditions, it remains a useful first approximation. In this thesis, blockage corrections are not included in the Python model (Appendix B), since most approaches focus on power only and reliable formulations for thrust and torque are lacking. Consequently, the presented model is only intended for low-blockage conditions. For configurations with higher blockage ratios, the predicted performance might underestimate the true energy extraction potential.

2.4. Implementation into Python

Using actuator disc and angular momentum theory, the ideal performance of a hydrokinetic turbine can be estimated with a simplified Python model that predicts thrust, torque, and power from first principles.

2.4.1. Induction factors

The axial induction factor a and tangential induction factor a' are required to compute thrust and torque along the blade span using equations 2.4 and 2.5.

Table 2.1: Axial induction factor a and maximum power coefficient $C_{P,\text{max}}$ from Manwell et al. (2009).

TSR	a	$C_{P,\text{max}}$
0.5	0.2983	0.289
1.0	0.3170	0.416
1.5	0.3245	0.477
2.0	0.3279	0.511
2.5	0.3297	0.533
5.0	0.3324	0.570
7.5	0.3329	0.581
10.0	0.3330	0.585

To obtain continuous estimates of the optimal axial induction factor a and the corresponding maximum power coefficient $C_{P,\text{max}}$, a rational (multiple polynomial functions) curve fitting approach was applied to the dataset in table 2.1, originally presented in Manwell et al. (2009). It shows the optimal a values

corresponding to different tip-speed ratios. The same function was used for both quantities:

$$f(TSR) = a + \frac{b}{TSR + c} + \frac{d}{(TSR + c)^2} \tag{2.8}$$

The fitted parameters for each case are:

- For $a_2(TSR)$: $a = 0.3324$, $b = 0.0123$, $c = 0.7415$, $d = -0.0679$
- For $C_{P,\text{max}}(TSR)$: $a = 0.5901$, $b = 0.0141$, $c = 1.1166$, $d = -0.8097$

Figure 2.3 shows the resulting curves, which are used to provide continuous estimates at different tip-speed ratios.

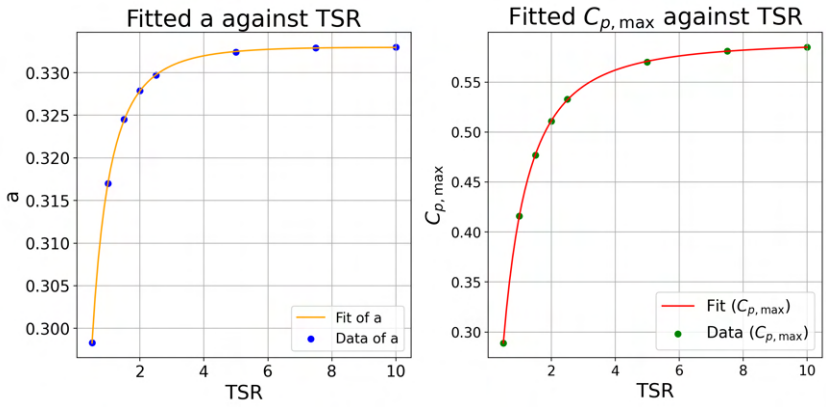

Figure 2.3: Fitted curve of axial induction factor a and C_p as a function of TSR.

The tangential induction factor a' is then obtained from a using equation 2.3. Figure 2.4 shows the resulting spanwise distributions of a and a' for a rotor with $R = 0.74$ m, hub diameter $D_{\text{hub}} = 0.12$ m, and a tip-speed ratio of $TSR = 5$. A tip loss correction (section 2.5.5) is applied in figure 2.4b, which reduces a and a' to zero at the blade tip, lowering the predicted torque and thrust. The only additional input needed is the number of blades.

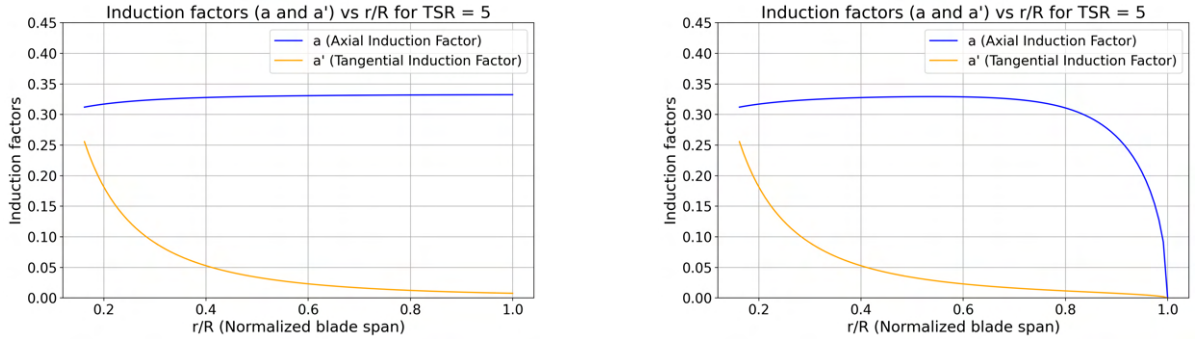

(a) Without tip loss correction

(b) With tip loss correction

Figure 2.4: Axial and tangential induction factors along the blade span for $R = 0.74$ m, $D_{\text{hub}} = 0.12$ m, $TSR = 5$.

2.4.2. Implementation

The rotor blade is discretized into annular elements, and the local torque and thrust are computed using equations 2.4 and 2.5. Summing over the span gives:

$$Q = \sum \delta Q = \sum 4\pi\rho U_\infty (1-a) a' r^3 \Omega \delta r \tag{2.9}$$

$$T = \sum \delta T = \sum 4\pi\rho U_\infty^2 (1-a) a\, r\, \delta r \tag{2.10}$$

The extracted power follows from equation 2.6, and the power coefficient from equation 2.1. The Python implementation (Appendix B) includes hub diameter, which is excluded from load generation since no lift or drag occurs there. If not specified, hub size can be estimated from literature values (table 1.1, fig. 1.9a). The other required input parameters are rotor diameter, inflow velocity, tip-speed ratio, and water density. Based on these fundamental parameters, the model provides a first-order estimate of rotor performance, later compared to BEMT predictions and experimental data.

2.4.3. Comparing results to model-scale tests

This section compares Python-calculated torque and thrust to literature values, using the same inflow velocity and tip-speed ratio conditions (table 1.3). Only ten studies reported explicit torque or thrust measurements. Studies that only reported C_t and C_p values, without directly listing thrust or torque, are excluded from this comparison.

Because actuator disc theory neglects wake rotation and viscous losses, its torque and thrust predictions are generally expected to exceed experimental values. This trend holds for most cases in table 2.2, although a few studies report measured values that exceed the actuator disc predictions. Several factors may contribute to these discrepancies.

A likely explanation is the absence of blockage correction in the Python model. This appears to be the case for Payne et al. (2017), whose experimental values exceed the theoretical predictions. Their estimated blockage of at least 16% is well above the 5% threshold (see 1.3.8). Similarly, Galloway et al. (2014) did not apply blockage correction despite operating at 7% blockage, which likely explains the torque overprediction in their data. The measurement data in this cases comes from Galloway et al. (2010).

Guo et al. (2018) reported slightly higher thrust than actuator disc predictions, possibly due to wave effects or measurement error. The strongly deviating results of Farhoody et al. (2023) likely stem from measurement error, as the data deviates more strongly than other studies.

Equation 2.11 can be used to check the results, where the ratio between the measured C_p and the theoretical C_p from actuator disc theory is computed. Multiplying this ratio by the predicted actuator disc torque provides a corrected estimate of the experimental torque that aligns within 10% for most cases.

$$Q_{extimated} = \frac{C_{p,measured}}{C_{p,theoretical}} \cdot Q_{actuator\ disc} \tag{2.11}$$

This method relies on the direct relationship between torque and power, as described in equation 2.6. While it is not useful in the design phase, since C_p is unknown, it provides a valuable check for validation. Deviations mainly reflect the fact that actuator disc theory assumes ideal energy extraction, while in practice additional losses reduce the measured power. Experimental uncertainties may also contribute.

Table 2.2: Comparison of experimental and Python-calculated (P) thrust and torque values. Experimental values are rounded to the precision of the source; some were digitized from graphs and may be less accurate. Python values are rounded to two decimals. TL indicates inclusion of the tip loss factor; C_p values also account for tip losses.

Article	T (ex)	Q (ex)	T (P)	Q (P)	T (P,TL)	Q (P,TL)	C_p(ex)	C_p(P)
Chen et al. 2017b	5	0.17	9.66	0.26	8.45	0.23	0.31	0.44
Payne et al. 2017	385	18	325.48	17.43	302.55	16.19	0.50	0.49
Farhoody et al. 2023	70	5.8	438.91	21.34	409.01	19.82	0.21	0.48
Doman et al. 2015	84	6.8	190.17	12.89	167.45	11.37	0.29	0.42
Faudot et al. 2012	320	17	330.31	21.06	307.57	19.57	0.43	0.48
Galloway et al. 2014	135	8.0	174.05	6.99	160.47	6.46	0.5	0.476
Luznik et al. 2013	-	0.44	25.25	0.64	23.12	0.59	0.38	0.470
Allmark et al. 2020	250	15	274.43	21.71	242.56	19.20	0.38	0.476
Lande-Sudall et al. 2023	-	2.9	59.87	3.74	52.85	3.30	0.40	0.476
Guo et al. 2018	110	3.5	101.30	4.21	93.26	3.89	0.44	0.485

Table 2.2 presents the results from the actuator disc model both with and without the tip loss correction applied. As expected, including tip loss lowers predictions and brings them closer to experiments. The studies of Payne et al. (2017), Galloway et al. (2014), and Farhoody et al. (2023) are excluded from the final comparison due to high blockage or questionable data.

Considering only the remaining studies, torque predictions overestimate experiments by 43.7% without tip loss correction and 29.2% with correction. For thrust, the deviations are 44.9% and 27.9%, respectively. This confirms that tip loss correction improves accuracy, and it will therefore be applied in all subsequent predictions.

The largest deviations between experimental results and momentum theory predictions occur at low power coefficients (C_p). This is expected, as momentum theory does not account for blade characteristics and is derived for peak efficiency conditions. The extended actuator disc model, which includes the tangential induction factor a', is based on maximum power extraction (see equation 2.3), limiting its accuracy to a single design tip-speed ratio. As a result, the model performs well near peak efficiency, but becomes less accurate under off-design conditions or when predicting maximum loads.

At high loading, the theory often underpredicts thrust, as it cannot capture boundary layer effects, separation, or radial pressure gradients (Burton et al. 2011). For highly loaded turbines ($a > 0.5$), momentum theory becomes invalid due to breakdown of one-dimensional assumptions and wake reversal (Manwell et al. 2009).

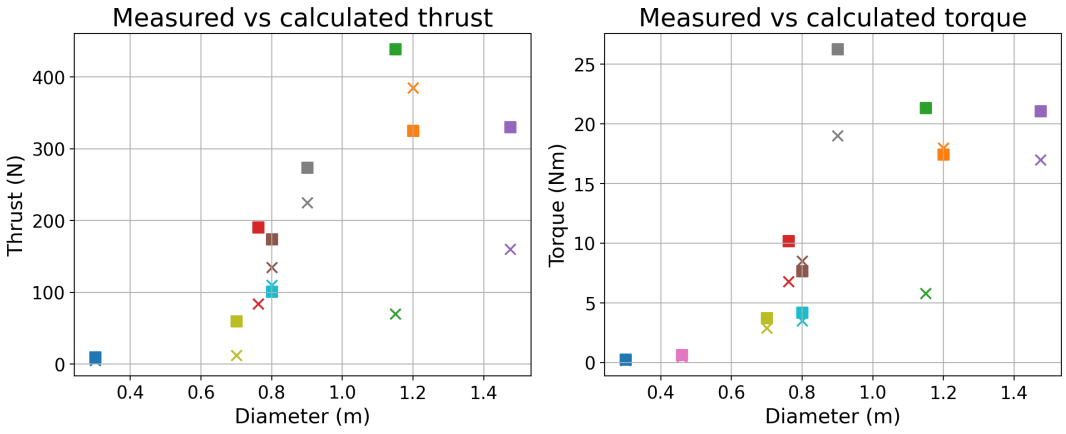

Figure 2.5: Comparison of the actuator disc values with the measured values. The cross-signs are the measured values, and the squares the actuator disc values.

Figure 2.5 illustrates the results. In most cases actuator disc predictions exceed measured values, as expected, with deviations explained above. Additional assumptions were required for hub size, since it was not always reported. Estimates were 0.1 m for Chen et al. (2017b) and Luznik et al. (2013), 0.25 m for Faudot et al. (2012), and 0.15 m for Galloway et al. (2014). For Allmark et al. (2020), who tested in multiple facilities, the dataset from the CNR-INM tank with the highest measured C_p was selected.

Overall, the results align with theoretical expectations, with deviations explained by the factors above. The actuator disc model offers rapid estimates of thrust and torque from a few basic inputs (blade number, rotor and hub diameter, inflow velocity, tip-speed ratio). Greater accuracy would require blade-specific lift and drag data, but this would increase complexity and computational cost. Section 2.6.6 compares these results to BEMT, which incorporates detailed blade geometry and flow.

Figure 2.6 also illustrates the distribution of thrust and torque along the blade span. Although the details would differ for a real turbine with defined foil geometry, the general pattern is clear. Contributions rise with distance from the hub and decrease near the tip due to tip losses. This supports the reasoning in sections 1.3.6 and 1.3.7, where it is shown that structural strength is typically prioritized near the hub, while hydrodynamic performance is favored near the tip.

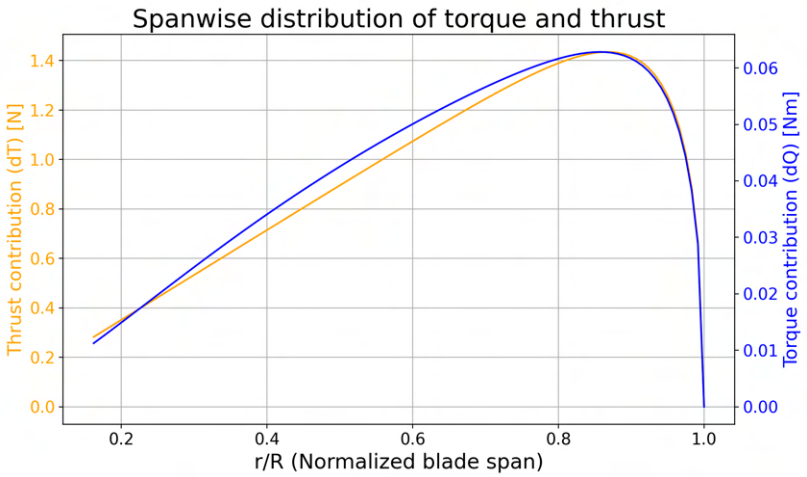

Figure 2.6: Spanwise distribution forces for a 0.74 m rotor with 0.12 m hub diameter, with a incoming flow velocity of 0.75 m/s and a TSR of 5.

2.5. Momentum theory vs Blade Element Momentum Theory

Blade Element Momentum Theory (BEMT) combines momentum theory with blade element theory, incorporating lift and drag on individual blade sections. This enables more accurate predictions of local forces, power output, and induced velocities along the span. The formulation described here is derived directly from Burton et al. (2011) and builds upon the actuator disc theory previously introduced.

2.5.1. Relative velocity and angle of attack

In the section on Reynolds (1.4.6), the relative velocity was introduced as:

$$U_{\text{rel}} = \sqrt{U_\infty^2 + (\Omega r)^2} \tag{2.12}$$

This expression represents the undisturbed geometric relative velocity experienced by a blade element at radius r. However, In BEMT, induction effects modify this velocity: the axial factor a reduces the axial component, and the tangential factor a' increases the swirl. The presence of induction alters the local inflow, and the true (induced) relative velocity experienced by the blade becomes:

$$U_{\text{rel,ind}} = W = \sqrt{(U_\infty(1-a))^2 + (\Omega r(1+a'))^2} \tag{2.13}$$

This effective relative velocity forms the basis for calculating the local hydrodynamic forces. The angle ϕ describes the direction of the incoming flow relative to the rotor plane for each blade element:

$$\tan\phi = \frac{U_\infty(1-a)}{r\Omega(1+a')} \tag{2.14}$$

From this, the corresponding trigonometric relations are:

$$\sin\phi = \frac{U_\infty(1-a)}{W} \qquad \text{and} \qquad \cos\phi = \frac{r\Omega(1+a')}{W} \tag{2.15}$$

The angle of attack α experienced by the local foil is determined by subtracting the local blade pitch angle β from the inflow angle (see figure 1.7):

$$\alpha = \phi - \beta \tag{2.16}$$

From α, the lift and drag coefficients $C_L(\alpha)$ and $C_D(\alpha)$ are obtained. These coefficients are typically obtained from experimental foil measurements or tabulated data. In this project, these are provided by QBlade, which computes C_L and C_D for different angles of attack, using its built-in XFoil module.

2.5.2. Momentum theory component

The expressions for the differential thrust and torque derived in the actuator disc theory section (see equations 2.9 and 2.10) are retained in BEMT:

$$\delta T = 4\pi r \rho U_\infty^2 a(1-a)\,\delta r \tag{2.17}$$

$$\delta Q = 4\pi r^3 \rho U_\infty \Omega a'(1-a)\,\delta r \tag{2.18}$$

These momentum-based expressions are then matched with blade element theory, which will be explained next, allowing the induction factors a and a' to be solved consistently.

2.5.3. Blade element theory component

From two-dimensional foil theory, the lift and drag per unit span are:

$$L = \frac{1}{2}\rho W^2 c C_L \tag{2.19}$$

$$D = \frac{1}{2}\rho W^2 c C_D \tag{2.20}$$

Where W is the true relative velocity, c is the local chord length, and C_L and C_D are the lift and drag coefficients corresponding to the local angle of attack.

A key assumption of BEMT is that each blade element acts independently, experiencing hydrodynamic forces equivalent to those on an identical, isolated foil in steady, two-dimensional flow at the same angle of attack. This implies that three-dimensional flow effects are neglected. Similarly, the flow through each annular control volume (annulus) is assumed to be influenced only by the forces within that annulus, with no radial interaction between adjacent elements. While this condition holds strictly only if the axial induction factor is constant along the span, experimental studies by Lock (1924) showed that the assumption of radial independence provides acceptable accuracy in practice.

Under these assumptions, the sectional lift and drag forces can be directly projected into an axial component opposing the incoming flow and a tangential component driving rotor rotation:

$$F_x = L\cos\phi + D\sin\phi \tag{2.21}$$

$$F_\theta = L\sin\phi - D\cos\phi \tag{2.22}$$

The total axial thrust and torque generated by all N blades in an annular element of width δr, using blade element theory:

$$\delta T = N \cdot F_x \cdot \delta r = \frac{1}{2}\rho W^2 N c (C_L\cos\phi + C_D\sin\phi)\,\delta r \tag{2.23}$$

$$\delta Q = N \cdot F_\theta \cdot r \cdot \delta r = \frac{1}{2}\rho W^2 N c (C_L\sin\phi - C_D\cos\phi) r\,\delta r \tag{2.24}$$

The differential power extracted by an annular blade element is given by:

$$\delta P = \Omega\,\delta Q \tag{2.25}$$

Summing all elements gives the total power and the power coefficient C_p.

2.5.4. The Blade Element Momentum Theory (BEMT)

BEMT is formed by combining the two previously described approaches: momentum theory and blade element theory. Momentum theory relates the rotor's effect on the flow field to global force expressions, while blade element theory models the local forces acting on individual blade sections based on their geometry and foil characteristics.

By equating thrust and torque from both approaches, the induction factors a and a' (unknowns in momentum theory) are related to the blade geometry and hydrodynamic properties (c, ϕ, C_L, C_D). Solving these equations for each annular section yields the local flow and forces acting on the rotor. Equating axial and tangential force expressions gives:

$$\frac{1}{2}\rho W^2 Nc(C_L\cos\phi + C_D\sin\phi) = 4\pi r\rho U_\infty^2 a(1-a) \tag{2.26}$$

$$\frac{1}{2}\rho W^2 Nc(C_L\sin\phi - C_D\cos\phi)r = 4\pi r^3\rho U_\infty \Omega a'(1-a) \tag{2.27}$$

These nonlinear equations are solved iteratively for a and a', after which thrust, torque, and power can be integrated over the span. To simplify the equations, they are often expressed non-dimensionally using the local blade solidity σ (equation 1.4), yielding:

$$\frac{a}{1-a} = \frac{\sigma(C_L\cos\phi + C_D\sin\phi)}{4\sin^2\phi} \tag{2.28}$$

$$\frac{a'}{1+a'} = \frac{\sigma(C_L\sin\phi - C_D\cos\phi)}{4\sin\phi\cos\phi} \tag{2.29}$$

These equations provide a direct relationship between the local flow conditions (via ϕ, see equation 2.14), the blade geometry (via σ, see 1.4), and the hydrodynamic response of the foil (via C_L and C_D, see 2.19), forming the mathematical core of BEMT. Since both a and a' appear implicitly (through their effect on ϕ and W), these equations must be solved iteratively. The solution typically begins with initial guesses for a and a', after which ϕ and α are computed, followed by the corresponding C_L and C_D. The induction factors are then updated, and the process is repeated until the values of a and a' converge within a specified tolerance.

2.5.5. Tip Loss Correction

To account for the reduced hydrodynamic loading near the blade tip due to the finite number of blades, Prandtl introduced the first tip loss correction factor (Prandtl 1921). Glauert (1935) later reformulated this correction into a more numerically convenient form, which has become the standard in modern BEMT implementations. In this thesis, the formulation will be referred to as Glauert's correction, although in the literature it is often still called the Prandtl tip loss. The factor F is given by:

$$F = \frac{2}{\pi}\cos^{-1}\left(e^{\frac{-N(R-r)}{2r\sin\phi}}\right) \tag{2.30}$$

Where N is the number of blades, R the rotor radius, r the radial location, and ϕ the inflow angle. The tip loss factor modifies the momentum equations as (Zhong et al. 2024; Burton et al. 2011):

$$\frac{a}{1-a} = \frac{\sigma(C_L\cos\phi + C_D\sin\phi)}{4F\sin^2\phi} \tag{2.31}$$

$$\frac{a'}{1+a'} = \frac{\sigma(C_L\sin\phi - C_D\cos\phi)}{4F\sin\phi\cos\phi} \tag{2.32}$$

Applying this correction is essential to avoid overpredicting thrust and torque near the tip, which would otherwise result from the idealized assumptions of BEMT (Burton et al. 2011). For wind turbines, neglecting tip losses typically leads to 5-15% overprediction (Boatto et al. 2023), especially at high tip-speed ratios or under high loading. Although less experimental data exists for hydrokinetic turbines, the Glauert factor is geometry-based and has been successfully applied in several studies (Wilden et al. 2023), supporting its validity in water as well. For the actuator disc theory, it has already proven to give more accurate results (see section 2.4.3). The tip loss factor makes it possible to account for the effect of a finite number of blades and ensures the induction factor smoothly approaches zero at the tip, providing more realistic force distributions (Burton et al. 2011).

Despite its simplicity, Glauert's correction has limitations. The main assumption is that it is only valid for lightly loaded turbines or in other words, a low thrust coefficient, where flow separation and complex wake dynamics remain minimal (Zhong et al. 2024). This also means that wake expansion is ignored, which is acceptable at low loading, but becomes less accurate when thrust is high and the flow becomes more complex.

To address these issues, several researchers have proposed modified tip loss corrections (Zhong et al. 2024). These improve accuracy in high loading conditions and high TSR regimes while maintaining the mathematical structure of the original formulation. Nevertheless, the original Glauert tip loss factor remains the most widely used in wind and hydrokinetic turbine modeling, due to its simplicity and proven reliability in most operating conditions (Zhong et al. 2024).

2.6. Validating QBlade

QBlade is used in this thesis as the BEMT model. It is an open-source simulation tool developed at the Technical University of Berlin and has been applied in numerous hydrokinetic studies (Alamian et al. 2020; Ferraiuolo et al. 2024; Farhoody et al. 2023). A dedicated section in the documentation describes its application to marine turbines (Marten et al. 2024), which mainly requires setting the density and kinematic viscosity to that of water. Reynolds number and the critical amplification factor N_{crit} must also match operating conditions, as discussed in section 2.6.5. Version 2.0.8.6 of QBlade, published in March 2025, was used in this thesis.

QBlade provides both BEMT and a more advanced lifting line free vortex wake method, as well as structural and drivetrain modules. In this thesis only the steady BEMT solver is used, to estimate rotor forces and power output under uniform inflow. Qblade's documentation includes validation cases and further studies have confirmed its accuracy (Chihaia et al. 2016).

A limitation of QBlade is that it is not able to simulate wave loading on the turbine at this point. The only waves it can generate is for floating wind turbines. Thus, an alternative solution for this will have to be used, see section 4.7.1.

The software also offers a user-friendly interface, built-in integration with Xfoil for foil polar generation, and plotting features that facilitate quick turbine design and performance evaluation. These capabilities, combined with its widespread use in academic research, make QBlade a suitable and accessible tool. An alternative is NREL's OpenFAST, for which a hydrokinetic-specific version was released in early 2025 (National Renewable Energy Laboratory 2025). This may become a viable option in the future, but it was not available at the start of this project.

2.6.1. Reference study for BEMT validation

To validate QBlade and ensure correct simulation settings, selected experimental studies were reproduced. Only three papers provided sufficient blade and load data for this purpose: Doman et al. (2015), Guo et al. (2018), and Allmark et al. (2020).

Among these, the study by Guo et al. (2018) serves as the primary reference. Their 0.8 m rotor closely matches the 0.74 m rotor in this design, providing a conservative estimate since the slightly larger reference turbine will experience higher loads. The reported hub diameter of 0.1 m also aligns with the target hub size here.

Furthermore, the reference study used a NACA 63-8xx blade profile, which was identified in section 1.3.4 as the most frequently adopted foil in hydrokinetic turbine research. This reinforces the relevance of the comparison, as the blade type and general geometry are representative of current practices.

The reference turbine was also tested under wave-induced unsteady inflow, matching the intended operating conditions of the present design. The availability of detailed measurements makes this study a suitable benchmark for validating BEMT simulations and ensures that the predicted loads used for drivetrain design are grounded in experimental data.

2.6.2. Polar definition

For the case of Guo et al. (2018), lift and drag coefficients were generated with QBlade's XFoil module for a range of angles of attack. The required input values for the polar definition are shown in figure 2.7.

When generating hydrodynamic lift and drag coefficients using the integrated XFOIL tool, the e^n method is used to predict when a laminar boundary layer will become unstable and transition to turbulence. In this approach, small disturbances in the boundary layer are assumed to grow exponentially until a critical amplification factor, N_{crit}, is reached, at which point transition is triggered. The value of N_{crit} reflects the stability of the boundary layer to free-stream disturbances: higher values correspond to low-turbulence environments where disturbances must grow more before transition, while lower values represent more turbulent conditions where transition occurs earlier (Drela 1989). For wind turbines, $N_{\text{crit}} = 9$ is recommended, but towing tank conditions are typically more turbulent, so lower values have shown to improve agreement with experiments.

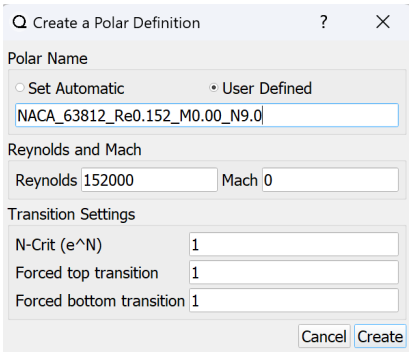

Figure 2.7: Polar definition tab QBlade.

El-Shahat (2020) found that $N_{\text{crit}} = 1$ produced the best agreement with tidal turbine experiments, as it better represents transition behavior in towing tanks and yields more realistic lift and drag curves. Higher values, such as $N_{\text{crit}} = 9$, caused premature stall prediction and less accurate thrust and power estimates. Following this validated approach, $N_{\text{crit}} = 1$ is used here to generate hydrodynamic coefficients, ensuring reliable input data.

In Xfoil-based simulations, the boundary layer transition from laminar to turbulent flow can be either predicted using the e^n method, or prescribed manually using forced transition parameters. The ”forced top transition” and ”forced bottom transition” settings seen in figure 2.7 define the non-dimensional chordwise location, ranging from 0 (leading edge) to 1 (trailing edge), at which transition is artificially imposed on the suction and pressure sides of the blade (Marten et al. 2024). This approach might be used to simulate the effect of surface roughness for example. In this study, forced transition was left at the default of 1, so transition is predicted naturally by the e^n method.

A chord based Reynolds number of 1.52×10^5, reported by Guo et al. (2018) for $U_\infty = 0.68$ m/s at 75% span, was used for generating the lift and drag curves, adopted for all validation simulations. QBlade is then able to generate the values for other Reynolds numbers when needed, this is also explained into more detail when talking about a multi-polar simulation in chapter 5.3.

Finally, the Mach number was set to zero, representing incompressible flow, which is valid since turbine speeds are far below sonic velocity (Munson et al. 2012).

2.6.3. Lift and drag visualization

After importing the NACA 6-series foils into QBlade, lift and drag curves were generated with the integrated XFoil tool, using the standard angle of attack range from $-15°$ to $20°$ in $0.2°$ steps. From the calculated values, the $360°$ polar plots can be made as explained into more detail in 4.6.5. The lift and drag plots for the different NACA 6-series foils that are used by Guo et al. (2018) are exported from QBlade and plotted in figure 2.8.

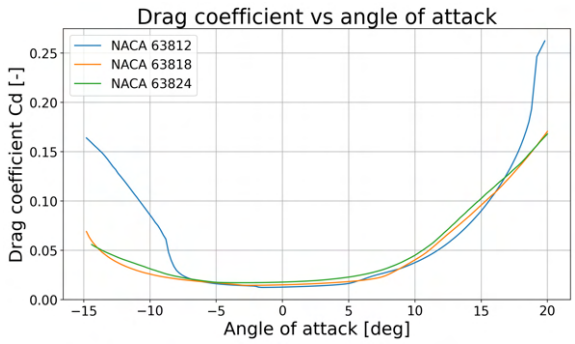

(a) Drag coefficient graphs for the NACA 6-series foils.

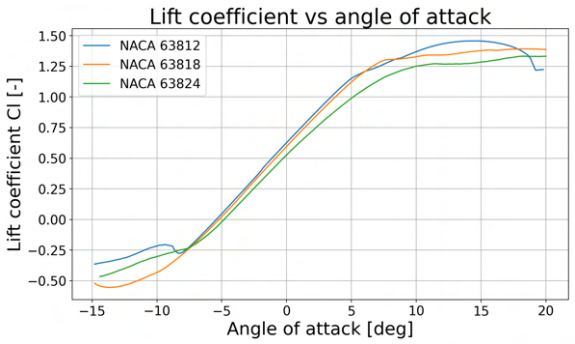

(b) Lift coefficient graphs for the NACA 6-series foils.

Figure 2.8: Lift and drag coefficients of the different NACA foils used by Guo et al. (2018).

The differences between the lift and drag seem relatively small between the different foils in figure 2.8. However, when looking at the lift to drag ratio, the differences become more clear and it is visible that, as expected, the thinnest foil (NACA 63812) has the highest lift to drag ratio. For this reason, this foil was used in the region that contributes most to the power generation, the tip region. Near the root, a thicker foil was used, likely for structural considerations, namely something close to the NACA 63824. This foil has approximately a 40% lower peak lift to drag ratio, which is significant when it comes to power generation.

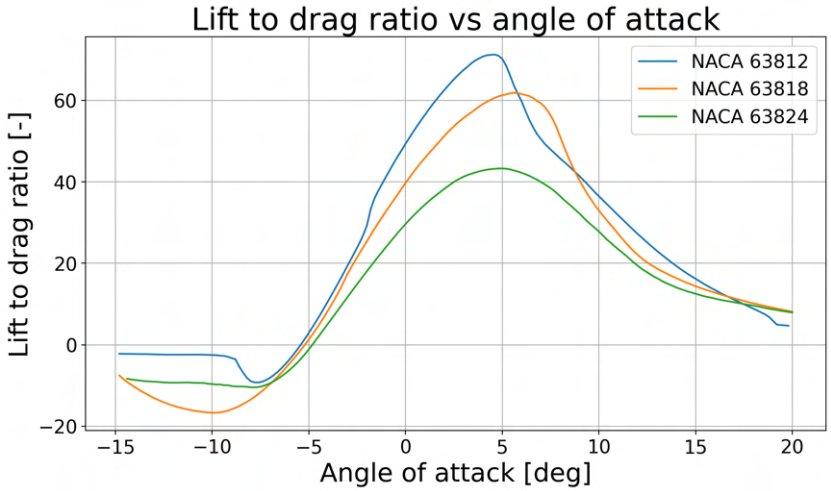

Figure 2.9: The lift to drag ratio for the different foils.

2.6.4. Simulation

After importing the blade geometry of Guo et al. (2018) (figure 2.10), the case was simulated in QBlade. The predicted C_p and C_t values follow the reference results closely, with deviations generally within 5% (figure 2.11). Below a TSR of 4 slightly larger differences occur, while above this value the predictions remain consistently within the 5% margin. Overall, the current BEMT method slightly underpredicts the measured parameters.

r/R	r (mm)	Pre-Twist (deg)	Chord (mm)	t/c (%)
0.125	50	20.0	32.0	99.9
0.200	80	19.5	67.9	22.0
0.300	120	16.5	60.7	20.0
0.400	160	13.3	51.9	18.3
0.500	200	11.6	47.6	14.8
0.600	240	9.4	43.3	14.2
0.700	280	7.3	40.1	13.6
0.800	320	5.2	37.6	13.1
0.900	360	2.7	35.3	12.5
1.000	400	0.0	33.2	12.0

Figure 2.10: The blade definition of Guo et al. (2018).

Several factors may explain the discrepancies. First, Guo et al. (2018) employed a modified BEMT formulation that included added mass terms and wave-induced inflow effects, giving improved accuracy under unsteady loading compared to the current method.

Minor deviations also arise from geometric simplifications. The original blade definition specified foil profiles at ten radial positions with precise thickness-to-chord ratios. Here, standard NACA 6-series foils available in discrete thickness steps (12%, 15%, 18%, etc.) were interpolated to approximate intermediate values, with thickness deviations up to 0.75%. In addition, details such as the exact twist-axis position along the chord were not available, introducing further approximations.

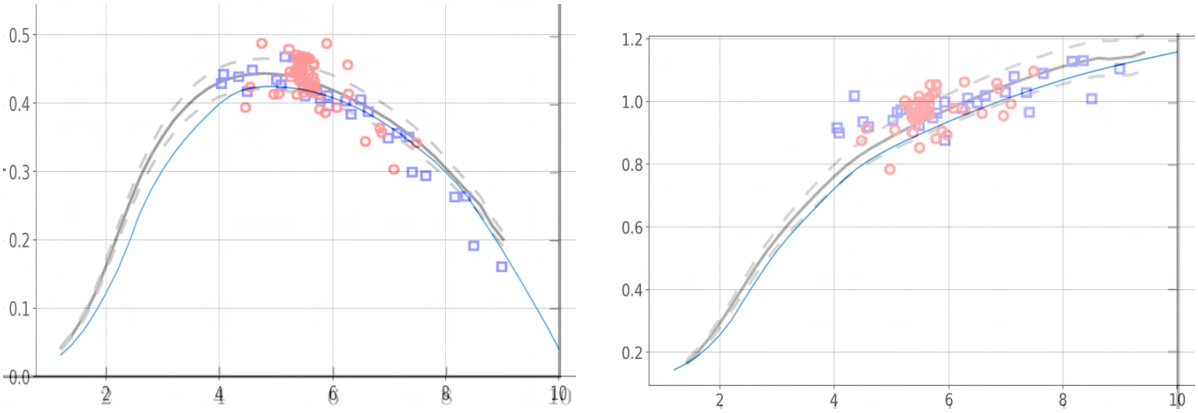

(a) C_p against TSR.

(b) C_t against TSR.

Figure 2.11: Comparison between BEMT (black line) and experimental values (red representing waves cases and blue without waves) from Guo et al. (2018) to current BEMT method (blue line).

2.6.5. Corrections and Ncrit verification

To ensure validity of the simulations at this early stage of the project, two verification steps were performed: applying QBlade's correction models and testing sensitivity to the N_{crit} parameter. First, figure 2.12 shows the effect of corrections on the predicted power coefficient C_p.

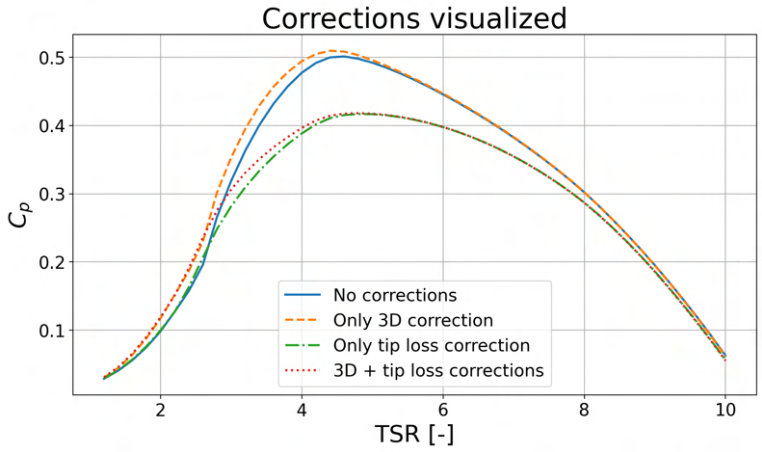

Figure 2.12: The influence of the different correction factors from QBlade on the C_p value.

Among the available corrections, tip loss has the largest influence, substantially reducing C_p. The 3D correction is an empirical enhancement based on the work of Snel et al. (1992), designed to mitigate the limitations of classical BEMT in modeling separated and three-dimensional flow near blade root and tip regions (Marten et al. 2024). It accounts for 3D effects like radial flow phenomena not captured in 2D foil polars. By modifying local lift and drag coefficients, it significantly improves the accuracy of load predictions in areas where spanwise flow and separation effects are non-negligible. The actual effect of this correction is relatively small as can be seen in figure 2.12, it only slightly increases performance at low TSR. Both the tip loss- and 3D corrections were applied in this study.

The DTU poly-BEM correction (Madsen et al. 2020), developed for large wind turbines in turbulent inflow, was not applied, as the present 0.74 m rotor operates under controlled, uniform towing tank conditions where its effect is negligible. Including this correction leads to a minor increase in C_p for high TSRs, but the effect is relatively small and it would add complexity without significant benefit. It is therefore also not shown in figure 2.12.

As a further check for model validation, the influence of the N_{crit} parameter on the BEMT results was evaluated. Three different values of N_{crit} were tested to assess their impact on the hydrodynamic performance predictions, with the results shown in figure 2.13.

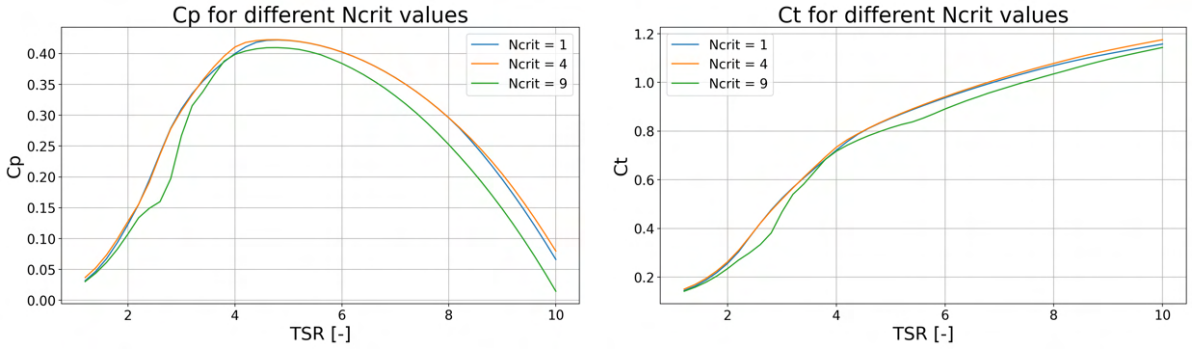

(a) C_p graph for different $Ncrit$ values.

(b) C_t graph for different $Ncrit$ values.

Figure 2.13: Differences in C_p and C_t curves for multiple N_{crit} values.

The most notable observation is that a value of $N_{crit} = 9$, leads to noticeably lower predictions for both thrust and torque, and results in less smooth performance curves. Although this value is frequently recommended for wind turbine simulations, it appears to be less suitable for hydrokinetic turbines, as also suggested by El-Shahat (2020). The differences between $N_{crit} = 1$ and $N_{crit} = 4$ are negligible within the relevant TSR range (3-7).

Based on these results and the recommendation of El-Shahat (2020), a value of $N_{crit} = 1$ was adopted. This ensures the small differences observed with Guo et al. (2018) are not due to incorrect N_{crit} or correction settings, and confirms the chosen parameters are suitable for the remainder of this work.

2.6.6. Torque and thrust comparison

Although C_p and C_t are directly related to torque and thrust, verification against experimental loads remains important for motor and sensor selection. Like mentioned, Doman et al. (2015) and Allmark et al. (2020) also provided detailed blade information in combination with measured torque and thrust values, so these studies are included now. They are imported into QBlade the same way the turbine of Guo et al. (2018) was imported. The Reynolds numbers were calculated based on 75% chord length and relative velocity, resulting in a Reynolds number of $2.09 \cdot 10^5$ for Allmark et al. (2020) and $1.23 \cdot 10^5$ for Doman et al. (2015). The results are summarized in table 2.3, which also includes actuator disc (AD) values for comparison.

Table 2.3: Comparison experimental values and BEMT calculation. AD is short for actuator disc.

Reference	T, exp	T, BEMT	T, AD	Q, exp	Q, BEMT	Q, AD	TSR
Guo et al. 2018	110	107	93	3.4	3.4	4.21	5.8
Allmark et al. 2020	250	270	243	14	14.5	19.2	3.6
Doman et al. 2015	70	102	167	5.8	7.3	11.4	3.5

Table 2.3 shows that BEMT consistently predicts torque and thrust more accurately than the actuator disc method. For example, in Guo et al. (2018) and Allmark et al. (2020), BEMT aligns well with experimental data, while actuator disc theory underestimates thrust and, in the latter case, overestimates torque.

The results for the Doman et al. (2015) turbine deviate more significantly, although the results are much closer to the measured values as calculated with actuator disc theory. This discrepancy can likely be attributed to the low C_p of this specific case, namely 0.29. Since low-efficiency operation is not the focus of this research, this outlier is not considered critical for the current application. Besides, the BEMT method over predicts torque and thrust for most cases, which adds additional safety for when the calculated values deviate slightly.

Overall, BEMT proves to be the more reliable method for force prediction under the operating conditions relevant to this study. With this validation complete, the load prediction method is now considered sufficiently accurate for the next phase of the project: the selection and sizing of the motor and sensor.

2.7. Motor and sensor selection

Validated BEMT predictions were used to define the loads for motor and sensor selection. Since the final detailed rotor design is not yet fixed, the 0.8 m rotor from Guo et al. (2018) was taken as a reference, providing a slightly conservative estimate compared to the 0.74 m design. Simulations were performed for tip-speed ratios (TSR) from 1 (start-up) to 7, and for both minimum and maximum inflow velocities. The maximum expected torque for the reference turbine is approximately 10.5 N/m at a TSR of 3, and $U_\infty = 1$ m/s. The highest thrust load occurs at a TSR of 7, giving a maximum thrust of 255 N (figure 2.14).

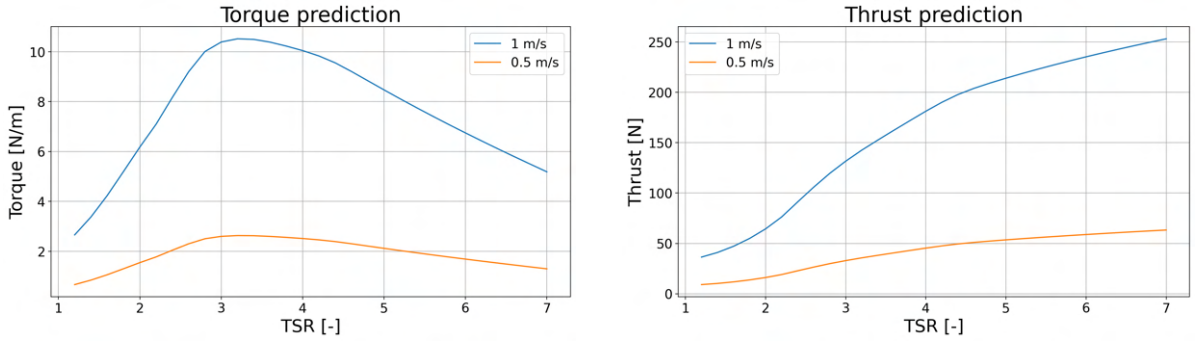

(a) Torque prediction.

(b) Thrust prediction.

Figure 2.14: Predicted torque and thrust for a 0.8 m rotor.

As shown in section 2.6, the BEMT can underestimate performance values with approximately 10% for some cases. Increasing the calculated maximum values with 10% and and rounding it up, gives 12 N/m torque and 280 N thrust for steady flow conditions. The corresponding rotational speed is 160 rpm at a TSR of 7, for 1 m/s. For a TSR of 3 and inflow velocity 0.5 m/s, the rotational speed is 36 rpm, this corresponds to the lowest rotational speed during testing.

As the turbine will also be tested in waves, it can be expected that the loading will increase further. Guo et al. (2018) showed that even relatively small wave amplitudes can significantly influence the rotor loads. In this study, thrust and torque values reached up to 50% of the mean load when exposed to regular waves with a period of 1.6 s and a height of 14 cm. Even small perturbations of the mean inflow velocity (15%) could already lead to these large cyclic load variations. This means the temporary maximum value for torque could increase up to 18 N/m and the thrust value up to 420 N. These values will be taken as maximum value, to ensure the motor and sensor will not be overloaded.

The turbine's maximum mechanical power in steady inflow is about 106 W. Including gearbox losses of 5-10% gives 95-106 W at the motor. With torque fluctuations of up to $\pm$50%, peak mechanical power may reach 160 W. To cover this range, the motor should have a continuous power rating of at least 120 W and a peak capacity of 160 W. These requirements, summarized in table 2.4, form the basis for motor and sensor selection in the next chapter.

Table 2.4: Predicted loads and motor power requirements

Parameter	Value
Nominal torque	12 Nm
Peak torque	18 Nm
Nominal thrust	280 N
Peak thrust	420 N
Nominal rotational speed	36–160 rpm
Rated power	120 W
Peak power	160 W

3

Nacelle design

With the main design parameters established using BEMT, the nacelle can be designed. This includes selecting an appropriate motor-sensor combination, followed by the structural design of the inner nacelle. This chapter addresses the following research question:

How can the nacelle be designed to ensure mechanical stability, structural robustness, and practical integration with the measurement system, while remaining cost-effective and adaptable to future testing needs?

3.1. Sensor and motor setup

To enable both control of the rotor's rotational speed and measure the torque, three possible configurations for the drivetrain and instrumentation were considered. These setups are intended to support future testing under both steady and wave-influenced inflow conditions. Each option offers a different method for applying resistive torque to the turbine shaft to control the rotational speed and for integrating torque and speed measurement instrumentation.

Option 1: magnetic brake system

This configuration uses a dedicated magnetic brake to control the rotor speed and dissipate the power produced by the turbine. This approach has been adopted in various hydrokinetic studies, where the brake serves both to regulate the TSR and to absorb generated power, see Ferraiuolo et al. (2024). However, Lust et al. (2013) reports practical limitations, noting that TSR values below 5.5 were unattainable due to shaft binding under high braking torque.

For this setup, Magtrol recommends their TPB 25 magnetic powder brake, which offers adequate braking capacity. Given its diameter (184 mm), it is preferable to mount the brake above the waterline, as is common practice in the literature as well. The torque sensor would remain close to the rotor to maximize measurement accuracy. One advantage of this setup is future flexibility: the brake could be replaced with a motor without redesigning the entire setup as the brake is placed outside of the nacelle. This could possible offer a cheap temporary solution.

Option 2: Brushless DC motor (BLDC)

A brushless DC motor can also apply braking torque. Since BLDC motors are designed for high-speed operation, a gearbox is required to match the turbine's low-speed, high-torque range. While this reduces efficiency, it does not affect experimental validity. BLDC motors are compact relative to other options, enabling full integration in a small nacelle.

This approach is the most common in hydrokinetic turbine experiments, for example reported by Mei et al. (2024), Milne et al. (2013), Stallard et al. (2015), and Lande-Sudall et al. (2023).

Option 3: Permanent magnet synchronous machine (PMSM)

The third configuration involves using a PMSM, which can provide high torque at low speeds without a gearbox, simplifying the drivetrain. However, the motor diameter (e.g. Alxion's 190STK series, 190 mm)

exceeds the 100 mm nacelle target, requiring a redesign of the rear nacelle section (figure 3.1c).

An alternative low-cost approach considered was the use of a stepper motor, such as a NEMA 42. Though less suitable for dynamic control, stepper motors can generate relatively high resistive torque at low rotational speeds. With a diameter of approximately 156 mm, this option lies between the BLDC and PMSM in terms of space requirements. Figure 3.1 presents the three different options in a schematic drawing.

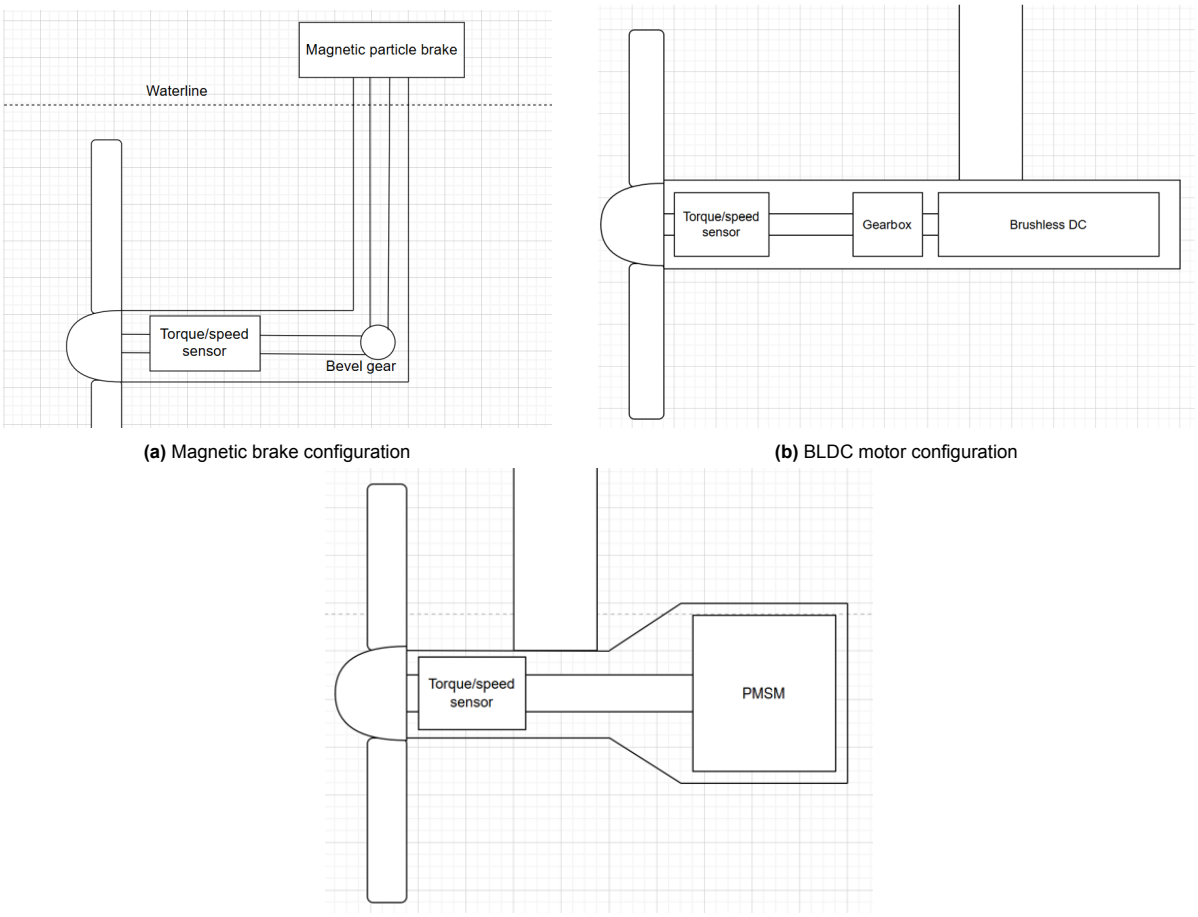

(a) Magnetic brake configuration

(b) BLDC motor configuration

(c) PMSM configuration

Figure 3.1: Schematic layouts of the three drivetrain configurations considered for the experimental setup.

Based on the trade-offs between required diameter, functionality, and integration complexity, the selected configuration will use a brushless DC motor in combination with a gearbox (figure 3.1b). This solution offers the most compact nacelle geometry, while prior experimental use and manufacturer recommendations confirm its suitability. The gearbox introduces minor efficiency and cost penalties, but braking capability, rather than power generation, remains the primary goal.

To accommodate this configuration, a waterproof nacelle will be required to protect the motor assembly, as the motor is likely not waterproof. Consequently, the torque sensor does not necessarily need to be waterproof, provided it can be housed within the same sealed compartment. In cases where external mounting is unavoidable, a waterproof sensor may still be considered as a redundancy measure.

3.2. Sensor selection

Several commercial torque sensors were evaluated based on technical specifications, integration constraints, and costs. The choice was independent of the drivetrain setup. Manufacturers with experience in hydrokinetic turbine testing, identified through the literature review, were contacted directly: Magtrol (Ferraiuolo et al. 2022), Appmeas (Payne et al. 2017, Allmark et al. 2020), and Futek. Although Futek

sensors were not used in prior studies, they have been applied in earlier TU Delft projects and were therefore included. Based on company input, five models were shortlisted. The main selection criteria were required nacelle diameter and cost, as these strongly affect nacelle integration.

Option 1 is the TS 107 sensor from Magtrol. It provides high accuracy, includes a built-in 360 ppr encoder, and supports high rotational speeds. However, it has a relatively large diameter compared to some of the alternatives and limited environmental protection (IP44).

Options 2 and 3 are both supplied by Appmeas. Option 2 is the DRWPL-II, a waterproof sensor (IP67) with high accuracy and strong axial/radial load capacity, making it suitable for submerged applications. Option 3, the DRBK-II, is a lower-cost alternative with reduced accuracy, speed range, and no keyways on the shaft. According to communication with the manufacturer, these trade-offs primarily explain the difference in price. Despite these limitations, both Appmeas sensors remain viable options, especially when paired with external encoders.

Option 4 is the TRS605 from Futek. It is extremely compact, with a 360 ppr encoder and good accuracy. However, it allows only limited axial load (requiring a thrust bearing) and is rated IP40, requiring extra sealing.

Option 5 stands apart from the other sensors. It is a customized version of the DBBSS/TSF series from Appmeas, used before in hydrokinetic turbine research (Payne et al. 2017). Unlike the other models, it is designed to rotate with the shaft, simplifying integration and allowing internal cable routing through the hollow shaft. It measures both torque and thrust, is highly robust (IP68), and reduces external cabling. However, it requires a slip ring for signal transfer and comes at higher cost. Despite this, it is an excellent candidate for submerged and dynamically loaded environments when costs is not limiting.

A summary of the shortlisted sensors is given in table 3.1, listing key parameters, minimum diameters (depending on cable routing), and price estimates. It is important to note that the cable outlet of many sensors is located at the top of the sensor, which poses integration challenges in a compact nacelle. To address this, manufacturers were asked to specify both the required sensor diameter and additional height clearance needed for cable bending. Since most sensors need a large amount of space for the cable output compared to the sensor size, different cable routing options were considered to keep the hub diameter as small as possible. Firstly, the cable could exit through the nacelle wall on top and water column to an external data system, requiring a waterproof seal, or the cable can go via internal routing through the strut, requiring the sensor the be located below the strut. This would simplify sealing, but can lead to a longer nacelle length since the strut can not be placed right behind the rotor, as it could then influence the free stream inflow into the rotor.

Property	Required (approx.)	1: Magtrol TS 107	2: DRWPL-II	3: DRBK-II	4: TRS605	5: DBBSS/TSF
Price (€)	<7000	3910	5586	2586	4394	6000
Hub D incl. cable (mm)	-	168	322	326	284	84
Hub D excl. cable (mm)	<130	126	99	103	87	84
Height (mm)	<90	85	68	72	58	84
Breadth (mm)	<90	65	50	70	38	84
Length (mm)	<150	49	92	48	59	86
Rated torque (Nm)	$\geq$18	10	20	20	20	25
Shaft diameter (mm)	-	9	15	15	16	25
Non-linearity	$\leq$0.2%	Not specified	0.1%	0.3%	0.2%	0.1%
Hysteresis	$\leq$0.2%	Not specified	0.1%	0.3%	0.1%	0.1%
Non-repeatability	$\leq$0.2%	Not specified	Not specified	Not specified	0.2%	0.05%
Full scale error	$\leq$0.2%	0.05%	0.1%	0.5%	0.5%	0.1%
Protection	$\geq$IP67	IP44	IP67	IP40	IP40	IP68
Operating temp (°C)	10 to 30	-25 to 80	0 to 60	0 to 60	-25 to 80	-20 to 80
Max rpm	>160	15000	10000	10000	7000	Not specified
Max dynamic safe overload	$\geq$100%	200%	100%	100%	150%	150%
Encoder (ppr)	$\geq$60	360	60	60	360	Not included
Max axial load (N)	>420	50	930	930	150	2500
Max radial load (N)	>50	50	90	90	30	Not specified

Table 3.1: Specifications of shortlisted torque sensors, including target requirements.

Figure 3.2 illustrates a comparison of the cable footprint for the listed sensors. The cable size and routing constraints significantly influence the total required sensor diameter. For instance, although the Futek sensor (option 4) is the smallest in core dimensions, its vertical cable outlet occupies more

height than the slightly larger Magtrol sensor (option 1), which offers a more compact footprint once cable routing is considered. The Appmeas sensors (options 2 and 3) require relatively large cable bending space as well, though custom modifications are possible. As shown in table 3.1, all four sensors exceed the 0.15 m hub diameter target and must be mounted directly below the strut.

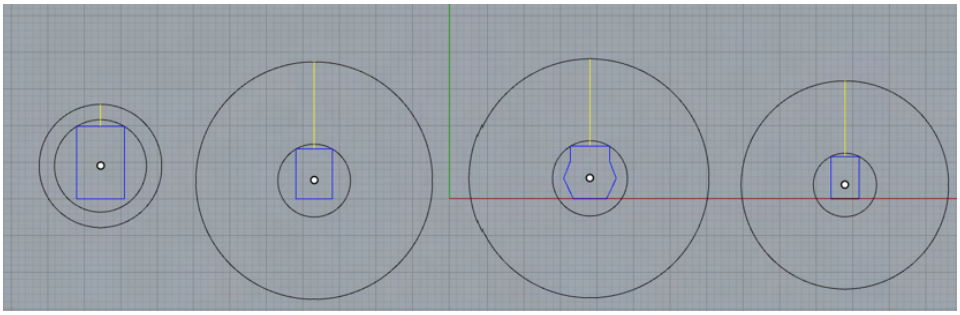

Figure 3.2: Required hub diameter visualized for the different sensors. From left to right, options 1 to 4 are shown

Option 5, also from Appmeas, offers a unique solution by routing the cables internally through the hollow shaft, eliminating external cabling and simplifying integration. This model, a custom version of the DBBSS/TSF series, has been previously applied in hydrokinetic turbine studies (Applied Measurements Ltd. 2020, Payne et al. 2017) and can be adapted to the specific needs of this project. Its compatibility with through-shaft cabling was a key reason for its inclusion in this evaluation.

The 2D schematic of figure 3.1b demonstrates the preliminary nacelle layout, including sensor and motor placement. For option 1 to 4, the sensor will thus have to be placed right below the strut, which means the motor and gearbox will also have to move to the right in the drawing. This will then result in a longer nacelle. If option 5 is selected, the strut position is less constrained.

Dimensions

As discussed previously, the cable routing has a significant influence on the total spatial footprint. Shaft length is not considered critical at this stage, as it will be adapted during integration. Among the options, the TRS605 sensor (Option 4) from Futek has the smallest overall dimensions and thus offers the greatest flexibility in nacelle layout, not considering cable height. Shaft diameter, while noted for reference, is not expected to be a limiting factor in sensor selection.

Measurement accuracy

Accuracy is central to torque measurement reliability, though manufacturer specifications vary: some report as a percentage of rated output (RO), others of rated torque (RT) or full scale. Futek (Option 4) confirmed its values are based on the full 20 Nm range, consistent with RT-based definitions used by others, allowing fair comparison.

Based on the available data, the estimated ranking in terms of measurement accuracy, from highest to lowest accuracy is: Option 1 (Magtrol) and Option 5 (Appmeas DBBSS/TSF) with equal full-scale error, followed by Option 2 (Appmeas DRWPL-II), Option 4 (Futek TRS605), and finally Option 3 (Appmeas DRBK-II). The latter is 3-10 times less accurate than the others, but also significantly more affordable.

Environmental protection

Ingress Protection (IP) ratings define resistance to dust and water (International Electrotechnical Commission 2013). The shortlisted sensors range from IP40 to IP68:

- IP40: Protection against objects >1 mm; no water protection.
- IP44: Splash-resistant from any direction.
- IP67: Dust-tight; submersible to 1 m for up to 30 minutes.
- IP68: Fully dust-tight and submersible under prolonged immersion.

Option 5 clearly provides the highest protection (IP68). Even with a sealed nacelle, leakage cannot be ruled out, making IP68 sensors the most reliable, especially given the relatively high cost of a sensor compared to other components.

Operating temperature
The environmental temperature range of the sensors is generally suitable for laboratory and field testing. Options 1, 4, and 5 offer the broadest margins, though options 2 and 3 remain fully adequate.

Maximum rotational speed
Although the sensors have varying upper limits for rotational speed, ranging from 7000 to 15000 rpm, the turbine is expected to operate between 36 and 160 rpm. As such, all sensors are suitable in this regard and the motor will most likely be the limiting factor in this. Option 5, which rotates with the shaft, does not have a conventional maximum rpm limit. Similar configurations have been validated in prior work by Payne et al. (2017) for option 5, further confirming its suitability for low-speed applications.

Dynamic overload capacity
Dynamic overload refers to the maximum load above rated torque that the sensor can withstand without failure. Options 1, 4, and 5 tolerate $>$100% overload, offering safety under unsteady loading. Options 2 and 3 must remain below 40 Nm, which is within the expected range for this study. Option 1 has a low rated torque (10 Nm) with high overload capacity, but exceeding its rating may reduce accuracy. Since the turbine is designed for 12 Nm, a sensor with higher rated torque would be ideal, though Magtrol recommended this model for the current application.

Encoder
Options 1 and 4 integrate 360 pulses per revolution (ppr) rotary encoders, enabling high-resolution speed measurement. Options 2 and 3 require external encoders ($\approx$ €500, already included in table 3.1) with 60 ppr, equivalent to 6° resolution, sufficient for TSR control, but less suited to capturing high-frequency torque fluctuations. Option 5 requires a separate encoder or can derive speed from the motor.

Axial and radial load ratings
The axial and radial load limits determine the mechanical robustness of the sensor under thrust and shaft misalignment. Option 4 from Futek is most limited, allowing only 150 N of axial force. Since peak thrust can exceed 250 N at 1 m/s inflow, a thrust bearing will be required to prevent sensor overloading, which is a standard practice in turbine drivetrain design. Option 2 also requires a bearing under wave-influenced conditions. Option 5, by contrast, is rated for over 2500 N of axial load, which is also the measuring range of thrust for this sensor. Radial loads are not expected to be critical with proper shaft support and alignment.

Selection
Based on performance, integration feasibility, and durability, Option 5 (Appmeas DBBSS/TSF) is selected as the preferred torque sensor. While the Magtrol TS 107 (Option 1) provides the highest measurement accuracy and an integrated encoder, its diameter exceeds the nacelle limit and the lack of waterproofing (IP44) makes it unsuitable for submerged operation. The Appmeas DRWPL-II (Option 2) offers excellent accuracy and load capacity with IP67 protection, but only guarantees short-term submersion, limiting long-term reliability. The DRBK-II (Option 3) is attractive from a cost perspective but its accuracy and lack of sealing are insufficient. The Futek TRS605 (Option 4) is compact and includes an encoder, yet suffers from low axial load capacity, reduced accuracy, and poor environmental protection, resulting in an unfavorable performance-to-cost ratio.

Option 5 stands out by combining IP68 waterproofing, robust axial load capacity (2500 N), and the ability to measure both torque and thrust. Its internal cable routing simplifies sealing and supports integration of a slip ring. Although thrust measurement is not a requirement at this stage (see chapter 1.6.1), this sensor provides future flexibility without additional components for thrust measurements. Appmeas confirmed that the standard model can be customized for this application, including cable routing and waterproofing upgrades. Their previous experience with similar hydrokinetic turbine projects like Payne et al. (2017) further validates the sensor's suitability. Despite the higher price ($\approx$ €6,000 excluding encoder and slip ring), the reduced risk of failure and added functionality make Option 5 the most reliable long-term investment.

Figure 3.3: Appmeas sensor DBSS/TSF.

3.3. Motor selection

Selecting a suitable DC motor is more straightforward than choosing a torque sensor. The main constraint is the nacelle diameter: a DC motor is preferred due to its relatively small diameter for a given torque rating, as it typically operates at high rotational speed and low torque. The motor can then be paired with a gearbox to meet turbine requirements. Since the motor will primarily act as a braking element to regulate rotor speed and TSR, power generation is not essential. The final motor setup must therefore include a compatible controller, integrated or external, to manage the rotational speed.

After surveying the market, two manufacturers were identified with viable options: Crouzet and Maxon. Other brands (e.g. Bosch, Baldor) either lacked suitable models or only offered AC or brushed solutions exceeding nacelle constraints. Crouzet motors have been applied in hydrokinetic testing (Stallard et al. 2015), while Maxon solutions were used by Tian et al. (2018) and Lande-Sudall et al. (2023), and have also performed reliably in earlier TU Delft projects.

Two Crouzet models were considered. The 874-8036D002 (400 W, 24.4 Nm, 131 rpm) was dismissed due to its large diameter (230 mm) and overspecification. The DCmind brushless gearmotor (part number 80289718), by contrast, offers 21.5 Nm torque, 150 W continuous power, and a diameter of ~ 100 mm. With external controller availability through RS Components, this motor closely matches project requirements and is a strong candidate.

Maxon recommended two solutions. The IDX56M ENC 24V, with a 1:28 gearbox, provides 16.3 Nm continuous torque (34.5 Nm peak), 330 W, and a 120 mm diameter, while offering integrated control features. The EC90 Flat with GP90 gearbox provides higher ratings (29 Nm continuous, 60 Nm peak, 400 W) within a 100 mm diameter, though at higher cost.

Table 3.2 summarizes the approximate requirements based on the BEMT analysis (chapter 2) and compares the three shortlisted motor options. All three motors satisfy the basic torque and power

Table 3.2: Comparison of shortlisted DC motor options

Parameter	Required (approx.)	Crouzet (80 289 718)	Maxon IDX56M	Maxon EC90 flat + GP90
Max continuous torque (Nm)	12	8.4	16.3	29
Max peak torque (Nm)	18	21.5	34.5	60
Power rating (W)	$\geq$160	150	330	400
Required diameter (mm)	$\leq$130	100	120	100
Length (mm)	$\leq$250	204	203	120
Gear ratio	-	26.85	28	25
Nominal speed (rpm)	36-160	121	174	68
Max permissible speed rotor (rpm)	≥160	147	214	Not specified
Input voltage (VDC)	12-24	24	24	18
Control integrated	Preferred	No	Possible	Possible
Protection rating	≥IP65	IP65	IP65	IP54
Price ex. VAT, all included (€)	<2000	1357	1549 (−20%)	2196 (−20%)
Price ex. VAT, ex. controller (€)	<1600	1187	1109 (−20%)	1779 (−20%)

requirements. The Crouzet option provides suitable torque and diameter, but its maximum permissible speed (147 rpm) falls short of the expected 160 rpm after gearbox reduction. Although the Crouzet motor can be delivered quickly and is competitively priced, its performance limitations and lack of control integration reduce its overall suitability.

The Maxon EC90 Flat with GP90 gearbox offers the highest torque and power within a 100 mm diameter, but it is over-dimensioned for this application. Its lower protection class (IP54), long delivery time ($\approx$ 20 weeks), and higher cost further reduce the feasibility of this option.

The Maxon IDX56M emerges as the most balanced choice. With 16.3 Nm continuous torque (34.5 Nm peak), integrated control, and a maximum permissible speed of 8000 rpm at the motor (gearbox-limited to 6000 rpm at input, or 214 rpm at output), it comfortably meets the turbine's requirements while maintaining a safe margin. Although slightly larger in diameter than the Maxon EC90 (120 mm), it remains within design limits. Communication with Maxon confirmed cable routing challenges can be resolved with 90° connectors, and the gearbox (GPX52UP) offers 92% efficiency. Its delivery time ($\approx$ 9 weeks) and cost (€1,109 excluding VAT and a 20% educational discount) make it both technically and financially the most viable option.

Figure 3.4: Maxon motor IDX56M

In conclusion, the Maxon IDX56M was selected as the motor for this project due to its favorable balance of performance, integration potential, and availability. Together with the chosen torque sensor, the total cost of the drivetrain is approximately €7,100, though the exact sensor price will depend on final customization by Appmeas.

3.4. Cost constraints

During the development of this project, a significant and unexpected constraint emerged related to available funding. Originally, the plan was to complete the full drivetrain design, including all critical components (sensor, motor, and control system), and to manufacture a waterproof nacelle for experimental testing. However, due to recent government budget cuts to Dutch universities, the financial support available for MSc thesis projects at TU Delft was reduced. As a result, the project no longer received sufficient funding to purchase all planned components.

The motor (Maxon IDX56M) was already ordered before these funding constraints became clear, allowing this part of the system to be retained in the experimental design. With no budget available to purchase the torque/thrust sensor, the next phase of the project is also affected: while the design of the nacelle will still be carried out, there will be no budget to manufacture it during this project phase.

Nevertheless, this design work still remains valuable. By proceeding with the nacelle design, the project will generate a concept that can be used by future researchers, should additional funding become available. The design will still assume the use of the most advanced sensor considered (Option 5 - Appmeas DBBSS/TSF), since it was identified as the technically superior choice when cost is not a constraint. In this way, the sensor selection is aligned with the long-term goal of robust, high-fidelity measurement in submerged turbine environments.

In parallel, the rotor blades will still be 3D printed, and the mechanical connection to the hub will be constructed. This assembly is designed to fit onto the existing gondola structure at the TU Delft, which is currently used for propeller measurements. By adapting this infrastructure, it is still possible to conduct meaningful experiments to validate the BEMT predictions and run some wave cases.

The nacelle design will thus be carried out to the level of defining component layout, bearing configuration and overall dimensions, but not to full manufacturing detail, as this is no longer the main focus of the project.

3.5. Nacelle Design

The nacelle design is centered around the two primary components selected in the previous section: the motor and the torque/thrust sensor. The chosen motor requires a minimum nacelle diameter of 120 mm (see table 3.2). This value remains within the allowable range outlined in chapter 1.6.1, though it approaches the upper limit. Consequently, the design strategy is to treat the motor as the maximum defining diameter, meaning that all additional components such as bearings, sealing elements, and structural housing, must fit within or around this constraint.

Figure 3.5 shows a scaled representation of the motor and sensor with their supporting elements, including cable outlet, shaft couplings, bearings, and a slip ring. The slip ring (purple) transfers sensor signals from the rotating shaft to a stationary cable path. A suitable model is the Moflon MT1256-S12-HC2050, though the final choice will depend on channel count and configuration.

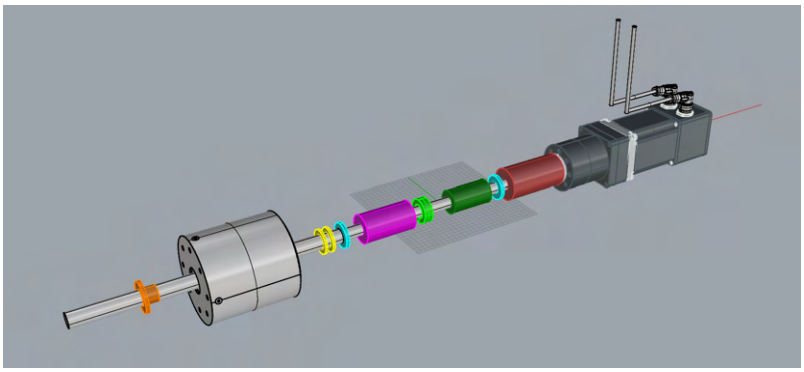

Figure 3.5: Setup of the motor, sensor and bearings.

The design is explained in three steps, starting of with the layout of the motor, sensor and all bearings that are needed. Then, to support this setup, the section called base support explains what connections are needed to the nacelle. The final part will explain the dimensioning of the outer tube and strut.

3.5.1. Axis configuration

A central consideration in the design process was modularity and ease of assembly. The nacelle is fully detachable, allowing components to be replaced or maintained without disassembling the entire system. This improves accessibility, facilitates bearing lubrication, and increases experimental flexibility.

Another critical factor is the low axial load capacity of the selected motor ($12\,$N). To protect it, axial forces from the rotor are absorbed by dedicated thrust bearings. The driveshaft is therefore divided into two sections: a motor-side shaft inserted from the rear, and a sensor-side shaft inserted from the front. These are joined internally by a coupling accessible from the top of the nacelle. The diameter of the shaft is flexible, but the axis of the force transducer of the gondola that will be used for testing is 10 mm in diameter, so this will be used as a reference.

Shaft support is provided by a combination of bearings and seals, color-coded in the design schematics (figure 3.5 and 3.7):

- Orange - plain bearing: A cost-effective option suitable for use in submerged environments. Provides radial support at low cost.

- Yellow - Radial shaft seal: Prevents water ingress along the rotating shaft, critical for protecting internal components like the motor. Two are added for extra safety.
- Light blue - Thrust bearing: Supports axial loads in both directions. Can be mounted against a shaft shoulder or a fixed collar on the shaft. The left bearing prevents movement to the right and the axial bearing on the right prevents movement to the left.
- Green - Radial bearing: Ensures lateral shaft stability. Only one radial bearing is included in this design, supported by the plain bearing and shaft alignment from the motor as well. It is expected that due to the stiffness of the shaft and the limited length, this will be sufficient.
- Dark green - Rigid shaft connection: Mechanically couples the two shaft sections to transmit torque directly.
- Red - Flexible shaft coupling: Accommodates minor misalignments and absorbs small axial or torsional deflections. While the use of both rigid and flexible couplings may seem redundant, it is necessary to isolate the axial bearing system between the two thrust bearings.

(a) Standard rigid shaft connection.

(b) Flexible coupling.

Figure 3.6: Examples of the 2 different shaft connections that are be used (RS Components Nederland 2025).

This bearing and shaft setup ensures that axial forces are absorbed where needed, while allowing the motor-side shaft to remain unloaded axially. The part to the right of the yellow radial shaft seals is to be watertight, as the components in this part are not resistant against water. The part with the sensor can be flooded without issues. The dark blue coupling element, which connects the two shaft sections, must be accessible from the top of the nacelle. This requirement defines the location of the strut, which must be positioned above the connection point to allow access during assembly.

The shafts join in the nacelle's central section, which also sets the minimum nacelle length. To avoid rotor inflow disturbance, at least 300 mm spacing is maintained between the rotor and the strut, corresponding to approximately one blade length.

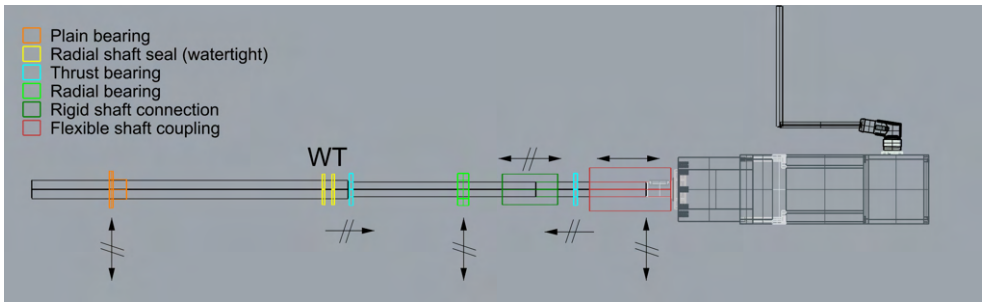

Figure 3.7: 2D drawing of the bearing configuration.

To clarify the bearing configuration in 2D, figure 3.7 is provided, showing which bearing constrains which movements. Above the axis, the two arrows provide information on the couplings, below the axis, the arrows provide information on the bearings. The yellow bearings do not have an arrow, as they are purely there for waterproofing.

3.5.2. Base support

The base support structure is described sequentially from front (left) to back (right), beginning at the rotor interface (figure 3.8). At the front end, a dedicated support is required to house the plain bearing (indicated in orange). This support will be integrated into a removable front cap, which is secured using four mounting holes visible on the flange of the circular attachment ring. This ring is rigidly connected to the outer nacelle tube.

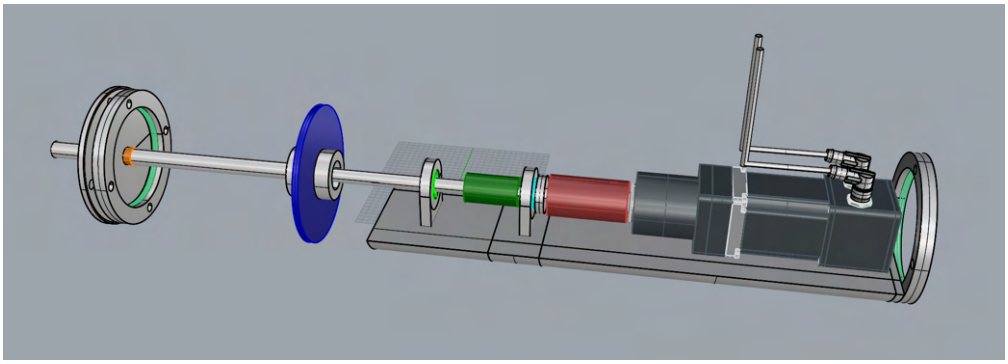

Figure 3.8: Support structure of the motor, sensor and other equipment within the nacelle.

Because the plain bearing is not watertight, the front section of the nacelle (left of the blue bulkhead) may flood during operation. This is acceptable, as all components in this region are water-tolerant. The blue watertight support houses two radial shaft seals (yellow), which form the primary barrier against ingress, and a forward thrust bearing (light blue) to absorb axial loads. A small water detection sensor with pump can be integrated here to remove any leakage, thereby protecting the rear nacelle section (requirement 2.5).

Further aft, an additional support structure is located at the bottom of the nacelle. This rear support section carries the radial bearing (green), the rear thrust bearing, and serves as the mounting point for the motor. The exact method for connecting the internal supports to the outer tube (e.g. bolted or threaded flanges, adhesive bonding, or snap-fit features) will depend on material and manufacturing choices.

These final details can be discussed with the company that is going to built the turbine housing. The current design was discussed with DEMO to explore the feasibility of manufacturing the nacelle. However, due to cost constraints, these discussions were discontinued. DEMO indicated that the estimated production cost would lie between €5,000 and €10,000, depending on material selection and manufacturing details. This includes also the housing that is discussed in the following section.

3.5.3. Nacelle Dimensions

In consultation with DEMO and technical staff at TU Delft, the outer nacelle geometry was developed based on internal component constraints and practical manufacturing considerations. As previously established, the inner diameter of the nacelle is $120\,\text{mm}$. To ensure sufficient mechanical strength and facilitate waterproofing, a wall thickness of $5\,\text{mm}$, as recommended by DEMO, was adopted. This results in an outer diameter of 130 mm. The limiting factor in further diameter reduction is the motor cable outlet. With alternative cable connectors or routing strategies, it may be possible to reduce the outer diameter to as low as 120 mm, but this is subject to further testing with the motor, which is already delivered to the TU Delft.

Given that the turbine will operate in submerged conditions, the nacelle must be manufactured from a corrosion resistant material. Standard stainless steel 316 has been selected due to its proven performance in marine environments and availability for fabrication.

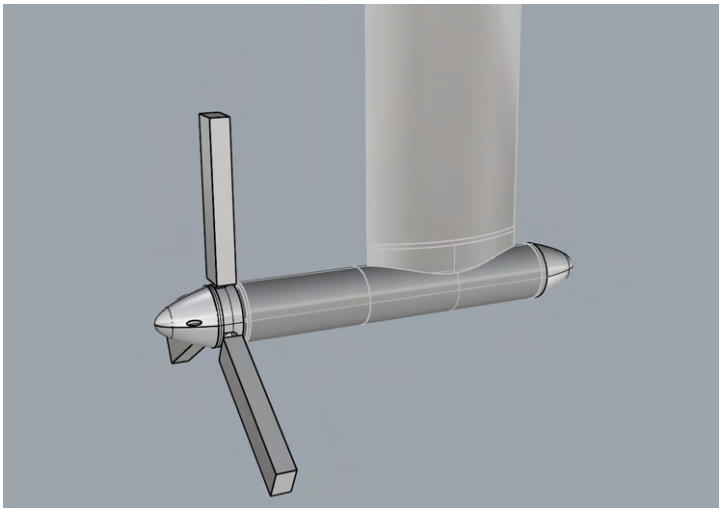

Figure 3.9: External view of the nacelle with simplified blade geometry.

The stainless-steel nacelle tube has a length of 700 mm (excluding end caps). Front and rear caps will be 3D printed and mounted to flat end plates, reducing costs and allowing hub design flexibility. The full assembly length, including the caps (figure 3.9), is approximately 950 mm.

The circular interface visible on the tube just in front of the strut indicates a mechanical connection point that allows the nacelle tube to be extended. By adding an additional central section, the design enables testing of wake strut interaction under varied rotor strut distances. The driveshaft must then also be extended accordingly, extending the shaft between the watertight support and the rigid shaft connection. The strut itself is also detachable to allow access to the internal rigid shaft coupling (see section 3.5.1) and also serves as the route for all electrical cabling.

On top of the stainless-steel caps, 3D-printed hubs can be mounted. This allows for a wide range of hub shapes to be tested while minimizing metal fabrication costs. The minimum diameter of 120 mm will be designed and used for the gondola setup (see chapter 5), but this can be scaled up to 130 mm by adjusting the outer 3D printed hub geometry without redesigning the base structure.

Strut height can be varied by adjusting the towing carriage position or replacing the strut with an alternative length. As an alternative to the current foil-shaped strut, a simpler cylindrical or rectangular profile could be used with a 3D-printed hydrodynamic fairing. This reduces fabrication cost and enables rapid iteration of strut designs, provided that the rigid shaft connector remains accessible. Since the centroid of the current foil-shaped strut is not located directly above the connector, a simplified profile may need to be shifted slightly forward.

3.5.4. Assembly order

The housing with its internal supports is fixed. The shaft with the sensor is then inserted from the front through the watertight support and radial bearing until it rests against the thrust bearing. After this, the front hub cap is attached, keeping the shaft in position while still allowing removal.

Next, the short intermediate shaft section is installed from the rear or top and connected to the rigid coupling, which is accessible from above. At this stage, the shaft is locked axially between the two thrust bearings. The first half of the flexible coupling is also mounted here.

From the rear, the motor with the second half of the flexible coupling is then connected, secured to the housing, and aligned with the coupling. Once the cables are routed, the rear hub cap and strut are mounted. The nacelle is then ready for operation, after which the hub with rotor can be attached. For disassembly, the steps can be taken in reverse order.

3.5.5. Preliminary structural simulation of the nacelle

To assess the structural integrity of the nacelle design (requirement 2.6), a preliminary strength analysis was carried out using SolidWorks Simulation. The primary goal of this study was to evaluate whether the proposed wall thickness of 5 mm would be sufficient to withstand the expected loads, and to quantify the resulting deformation under worst case loading scenarios. Although the final dimensions of the nacelle and strut may change, this simplified analysis provides valuable insight into load response and guides future design iterations.

A simplified nacelle and strut model (each 1 m long) was created in Rhino and imported into SolidWorks. This model does not reflect the full complexity of the turbine housing, but captures the overall geometry and structural layout necessary for initial strength verification. The strut was chosen as circular in this case, but it could change into square (with 3D print around) or foil shaped, like mentioned in 3.5.3. The main difference with the final model is that the loading from the current on the strut will be on the foil shape, whereas the strength must come from the rectangular or circular shape in case of the 3D print option.

SolidWorks Simulation uses the finite element method (FEM) to solve structural problems by discretizing the model into small elements and solving the governing equations for stress, displacement, and strain under applied loads and constraints (Dassault Systèmes 2025). For this study, two linked simulations were performed. First, a flow simulation to calculate the pressure distribution on the strut due to fluid motion. Second, a static simulation to apply both the hydrodynamic pressure and mechanical thrust load from the rotor. The thrust load was applied to the hub, representing the force that the rotor would exert on the nacelle.

The towing tank cross-section was represented as a rectangular flow domain with open inlet and outlet boundaries. A velocity of 1 m/s was prescribed at the inlet, and ambient pressure at the outlet. Flow was defined as external water flow with both laminar and turbulent modes enabled; default solver settings were retained. The resulting strut pressure distribution was exported and applied as a surface load in the subsequent structural analysis.

In the structural simulation, the nacelle was modeled as a shell body with a uniform wall thickness of 5 mm. The upper mounting interface of the strut was fixed, representing rigid attachment to the towing carriage. A load of 420 N was applied in the x-direction on the front hub surface, corresponding to the maximum expected rotor thrust (see table 2.4). The hydrodynamic pressure distribution from the flow simulation was applied across the entire strut surface. While in reality only the submerged section is loaded, this conservative assumption prevents underestimation of structural demands. Default mesh settings were used, resulting in computation times under one minute.

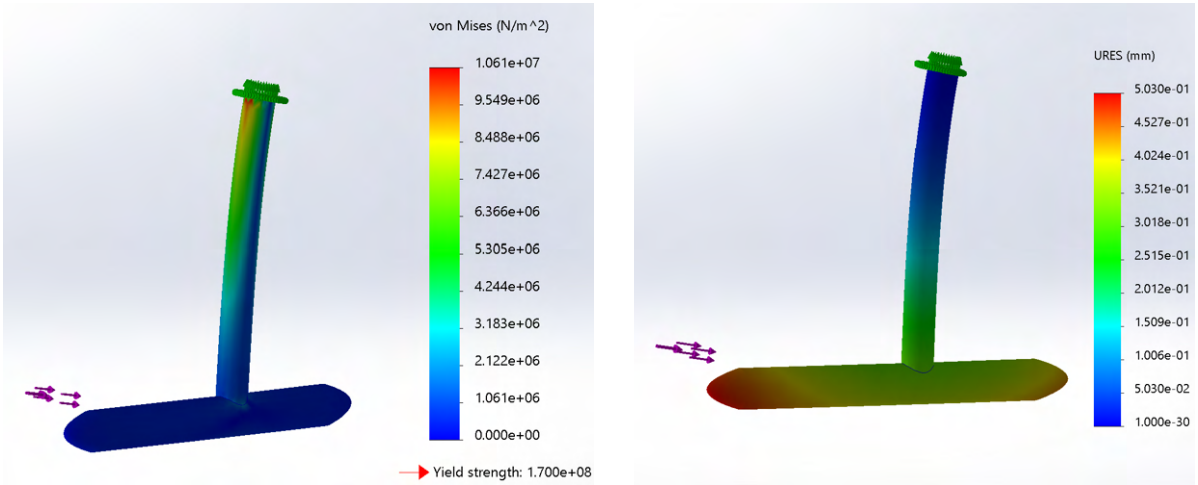

(a) Von Mises stress plot.

(b) Deflection plot.

Figure 3.10: Simulation results of the nacelle and strut under combined thrust and hydrodynamic loading.

The maximum von Mises stress, a commonly used criterion to assess material yield under complex loading (Budynas et al. 2015), was found at the fixed support region and reached a value of approximately 1.06×10^7 Pa, significantly below the yield strength of stainless steel 316 (1.7×10^8 Pa), resulting in a safety factor around 16. The maximum displacement occurred near the location of the applied rotor thrust and was found to be approximately 0.5 mm, which is considered acceptable given the 1 m nacelle and strut length. The plots of displacement and stress are shown in figure 3.10.

These results confirm that a 5 mm wall thickness is structurally sufficient under maximum loading conditions. SolidWorks provided an effective and efficient tool for this assessment: once the model and boundary conditions were defined, the simulations could be performed rapidly, enabling exploration of multiple scenarios within short computation times.

3.6. Conclusion

This chapter presented the conceptual design of the nacelle. While the full construction of the nacelle is currently beyond the project's budget, this design phase has established a technically feasible and structurally validated foundation for future development. The core components such as the sensor, motor, shaft layout, and structural supports, have been evaluated for their performance and integration potential, ensuring that the nacelle can be realistically constructed once additional funding becomes available. With the present design, requirements 3.1, 3.2, and 3.3 are satisfied, ensuring accurate torque and thrust measurement, precise rotational speed monitoring, and full-range speed control of the drivetrain.

The remainder of this thesis focuses on components that can be implemented within current constraints. The next chapter begins with the hub and blade design, forming the link between nacelle development and the experimental campaign. The hub will be constructed and mounted on the existing TU Delft gondola system, serving as a functional test platform. Once finalized, the hub geometry will also provide the basis for the blade design, which will proceed in parallel with manufacturing.

4

Hub and blade design

With the nacelle defined, the design of the rotor can now be addressed. The hub must provide a reliable connection to the nacelle while allowing for blade attachment and pitch adjustment. The blades require a balance between hydrodynamic efficiency, manufacturability, and structural stiffness under model-scale conditions. This chapter therefore answers the following research question:

Which blade and hub design choices best balance structural integrity and hydrodynamic efficiency, and what is their impact on turbine performance?

The following sections describe the hub requirements, blade design iterations, and performance predictions, followed by structural considerations and improvements leading to the final design.

4.1. Hub design requirements

The hub connects the blades to the shaft and sensor, transferring torque, thrust, and bending loads. It must fit the 10 mm H7 shaft with keyway of the TU Delft gondola (requirement 2.7) to ensure compatibility with existing infrastructure (requirement 2.6).

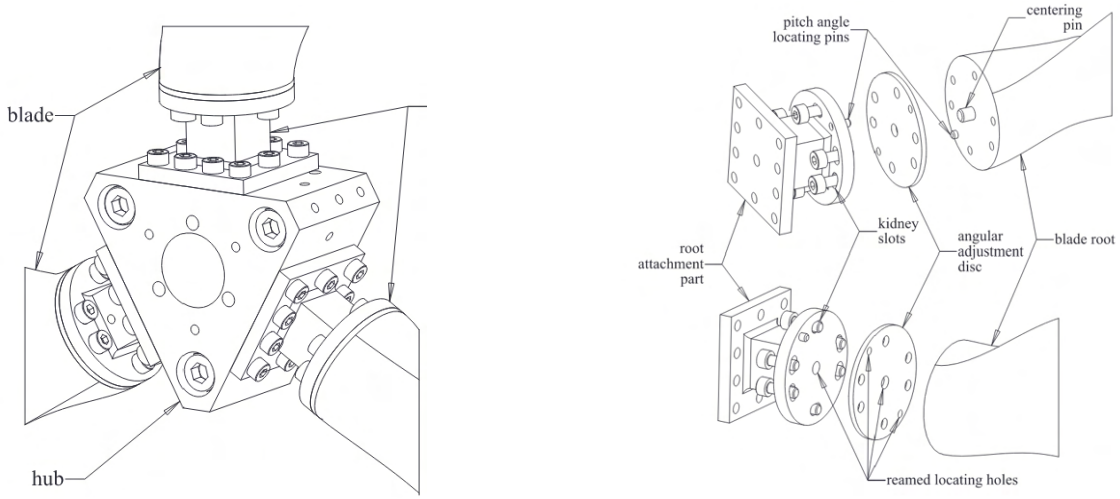

(a) Hub with blade connections.

(b) Blade connection and pitch adjustment system.

Figure 4.1: Hub design of Payne et al. (2017)

The design will build on the hub concept used by Payne et al. (2017) (figure 4.1), simplified for easier manufacturing. This design was mainly chosen because it meets all design requirements, with its pitch adjustment system and rigid design. It also has the possibility to add bending moment transducers within the blade connector in the future, as done by Payne et al. (2017). A circular root section will

be adopted for this design, to allow for easy pitch adjustments. The hub must also allow for quick assembly and disassembly, enabling fast blade changes and maintenance access (requirement 2.3). Each of the three blades should be mounted such that manual pitch adjustment is possible before installation, supporting flexible testing of different pitch angles (requirement 2.4). The use of corrosion resistant materials is essential, while non-load components may be 3D printed to reduce cost and allow for rapid design changes.

4.2. Connection between the blade and the hub

Before defining the hub dimensions, the blade-hub connection was designed. This required selecting the right connection for the flange (figure 4.1b), which also determined the circular blade root diameter. Four connection concepts in 3D printed material were tested experimentally (figure 4.2). Test piece 1 used a heated M5 insert, test piece 2 an epoxy-glued thread, and pieces 3 and 4 embedded M6 and M5 nuts, respectively. All connections had an effective height of 10 mm.

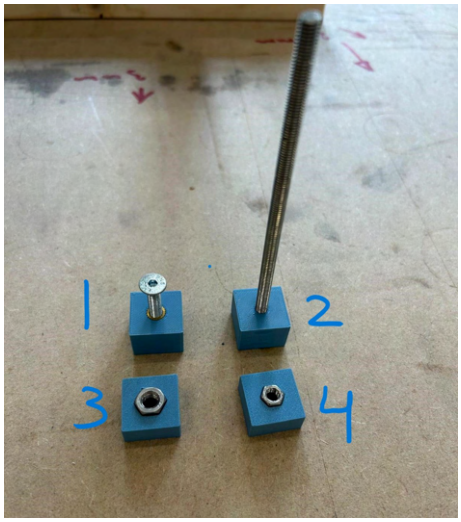

Figure 4.2: Testing pieces for 3D print connection. 1: heated M5 insert, 2: epoxy-glued thread, 3: M6 nut and 4: M5 nut

First, a static test was done, to see at what weight the connection fails and either the 3D print is destroyed or the weight is pulled out of the connection. The setup for this test is visible in figure 4.3.

(a) Epoxy connection, 4.5 kg.

(b) 30kg static test.

(c) Nut connection example.

Figure 4.3: Schematic layouts of the three drivetrain configurations considered for the experimental setup.

A maximum of 30 kg was possible in this setup, and at this maximum, 3 of the 4 options were still undamaged, see table 4.1. The epoxy connection failed at 26 kg, when the weight fell out of the connection, which makes this option less viable.

Connection type	Weight (kg)
1: Insert	>30
2: Epoxy	26
3: M6 nut	>30
4: M5 nut	>30

Table 4.1: Results of the connection pull-out tests.

The first test was inconclusive, as most of the designs remained undamaged under static loading. A second test simulated assembly torque. The nut-based designs failed quickly due to stress concentration across only a few printed layers (figure 4.4). The insert connection (option 1) performed significantly better. Although the insert began to rotate with the screw under torque, it remained embedded and was still able to support a 30 kg. A potential drawback is that if the insert starts rotating during disassembly, it may become difficult to remove the screw. However, this issue can be resolved by carefully heating the screw, allowing the surrounding material to soften again, enabling removal without damage. This recovery method was tested successfully.

(a) Top of damaged piece. **(b)** Bottom of damaged piece.

Figure 4.4: Damaged 3D printed piece with M6 nut.

Considering its balance of strength, ease of implementation and re-usability, the M5 insert connection (option 1) was selected for the final blade design. In contrast, the nut-based options would require integration during printing and complete blade replacement in case of damage or failure, which makes them less desirable.

4.3. Blade root diameter

After determining the connection method between the hub and the 3D print, the next important parameter to determine is the diameter of the circular blade root. This is a crucial input parameter for the flange connection. The determination of this diameter was done based on several input parameters, the first one being the M5 inserts. Payne et al. (2017) used 6 screws for this connection, this was found to be reasonable for this stage of the design as well.

Increasing the diameter of the root section will increase the strength, as it will be able to take up a larger moment. This will be mainly limited by the fact that the blade should still have a smooth transition from the circular section to the blade foils to ensure hydrodynamic smoothness. Several studies, for example Payne et al. (2017), Guo et al. (2018) and Bahaj et al. (2007) ensured that the first lift generating foil was located at $r/R = 0.2$, which will be the goal in this case as well. With a rotor radius of 0.37 m, this would be at 0.074 m from the center. The circular root diameter that other studies used is not of relevance, as the majority did not use 3D printed blades. Payne et al. (2017) used a circular root of 44 mm for its similar hub design. The only study that used 3D printed blades with a similar rotor diameter was Lande-Sudall et al. (2023), who had a blade root diameter of approximately 40 mm, following the design of Mycek et al. (2014).

With the range from earlier research determined, it was put into test using QBlade. Trying to maximize the diameter while still generating a smooth transition to a foil at approximately $r/R = 0.2$ leads to a diameter of 45 mm for the circular blade root. As can be seen in figure 4.6 the holes and the locating pin fit well within this space.

4.4. Hub design

With the blade root diameter defined, the remainder of the flange geometry was developed in consultation with workshop technicians to simplify manufacturing. Compared to the reference design (figure 4.1), several modifications were made to streamline the production process.

The flange was redesigned with fully circular components, removing the original square features that offered no structural benefit. Apart from the fact that it is easier the align (put the blade in the correct pitch orientation), there seems to be no major advantages in using square sections. The lower flange is secured with six bolts for now, sufficient given that the 3D printed blade root is the primary limitation. Calculations to validate this amount are provided in section 4.9. The central flange diameter was set to 25 mm to provide sufficient space for screw heads.

The new flange consists of three parts: two 5 mm thick plates and a 21 mm central cylinder, giving adequate screw engagement while minimizing hub size. Pitch plates are 3D printed, 3 mm thick, and used solely to set blade pitch (see figure 4.6).

The final adjustment that was done to the original flange design of Payne et al. (2017), is the removal of the original centering pin in favor of a 10 mm through hole for a carbon reinforcement rod. This rod will be glued into the blade root and extend into the flange, serving both as an alignment feature and as a structural element to relieve bending moments from the threaded insert connections. Given the 10 mm carbon rod at the root, this results in a wall thickness of 7.5 mm for the central flange section. The strength of the flange is validated in section 4.9.

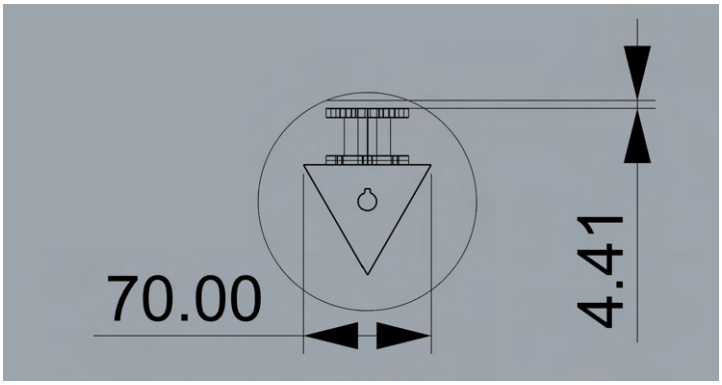

Figure 4.5: 2D hub design, with the 120mm ring representing hub diameter.

The triangular hub shape was also simplified for manufacturability. The final geometry has side lengths of 70 mm and an axial thickness of 50 mm, with six M5 threaded holes on each flange face. A maximum hub diameter of 120 mm was maintained, leaving 4.4 mm clearance for the hub cover (figure 4.5).

To evaluate the fits and functionality, the complete hub assembly was prototyped using 3D printing (figure 4.6). This revealed a potential issue with thread overlap in the triangular hub: for four of the six screw positions on each face, the M5 threads intersect with perpendicular threads after approximately 7 mm. Although this engagement length is considered sufficient for operational loads, care must be taken during manufacturing to avoid thread interference, and reach maximal usable thread. For the two vertical threads located directly above the axis, the thread depth was increased to 11 mm to ensure full engagement. Shrinkage of the print material also affected hole tolerances, which were increased to 5.4 mm to allow proper screw fitting.

Aside from this threading constraint and the shrinkage issue, the design looked feasible. After testing the strength with Solidworks, the working drawings can be produced.

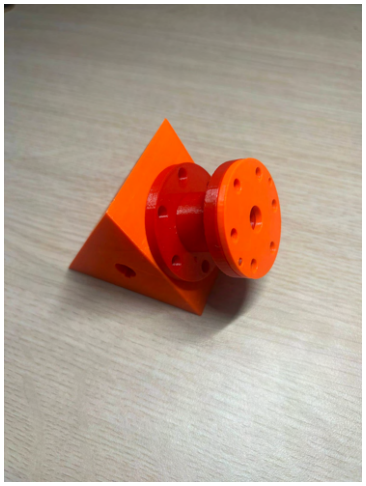

(a) 3D printed hub, with pitch plate attached.

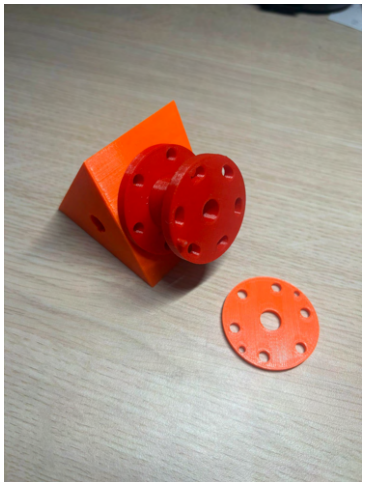

(b) 3D printed hub, with pitch plate unattached.

Figure 4.6: 3D printed design of the hub, with only one flange attached.

4.5. Pitching mechanism

To change the pitch angle of the blade, the blade must first be detached from the hub. Then, a new pitch plate, containing a different locating hole configuration, can be inserted. Only the position of the locating hole needs to vary between pitch plates as this shifts the orientation of the blade relative to the flange. As a result, the alignment of the screw holes changes slightly with each pitch setting. To accommodate this, the screw holes in the upper flange are designed as kidney-shaped slots (see figure 4.6b), allowing for angular adjustment of $\pm 5°$. This enables flexible testing under varying pitch angles without requiring structural modifications to the hub or blades.

4.6. Blade design

Several important blade dimension parameters are determined already. The turbine will have three blades and a diameter of 0.74 m. With a hub radius of 0.0542 m, the resulting blade length is 0.327 m. The circular root section has a diameter of 45 mm. This section now addresses the blade's chord, thickness, and twist distribution, starting with the selection of a foil. After designing the blade characteristics, the expected torque and thrust will be used to predict forces on the blade and the hub connection.

4.6.1. Blade profile

The design process starts with selecting a suitable blade profile. As discussed in section 1.3.4, thinner foils provide higher hydrodynamic efficiency, while thicker foils offer structural strength near the root (Muratoglu et al. 2015). The design therefore aims to use thin foils near the tip and thicker foils near the root, within the limits of 3D printing.

Based on the literature, three commonly used foil families were selected for comparison: NACA 63-8XX, NACA 63-418, and NREL S814 (see figure 1.10). The NACA 63-8XX series does not have a fixed thickness-to-chord ratio, offering flexibility to vary the thickness along the blade span. This foil also appears most frequently in previous studies, although the differences in popularity between the three profiles are relatively small. To evaluate foil performance, the integrated XFoil feature in QBlade was used to simulate lift-to-drag ratios, which serve as the most informative metric for foil efficiency. The simulations were performed with a Reynolds number of $1.2 \cdot 10^5$ (Guo et al. 2018). Although the final Reynolds number may differ, general performance trends remain valid.

Simulation results are shown in figure 4.7. For the NACA 63-8XX, thicknesses of 12%, 18%, and 24% were tested. The thinnest foil (NACA 63-812) produced the highest lift-to-drag ratio, while the NACA 63-818 showed a broader performance curve, advantageous for off-design conditions. The NACA 63-818 also outperformed the equally thick NACA 63-418, which exhibited a narrower operating range. Among 24% thickness foils, the NREL S814 slightly outperformed the NACA 63-824 in peak efficiency, but its

sharper peak limits robustness. Given that the thickness of the NACA 63-8XX foil can be adjusted spanwise, the NREL S814 does not offer a clear performance advantage.

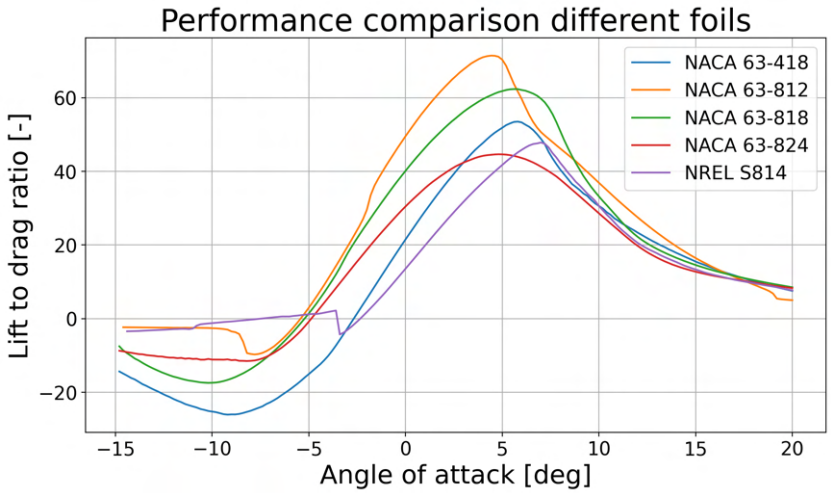

Figure 4.7: Lift-to-drag ratio as a function of the angle of attack, for the most used foils in hydrokientic turbine testing.

Based on this analysis, the NACA 63-8XX series was selected for the blade design. It combines superior lift-to-drag characteristics with the flexibility to vary thickness along the span, allowing a balance between efficiency near the tip and structural strength near the root. Thickness ratios between 12% and 24% can be applied depending on structural and manufacturing constraints. The 63-8XX belongs to the NACA 6-series, which dominates hydrokinetic turbine literature (see figure 1.10), appearing in 13 studies. Developed as second-generation foils by the National Advisory Committee for Aeronautics (NACA), the 6-series was designed to extend laminar flow and reduce drag due to separation (Abbott et al. 1959; Manwell et al. 2009). These foils exhibit relatively high maximum lift coefficients and are optimized for high-speed operation, though they show higher drag when operating outside their optimal range (Yadav et al. 2023).

The designation of a NACA 6-series foil follows a structured format, such as `NACA 63-818`, where each part provides specific information about its design characteristics:

- **6:** Indicates the 6-series.
- **3:** Defines the position of minimum pressure as a percentage of chord length (e.g., 30% in this example).
- **8:** Specifies the design lift coefficient in tenths (e.g., 0.8 in this case).
- **18:** Represents the maximum thickness as a percentage of the chord length (e.g., 18% in this example). XX at this location means that the percentage changes along the span of the blade.

With the blade profile chosen, the chord and thickness distribution along the blade can now be determined.

4.6.2. Chord length

The chord length strongly influences hydrodynamic performance. Two common approaches for determining chord length are the Betz and Schmitz methods, both derived from actuator disc theory and aimed at maximizing power extraction (Subramanya et al. 2020 and Gasch et al. 2012. The following formulas are based on Gasch et al. (2012).

The Betz method provides a simplified approach to chord length calculation, based on the concept of an ideal actuator disc and uniform loading along the blade span. The chord length, $\bar{c}_{\text{Betz}}$, is given as:

$$\bar{c}_{\text{Betz}} = c_{\text{Betz}} \cdot \frac{z \cdot C_L \cdot TSR_D}{R} = \frac{16 \cdot \pi}{9} \cdot \frac{1}{\sqrt{\left(TSR_D \cdot \frac{r}{R}\right)^2 + \frac{4}{9}}}$$

where z is the number of blades, C_L the lift coefficient, TSR_D the design tip-speed ratio, R the rotor radius, and r the radial position. The Betz method assumes a linear variation of axial induction along the blade span and neglects wake rotation effects. The chord length is a function of the local tip-speed ratio ($TSR_D \cdot \frac{r}{R}$), and decreases from the root to the tip of the blade.

The Schmitz method builds on the Betz method, but incorporates wake rotation effects, providing a more realistic representation of the flow around the blade. The chord length, $\bar{c}_{\text{Schmitz}}$, is given by:

$$\bar{c}_{\text{Schmitz}} = c_{\text{Schmitz}} \cdot \frac{z \cdot C_L \cdot TSR_D}{R} = \frac{16 \cdot \pi \cdot TSR_D \cdot r}{R} \cdot \sin^2 \cdot \left(\frac{1}{3} \cdot \phi_1\right)$$

where:

$$\phi_1 = \arctan \cdot \left(\frac{R}{TSR_D \cdot r}\right)$$

The inclusion of $\sin^2 \cdot \left(\frac{1}{3} \cdot \phi_1\right)$ accounts for the variation in the angle of relative velocity along the blade. This method adapts the chord length to ensure optimal lift generation, particularly in regions where wake rotation has a significant influence.

Comparison of the Methods

The two methods differ most at low local tip-speed ratios as can be seen in figure 4.8. This is the region near the root of the blade. For higher tip-speed ratios not much difference is noticeable.

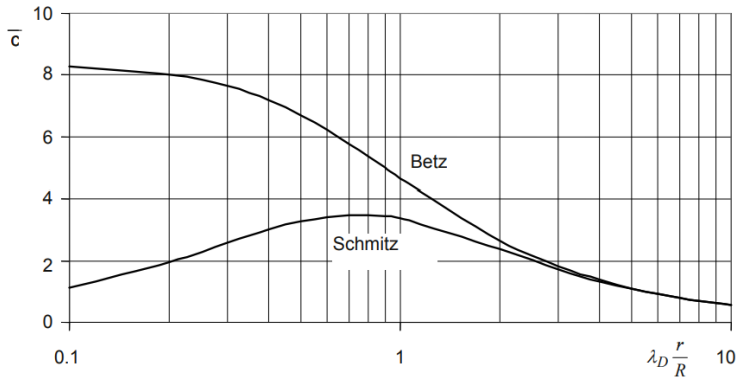

Figure 4.8: Difference between optimal chord distribution according to Schmitz and Betz method for different tip-speed ratios (Gasch et al. (2012)).

The chord length distributions derived from the Betz and Schmitz methods show that chord length is primarily a function of the blade's radial position, the number of blades, the design tip-speed ratio, and the lift coefficient. As shown in Batu et al. (2020) this is true for the different chord distribution calculation methods. Some methods also include the drag, which increases with higher chord length due to a larger wetted length. Based on the available formulations in QBlade and the nature of the expected flow conditions, the Schmitz method was selected to define the initial chord distribution. This method improves on Betz by accounting for wake rotation effects, which are particularly relevant at lower local tip-speed ratios, occurring near the root.

Linear taper

QBlade also offers a linear chord taper. Although the linear taper is simple to implement and often used due to its ease of manufacturing, it is not hydrodynamically optimal. As discussed by Gasch et al. (2012), it provides a reasonable compromise between performance and simplicity, but it especially oversimplifies the chord near the root section. Burton et al. (2011) explain that a uniform taper removes material near the root and reduces design complexity, but deviates from the optimal BEMT-based distribution, which is visible in figure 4.8. Since this blade will be 3D printed, manufacturing constraints are minimal. A strong root is structurally required, and the Schmitz distribution provides a more realistic, performance-oriented design. For these reasons, the Schmitz method was selected over the linear taper.

4.6.3. Thickness

The thickness at the root was predetermined to be 100% of the chord length by selecting a circular root section. To maximize efficiency, the objective is to transition to a lift-generating foil as early as possible along the blade span. Based on literature findings (figure 1.15), blade thickness typically decreases from approximately 22% at the root to around 12% near the tip.

For this design, the NACA 63-824 foil was selected as the first lift-generating section, aiming to be positioned at approximately $r/R = 0.2$ (see section 4.3). From this point onward, the blade thickness is gradually reduced, reaching a minimum of 12% at the blade tip. This initial distribution prioritizes hydrodynamic performance. If subsequent structural analysis indicates insufficient blade strength, the thickness distribution can be adjusted accordingly afterwards.

OpenVSP (v3.24.0), originally developed by NASA for aircraft design (NASA OpenVSP 2024), was used to generate NACA 6-series profiles with thicknesses of 12%, 15%, 18%, 21%, and 24%. The software exports high-resolution point data for use in QBlade, where intermediate foils can be generated with the built-in interpolation function (see section 2.6.4). Figure 4.9 illustrates the three thickness variations considered.

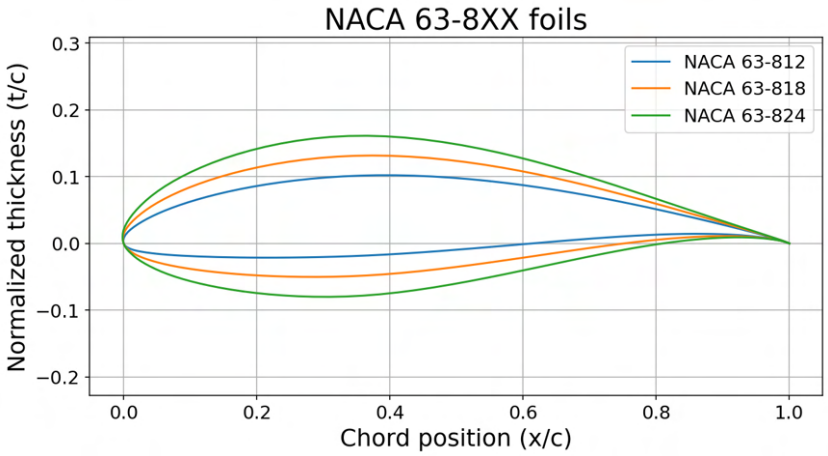

Figure 4.9: NACA 63-8XX plotted with different thicknesses.

4.6.4. Twist

The twist angle of a turbine blade is the final critical design parameter that ensures each section of the blade is aligned with the local relative flow direction, thereby maximizing hydrodynamic efficiency. In QBlade, the twist distribution can be optimized using either the Betz or the Schmitz approach.

The key difference is the treatment of wake rotation again. Betz neglects it, giving a simplified velocity triangle and generally higher twist near the hub at low tip-speed ratios (figure 4.10). Schmitz includes wake rotation, producing a more realistic velocity distribution and lower twist angles close to the root, similar to its improvement over Betz in chord distribution (section 4.6.2).

Like explained in Gasch et al. (2012), the twist angle $\beta(r)$ at a given radial position is computed as:

$$\beta(r) = \phi(r) - \alpha \tag{4.1}$$

where $\phi(r)$ is the angle of the relative velocity and α is the angle of attack at the optimal lift-to-drag ratio for the chosen foil, for Betz:

$$\phi_{\text{Betz}}(r) = \arctan\left(\frac{2}{3} \cdot \frac{R}{TSR_D \cdot r}\right) \tag{4.2}$$

and for the Schmitz method:

$$\phi_{\text{Schmitz}}(r) = \frac{2}{3} \cdot \arctan\left(\frac{R}{TSR_D \cdot r}\right) \tag{4.3}$$

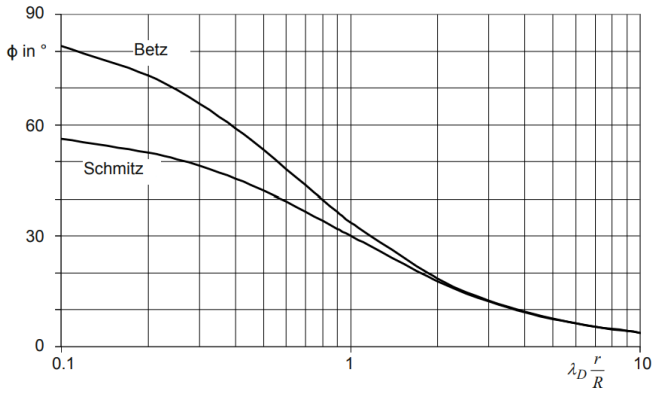

Figure 4.10: Difference between optimal twist distribution according to Schmitz and Betz method for different tip-speed ratios (Gasch et al. (2012)).

As discussed by Gasch et al. (2012) and visualized in Burton et al. (2011), the Schmitz distribution better accounts for the hydrodynamics near the blade root.

Besides Betz and Schmitz, QBlade offers linear and stall-based twist optimizations, but these are less suited for performance-oriented design. Instead, the optimal lift-to-drag ratio (C_L/C_D) approach is selected, which adjusts the angle of attack locally to achieve maximum efficiency. Practically, this means α in equation 4.1 is equal to the optimal angle of attack for the design TSR.

4.6.5. First design iteration

With the theoretical groundwork now complete, the attention shifts to the practical side of the project, namely the blade design. This first design iteration is developed using the input parameters summarized in table 1.5. This prototype will be 3D printed to assess structural integrity and printing resolution.

At this stage, two key parameters must be defined to shape the blade: the inflow velocity and the design TSR. The tip-speed ratio directly influences the chord and twist distribution along the blade, while the inflow velocity is needed to estimate the Reynolds number, which in turn governs foil selection.

Reynolds Number Estimation Strategy

The representative Reynolds number is calculated at $r/R = 0.75$, a commonly accepted reference location in literature for capturing the dominant hydrodynamic behavior of the blade. This method follows the approach of El-Shahat (2020), who showed that for horizontal-axis tidal turbines, the flow conditions at 75% span provide a good balance between accuracy and simplicity. This region typically contributes most to the overall torque and power, and the local flow angle remains relatively stable, making it a logical choice for evaluating lift and drag characteristics.

The Reynolds number is calculated using the following relation:

$$Re = \frac{U_{\text{rel}} \cdot c}{\nu} \tag{4.4}$$

where c is the chord length at $r/R = 0.75$ and ν is the kinematic viscosity of water, taken as $1 \cdot 10^{-6}$ m/s. U_{rel} is the local relative velocity, which depends on the rotational speed and inflow velocity (see equation 1.13).

However, in this early stage of the design, the chord length is not yet known. Instead, a rough estimate is used to proceed. A target inflow velocity of $0.75\,\mathrm{m/s}$ is chosen, as it is the middle value of the desired operating range. This choice allows the design to perform well under typical flow conditions, rather than being optimized for only extreme ends.

Assuming a rotor radius of 0.37 m, a TSR of 5, and an estimated chord length of 0.04 m at $r/R = 0.75$, the corresponding Reynolds number is approximately $1.2 \cdot 10^5$. This value is used for generating the initial polar data in the first design loop. QBlade will then interpolate the Reynolds number for different locations along the blade span and for different operating conditions.

Polar extrapolation

Once the foil shapes have been imported into QBlade (as described in section 4.6.3), the next step is to assign the polar definitions, illustrated in figure 2.7. For consistency with earlier validation work (see section 2.6), the critical amplification factor N_{crit} is set to 1 and compressibility effects are ignored by setting the Mach number to 0. Together with the specified Reynolds number, these values serve as input for QBlade's XFOIL-based analysis, which combines a panel method for the inviscid flow with a boundary-layer solver and transition model to compute lift and drag coefficients across a range of angles of attack. In addition, QBlade can generate visualizations of velocity and pressure distributions, though these are not used further in this study. The lift and drag curves, however, form the essential basis for the subsequent blade design.

QBlade requires complete $360°$ polar data to run its BEMT simulations (Marten et al. 2024). Even though the actual turbine is intended to operate around its optimal angle of attack, extrapolated polars ensure that QBlade can simulate performance under off-design conditions.

Two extrapolation models are available in QBlade for generating these extended curves: the Montgomerie method (Montgomerie 2004) and the Viterna method (Viterna et al. 1982). Both methods extend polar data beyond the angle range provided in the original foil simulations, but follow different strategies and assumptions.

The Montgomerie method approximates the foil as a flat plate at high angles of attack. It uses several curve-fitting parameters to ensure smooth continuity:

- $A+/B+$ and $A-/B-$: Define the curvature of the extrapolated sections for positive and negative angles.
- Slope: Sets the slope of the curve to match the existing polar data.
- CD90: Specifies the drag coefficient at $90°$, which has a notable effect on the overall curve shape.

The Viterna method, on the other hand, is based on empirical data and provides a robust model for post-stall behavior with fewer parameters to tune:

- Range of original polar: Defines the angle range from the original data used for interpolation.
- CD90: Sets the drag coefficient at $90°$, typically approximated as 1.3 for a flat plate (NASA Glenn Research Center 2023).
- St+ / St-: Represent the positive and negative stall angles.

In this project, the Viterna method is selected for its ease of use and consistent initial results. As the focus is not on off-design behavior or dynamic stall, extensive tuning is not necessary. The default polar range $(-15°, 20°)$ is kept, and CD90 is adjusted to match the flat plate value of 1.3. Stall angles are left at the standard $\pm 20°$, which, while possibly not accurate for the NACA 63-8XX foils at low Reynolds numbers in water, are considered acceptable for this steady-state analysis.

With these settings, QBlade generates extended lift, drag, and moment coefficient curves as shown in figure 4.11. These polars form the input for all performance calculations in subsequent steps.

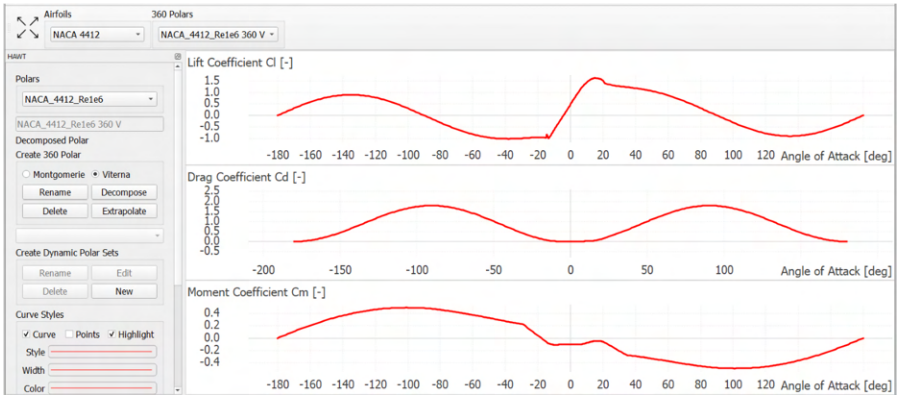

Figure 4.11: Example of foil extrapolation using the Viterna method in QBlade (Marten et al. 2024).

Blade root section

With the Reynolds number estimated and foil properties defined, the full blade geometry can now be constructed. A total of 25 spanwise stations was selected to define the blade shape. This number offers sufficient resolution for accurate interpolation and local refinement, while still being manageable within QBlade. With a blade length of approximately 0.315 m, this corresponds to an average spacing of 12.5 mm. In the root region, spacing was manually refined to ensure a smoother transition between the circular root and the foil shapes, which is an important factor for both structural continuity and printability.

To establish this transition, a 64% thick interpolated foil was introduced between the NACA 63-828 and the fully circular root section. This thick foil was not intended for hydrodynamic performance, but rather to bridge the geometry structurally. The very first two stations at the root used a circular profile, intended to house the inserts and provide sufficient volume for the inserts.

Chord lengths were initially defined using the Schmitz method (section 4.6.2) at a TSR of 5, and then slightly adjusted to maintain geometric continuity. This configuration successfully combined structural robustness with hydrodynamic performance: the first lifting section appears at $r/R \approx 0.22$, closely matching the $r/R = 0.2$ design target (section 4.3). Minimal changes to the root were needed in later design iterations.

Mid and tip section

The portion of the blade spanning from $r/R = 0.22$ to the tip is referred to as the mid and tip section. The aim in this region was to implement increasingly thinner, high-efficiency foils, with the NACA 63-812 at the tip, which exhibits the most favorable lift-to-drag performance at the design Reynolds number (see figure 4.7). Given that the precise mechanical properties of the printed material were not yet known at this stage, foil selection and thicknesses were based on earlier studies, particularly the work by Guo et al. (2018), and guided by the goal of achieving a smooth geometric transition.

With the foil layout defined, QBlade was used to optimize chord and twist distributions (sections 4.6.2 and 4.6.4). Several intermediate foils were interpolated within QBlade to ensure smooth thickness variation between the defined profiles. For practical integration of the carbon rod, all profiles were aligned along their maximum thickness in QBlade's advanced blade design tool, which does not affect hydrodynamic performance.

The resulting blade geometry is provided in Appendix D. The resulting geometry features a chord tapering from about 0.076 m at the root to 0.025 m at the tip, while the twist decreases smoothly from $\approx 25^\circ$ near the root to $\approx 3^\circ$ at the tip, excluding the circular root region. Thickness reduces gradually from 28% at $r/R = 0.22$ to 12% at the tip, with several interpolated foils ensuring smooth transitions. The first station is located at 0.054 m from the rotor center, corresponding to the top of the pitch plate.

Carbon rod integration

To improve bending stiffness and structural reliability, a tapered carbon rod was embedded in the blade, a common practice for 3D-printed model turbines at TU Delft. The taper maximizes rod diameter within the available blade thickness.

After exporting the geometry from QBlade to Rhino, a cylindrical cut-out was added. Its diameter was set 1 mm larger than the rod to allow clearance for insertion and to accommodate the epoxy adhesive, ensuring a continuous bond between the rod and the blade shell. Apart from the insert slots, this was the only post-processing modification before 3D printing.

3D Printing trial

To assess the structural integrity of the blade and its conformity to the design specifications, the geometry was fabricated using 3D printing. This initial prototype served to assess structural strength, printing accuracy, and overall surface quality. The result, shown in figure 4.12, revealed several shortcomings. While valuable insights were gained, the blade ultimately failed due to insufficient strength.

The primary issue encountered was the brittleness of the thin tip section. Also, the trailing edge was too sharp for the printer to replicate it, falling below the printer's minimum resolution of 0.4 mm per layer. As a result, the printer could not generate a continuous edge.

Figure 4.12: First 3D printed blade trial, broken at four different locations.

The blade was printed upright with 20% infill. While this gave good surface definition, the orientation aligned the weakest print axis with the bending loads, causing easy fracture along the chord.

Despite these failures, the trial confirmed a smooth root finish and sufficient geometric resolution (70 chordwise and 200 spanwise points). Although not structurally successful, the print provided useful feedback on material limits, print orientation, and tolerances, guiding the second design trial.

4.6.6. Second design iteration

Following the shortcomings observed during the first 3D printed trial, a second blade design was developed with several major modifications aimed at improving structural integrity and printability.

Key adjustments to the design

A significant change was made to the design TSR, which was reduced from 5 to 4. As discussed in section 4.6.2, this modification results in increased chord lengths and twist angles, and a lower rotational speed for a given inflow velocity. These modifications will provide a thicker and stronger blade profile. While the power output remains unchanged, the lower TSR increases torque (equation 2.6). For a chord of 0.041 m, $Re \approx 97{,}200$, which was used to generate updated polars in QBlade.

Since the tip region failed in the first print, the thinnest foil was replaced by the NACA 63-818 (18% thickness). Although thinner foils achieve slightly higher lift-to-drag ratios (figure 4.7), the 63-818 provided sufficient strength with acceptable efficiency. To further improve printability, trailing edges were thickened using QBlade's gap-setting feature, ensuring a minimum thickness of 0.8 mm (≈2 print layers). The shape change was minimal, as shown in figure 4.13 for the thinnest foil used.

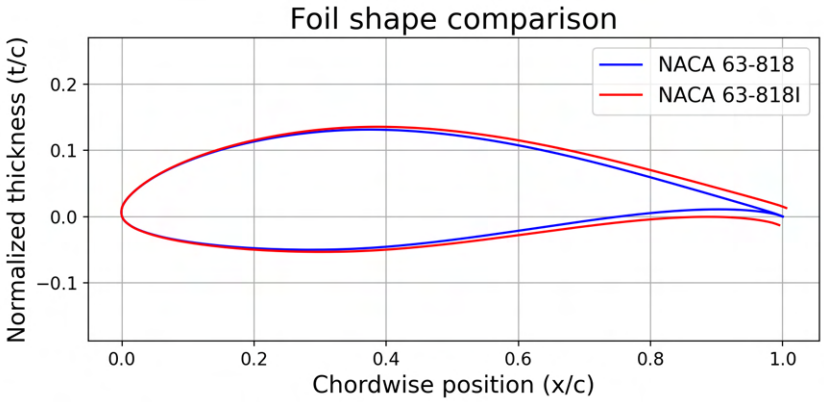

Figure 4.13: Comparison between original NACA 63-818 and modified version with 2.8% trailing edge gap.

These adaptations lowered the estimated efficiency from $C_p \approx 0.42$ to 0.39, but significantly improved structural feasibility.

Additional modifications

Several minor improvements were also introduced to address issues identified in the first prototype:

- The circular root section was extended by 1.2 mm in radial direction (3 print layers) to prevent the insert to stick through the blade.
- Chord lengths near the root were kept largely unchanged for smoothness, despite the TSR adjustment.
- To avoid visible indentations from the carbon rod holes, a minimum wall thickness of 1.2 mm was maintained around the rod cutouts.
- Hole clearances were reduced from 1.0 mm to 0.6 mm (0.4 mm for the 10 mm rod), improving the accuracy of placement in the blade.
- The printer infill percentage was increased from 20% to 50% for greater stiffness.

Geometry verification

To validate the smoothness of the updated blade design, the chord, thickness, and twist values were plotted along the blade span. A second-order polynomial was fitted to the chord distribution, and a third-order polynomial to the twist, as shown in figure 4.14. The fits confirmed that smooth transitions were achieved between the different blade sections. Only the root region, which was not re-optimized for a TSR of 4 in terms of chord length, required relatively large manual adjustments.

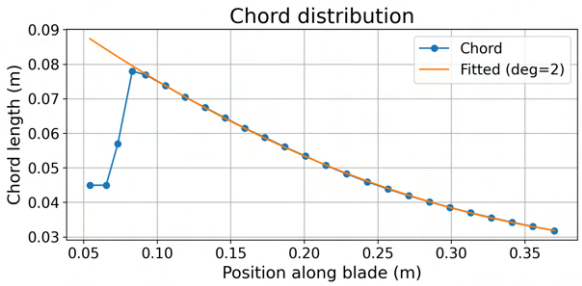

(a) Chord distribution with second-order polynomial fit.

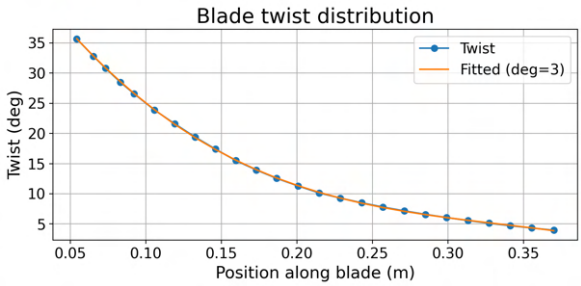

(b) Twist distribution with third-order polynomial fit.

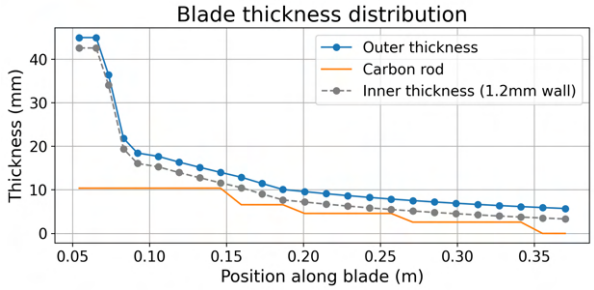

(c) Thickness distribution with carbon rod allowance.

Figure 4.14: Blade geometry characteristics plotted along span.

Figure 4.14c specifically shows the inner wall thickness after subtracting 1.2 mm from the outer surface. This constraint limited the maximum rod diameter at certain points but still allowed a 4 mm carbon rod up to approximately $r/R = 0.7$, and a 2 mm rod nearly to the tip.

Final geometry

The complete blade geometry, including spanwise positions, chord lengths, twist angles, and foil selections, is summarized in table 4.2. No changes were made to the blade definition after this point as the 3D print turned out smoothly and well defined.

4.6.7. Performance predictions

With the final blade design established, and a satisfactory 3D print, performance predictions for the turbine can be made with QBlade. Figure 4.15 shows the different parameters that were used during

Table 4.2: Final blade geometry definition

Pos [m]	Chord [m]	Twist [deg]	Foil
0.054	0.045	35.650	Circular_Foil
0.065	0.045	32.800	Circular_Foil
0.073	0.055	30.800	Interpolated 64
0.083	0.078	28.500	NACA63828I
0.092	0.077	26.600	NACA 63824I
0.106	0.074	23.900	NACA 63824I
0.119	0.070	21.600	Interpolated 23.25I
0.133	0.068	19.400	Interpolated 22.5I
0.146	0.065	17.400	Interpolated 21.75I
0.160	0.061	15.500	NACA 63821I
0.173	0.059	13.950	Interpolated 19.5I
0.187	0.056	12.550	NACA 63818I
0.201	0.053	11.300	NACA 63818I
0.215	0.051	10.140	NACA 63818I
0.229	0.048	9.278	NACA 63818I
0.243	0.046	8.503	NACA 63818I
0.257	0.044	7.803	NACA 63818I
0.271	0.042	7.167	NACA 63818I
0.285	0.040	6.588	NACA 63818I
0.299	0.039	6.058	NACA 63818I
0.313	0.037	5.572	NACA 63818I
0.327	0.036	5.124	NACA 63818I
0.341	0.034	4.711	NACA 63818I
0.355	0.033	4.328	NACA 63818I
0.370	0.032	3.957	NACA 63818I

the simulations. The fluid density is 1000 kg/m^3 for water and it has a kinematic viscosity of $1 \cdot 10^{-6}$ m^2/s. The inflow velocity is set to 0.5 m/s in this case as an example. The collective pitch is kept at $0°$, which means the twist angles along the blade define the effective pitch angle.

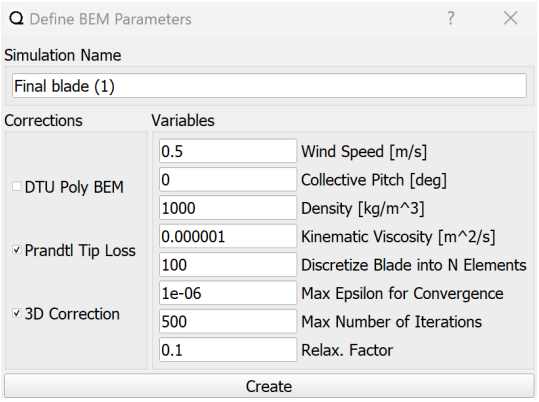

Figure 4.15: BEMT definition parameters.

The blade was divided into 100 elements, sufficient for accuracy without excessive computational cost. Default QBlade solver parameters (tolerance $1 \cdot 10^{-6}$, 500 iterations, relaxation factor 0.1) gave stable results and were not modified. The selected corrections are described separately in section 2.6.5.

First, looking at the efficiency for the current turbine design, the design goal was set at a minimal C_p of 0.35 (requirement 1.2). Figure 4.16a shows that this is achievable, despite the fact that some performance had to be removed for structural considerations (see section 4.6.6). The graph shows a rapid growth up until the maximum C_p of 0.391, after which the decline is more flat. It goes down to a

value of 0.257 for a TSR of 7. The maximum C_p predicted by QBlade happens at a TSR of 4, which is expected as this is what it was optimized for. Requirement 1.1 is thereby also reached.

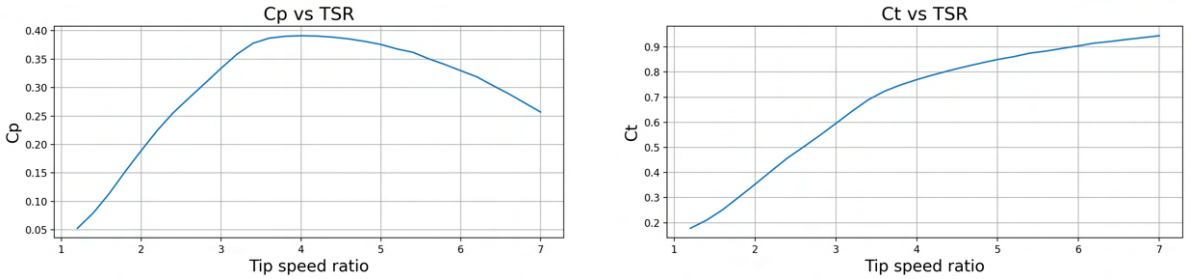

(a) C_p curve for the final blade design.

(b) C_t curve for the final blade design.

Figure 4.16: C_p and C_t curves for the final blade design.

For thrust, requirement 1.3 specified $C_t \geq 0.7$ at optimal TSR. This is also theoretically reached as can be seen in figure 4.16b. The value for a TSR of 4 is 0.77, which is only 10% above the desired value. Experimental validation in chapter 5 will show whether or not the minimum is reached in practice. Ct increases up until 0.945 for a TSR of 7.

Torque and thrust predictions for inflow velocities of 0.5-1.0 m/s are shown in figure 4.17. The maximum thrust expected for 1 m/s at a TSR of 7 is 203 N. The maximum torque of 8.93 N/m happens at a TSR of 3.2 according to the BEMT predictions. For lower inflow velocities the TSR at which maximum torque happens remains the same. These maximum values for steady flow will be used to predict forces that will act on the blades in sections 4.8 and 4.9.

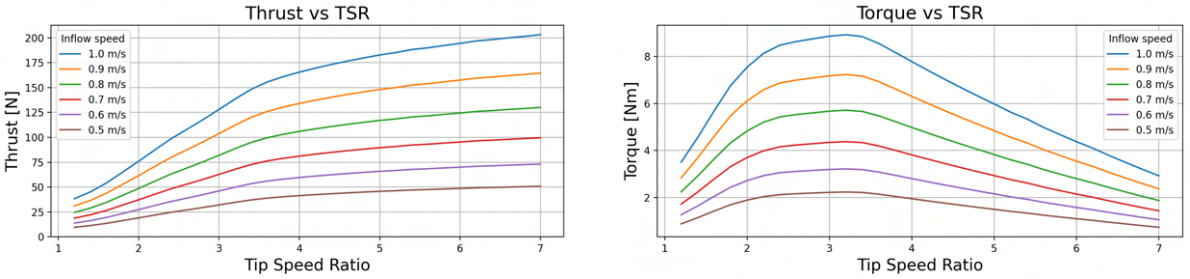

(a) Thrust vs TSR.

(b) Torque vs TSR.

Figure 4.17: Thrust and torque performance of the final blade design for different inflow velocities.

The final plots extracted are the normal and tangential force distributions along the blade span (figure 4.18), which are used to determine equivalent loading positions for experimental testing (chapter 4.8). Integrating the normal force using the trapezoidal rule gives one third of the total thrust, as expected since the values are per blade and thrust is evenly distributed under uniform inflow. Dividing the moment by the force gives the equivalent loading location, which for TSR = 4 was 0.197 m (68% span) for thrust and 0.164 m (59% span) for torque, measured from the blade root. For other TSRs, the differences of equivalent loading are minor so these values will be used in section 4.8. The shorter torque arm compared to thrust is consistent with the force distributions, and the thrust location aligns well with the common 2/3-span analytical approximation (Manwell et al. 2009). Tip-loss effects are visible, with forces approaching but not reaching zero at the tip, unlike in actuator disc theory (figure 2.6).

The theoretical values for torque and thrust will be validated in chapter 5 to ensure the structural rigidity of the blade, and the predictive capabilities of the BEMT method.

4.7. Wave conditions

The steady inflow analysis does not capture wave effects. Since QBlade cannot model unsteady or wave-induced inflow, an analytical wave model is used to estimate the maximum horizontal velocity at

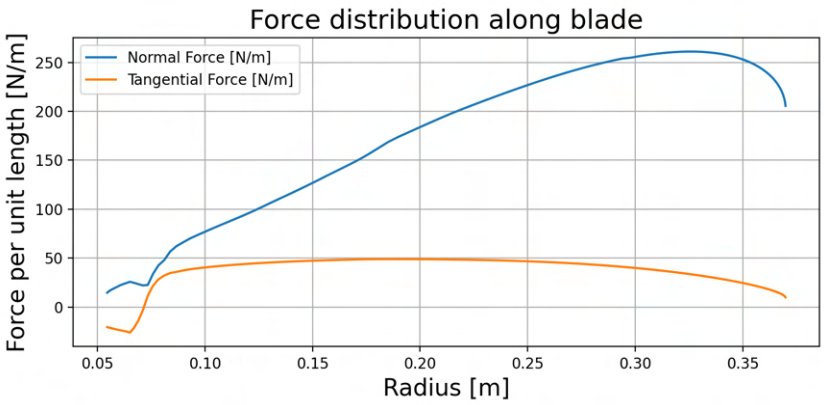

Figure 4.18: Distribution of forces along the blade radius.

different depths. Following linear wave theory in two dimensions (x-z) (Dean et al. 1991; Munson et al. 2012), this derivation provides the horizontal velocity induced by a propagating wave at depth, which can then be applied as a constant input in QBlade to approximate critical wave loading with steady-state tools.

4.7.1. Derivation wave-induced velocity from potential flow theory

The flow is assumed incompressible, inviscid, and irrotational. Starting from the incompressible Navier-Stokes equations:

$$\frac{\partial \boldsymbol{u}}{\partial t} + (\boldsymbol{u} \cdot \nabla)\boldsymbol{u} = -\frac{1}{\rho}\nabla p + \nu \nabla^2 \boldsymbol{u} + \boldsymbol{g}, \tag{4.5}$$

with the continuity equation for incompressible flow:

$$\nabla \cdot \boldsymbol{u} = 0, \tag{4.6}$$

For wave analysis, the convective term $(\vec{u} \cdot \nabla)\vec{u}$ is neglected (linearization), and the viscous term is dropped ($\nu \nabla^2 \vec{u}$). Under irrotational flow ($\nabla \times \vec{u} = 0$), the velocity field can be written as the gradient of a potential, $\vec{u} = \nabla \phi_p$. Substituting this into the continuity equation yields Laplace's equation:

$$\nabla^2 \phi_p = 0 \tag{4.7}$$

which governs the velocity potential in the fluid domain. In two dimensions (x-z plane), this reduces to:

$$\frac{\partial^2 \phi_p}{\partial x^2} + \frac{\partial^2 \phi_p}{\partial z^2} = 0, \tag{4.8}$$

forming the starting point for linear wave theory. With suitable free-surface and seabed boundary conditions, this equation can be solved to obtain the horizontal velocity at hub depth.

Harmonic solution and first boundary condition

To model a wave traveling in the positive x-direction a harmonic solution is assumed:

$$\phi_p(x, z, t) = \Phi(z) \sin(kx - \omega t) \tag{4.9}$$

with wavenumber $k = 2\pi/L$, frequency $\omega = 2\pi/T$, and vertical amplitude function $\Phi(z)$. Substituting this into the Laplace equation (4.8) gives:

$$\frac{\partial^2 \phi_p}{\partial x^2} + \frac{\partial^2 \phi_p}{\partial z^2} = -k^2 \Phi(z) \cos(kx - \omega t) + \Phi''(z) \cos(kx - \omega t) = 0 \tag{4.10}$$

This leads to what is commonly referred to as the Helmhotz equation:

$$\Phi''(z) - k^2 \Phi(z) = 0 \tag{4.11}$$

The general solution to this second-order ordinary differential equation is a linear combination of hyperbolic functions:

$$\Phi(z) = A\cosh(k(z+h)) + B\sinh(k(z+h)) \tag{4.12}$$

where A and B are constants. To determine the values of these constants, the bottom boundary condition is applied. At the seabed ($z = -h$), there is no vertical flow, which implies:

$$\left.\frac{\partial \phi_p}{\partial z}\right|_{z=-h} = 0 \tag{4.13}$$

Differentiating the general solution and substituting $z = -h$:

$$\left.\frac{\partial \phi_p}{\partial z}\right|_{z=-h} = Ak\sinh(0) + Bk\cosh(0) = Bk = 0 \tag{4.14}$$

Since $k \neq 0$, it follows that $B = 0$. Therefore, the vertical velocity condition at the seabed is satisfied only if:

$$\Phi(z) = A\cosh(k(z+h)) \tag{4.15}$$

By filling this in into equation 4.9, the velocity potential becomes:

$$\phi_p(x,z,t) = A\cosh(k(z+h))\sin(kx-\omega t) \tag{4.16}$$

By differentiating this equation, the horizontal velocity u and the vertical velocity w can be determined.

$$u(x,z,t) = \frac{\partial \phi_p}{\partial x} = -Ak\cosh(k(z+h))\cos(kx-\omega t) \tag{4.17}$$

$$w(x,z,t) = \frac{\partial \phi_p}{\partial z} = Ak\sinh(k(z+h))\sin(kx-\omega t) \tag{4.18}$$

Dispersion relation and other two boundary conditions

To express the potential in terms of the wave amplitude A_w, the surface boundary conditions can be applied. This requires using both the dynamic and kinematic free-surface conditions, applied at the still water level $z = 0$. Considering a progressive wave with the following water surface displacement:

$$\eta(x,t) = A_w\sin(kx-\omega t) \tag{4.19}$$

Now the kinematic free-surface boundary condition can be applied. This ensures the fluid particles stay on the surface:

$$\frac{\partial \eta}{\partial t} = \left.\frac{\partial \phi_p}{\partial z}\right|_{z=0} \tag{4.20}$$

Computing both sides:

$$\frac{\partial \eta}{\partial t} = \omega A_w\cos(kx-\omega t) \tag{4.21}$$

$$\left.\frac{\partial \phi_p}{\partial z}\right|_{z=0} = Ak\sinh(kh)\sin(kx-\omega t) \tag{4.22}$$

To compare both sides consistently, the amplitudes of the harmonic terms can be compared. Since $sin(kx-\omega t)$ and $cos(kx-\omega t)$ differ only by a phase shift, their amplitudes can be equated to obtain the following relation:

$$\omega A_w = Ak\sinh(kh) \tag{4.23}$$

Now, the third and final boundary condition of this derivation can be applied. This boundary condition balances the pressure at the surface, it is called the dynamic free-surface boundary condition:

$$\left.\frac{\partial \phi_p}{\partial t}\right|_{z=0} + g\eta = 0 \tag{4.24}$$

Filling in both terms:

$$\frac{\partial \phi_p}{\partial t} = -A\omega\cosh(kh)\cos(kx-\omega t) \tag{4.25}$$

$$g\eta = gA_w \sin(kx - \omega t) \tag{4.26}$$

Matching again the amplitudes:

$$A\omega \cosh(kh) = gA_w \tag{4.27}$$

Combining equations 4.23 and 4.27 after rewriting for A_w, leads to:

$$\frac{Ak \sinh(kh)}{\omega} = \frac{A\omega \cosh(kh)}{g} \Rightarrow \omega^2 = gk \tanh(kh) \tag{4.28}$$

This is the dispersion relation, which relates the angular frequency ω [rad/s], wave number k [rad/m], and water depth h [m]. It also ensures that the solution is physically consistent.

Final expression for the horizontal velocity:
Solving equation 4.23 for A leads to:

$$A = \frac{gA_w}{\omega \cosh(kh)} \tag{4.29}$$

Substituting this into equation 4.17 results in:

$$u(x, z, t) = \frac{gA_w k}{\omega} \cdot \frac{\cosh(k(z + h))}{\cosh(kh)} \cdot \sin(kx - \omega t) \tag{4.30}$$

This is the general form of the horizontal wave-induced velocity at any depth z, under linear wave theory. This derivation shows how potential flow theory, under linear wave assumptions, can yield a complete expression for the wave-induced flow field, which is essential for estimating forces on hydrokinetic turbines in wave conditions.

4.7.2. Deep water approximation

For this project, the deep water approximation is applicable. This approximation simplifies the wave equations under the assumption that the water depth is large compared to the wavelength. It is valid when $kh \gg 1$ (i.e. $h > L/2\pi$ with $k = 2\pi/L$). In this case,

$$\tanh(kh) \approx 1, \qquad \cosh(k(z + h)) \approx \tfrac{1}{2} e^{k(z+h)},$$

This leads to a simplified form of the general dispersion relation of equation 4.28:

$$\omega^2 = gk.$$

And the horizontal velocity expressed in equation 4.30 becomes (with $z < 0$) :

$$u(x, z, t) = \frac{gA_w k}{\omega} e^{kz} \sin(\omega t) \tag{4.31}$$

Similarly, the vertical velocity component is given by:

$$w(x, z, t) = \frac{gA_w k}{\omega} e^{kz} \cos(\omega t) \tag{4.32}$$

When interested in the flow velocity at a certain fixed location, like with a hydrokinetic turbine, the x can be set to zero and the cosine term therefore becomes $cos(\omega t)$. This can then be plotted for different combinations of wave amplitudes and heights. The z value in the case of a turbine can be chosen as the hub depth, to get an average flow velocity over the blades. The hub depth will be chosen as 0.6 m in this case, which means the tip of the rotor is 0.23 m below the water surface, corresponding to slightly more than half a radius tip submergence. In equation 4.31, the vertical decay of wave-induced motion is clearly visible through the exponential factor e^{kz}, which shows that wave effects diminish rapidly with depth. The larger the submergence depth, the fewer the turbine will notice from the wave induced motions. Figure 4.19 shows the wave-induced velocity at hub depth, using a typical wave case.

Equation 4.31 can also be used to calculate the maximum velocity as a result of the waves, combined with the free-stream inflow velocity:

$$u_{\text{max}} = \frac{gA_w k}{\omega} \cdot e^{kz} + U_\infty \tag{4.33}$$

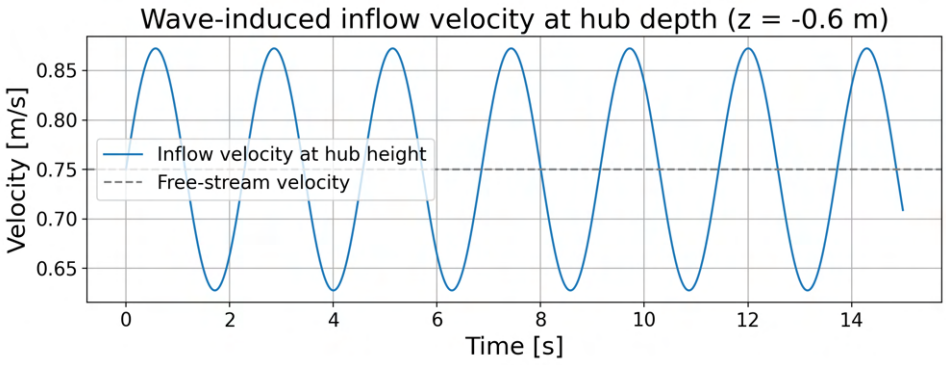

Figure 4.19: Wave-induced velocity at hub depth for wavelength $L = 4$ m, amplitude $A_w = 0.08$ m (wave steepness $\varepsilon = 0.04$).

This derivation is based on linear wave theory, valid for $\varepsilon \lesssim 0.04$ (Dean et al. 1991). Where ε is the steepness of the wave, which can be expressed as the wave height over the wavelength:

$$\varepsilon = \frac{2A}{L} \tag{4.34}$$

For steeper waves, nonlinear effects increase crest velocities and should be considered for accurate loading predictions.

4.8. Static deflection and strength test

To assess the structural performance of blade trial 2 (see section 4.6.6), a static deflection test was carried out. Because the material properties of the 3D-printed blade with carbon reinforcement are difficult to predict, an experimental approach was chosen to evaluate stiffness, deflection, and failure risk under representative loads. The test setup is shown in figure 4.20.

Figure 4.20: Experimental setup blade deformation test.

A plastic bag was used to apply weights at a distance of approximately 0.2 m from the root, which corresponds to the equivalent thrust loading position calculated using BEMT for a TSR of 4 (see section 4.6.7). It was chosen to test the blade in thrust direction as the forces in this direction are largest and the blade is the thinnest in this direction, meaning this will be the critical loading case.

The deflection at the load point was measured for various load values up to 9 kg. Beyond this value deflections became difficult to measure, but the blade did not fail up to the rig limit of 15 kg. A quadratic

curve was fitted to the measurement data to capture potential nonlinear deformation behavior at higher loads and to capture the accuracy of the measurements. As shown in figure 4.21, the fit closely matched all measurements.

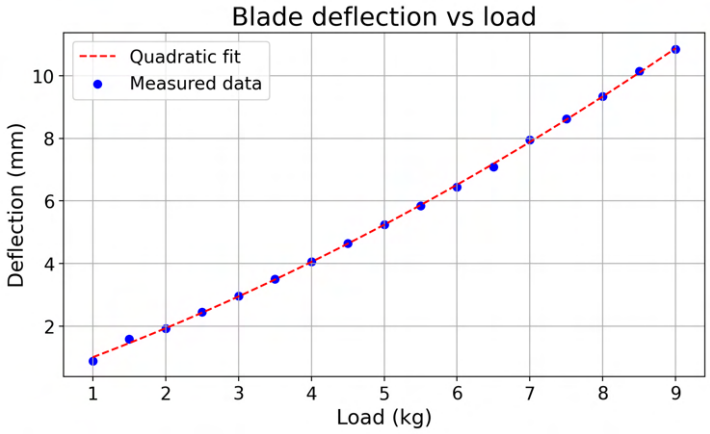

Figure 4.21: Measured deflection against load at ≈ 20 cm with quadratic fit.

From the linear portion of the deflection curve (approximately up to 4-5 kg), an effective structural stiffness of 1.03mm/kg was determined by fitting a linear regression to the measured data and taking the slope. This corresponds to approximately 9.8N/mm when accounting for gravitational acceleration. To relate this to the blade's bending stiffness, the static deflection of a cantilever beam subjected to a point load at a distance d from the fixed end can be described by:

$$\delta = \frac{Fd^2(3L_1 - d)}{6EI} \tag{4.35}$$

where δ is the measured deflection, F is the applied force, L_1 is the total blade length, and EI is the bending stiffness (product of Young's modulus and the second moment of area). Rearranging equation 4.35 gives:

$$EI = \frac{FL_1^2(3L - L_1)}{6\delta} \tag{4.36}$$

Using this expression and the known geometry ($L_1 = 0.32$ m, $d = 0.2$ m), the bending stiffness of the blade was estimated to be approximately $27.55\,\mathrm{N\,m^2}$. As the blade consists of a 3D printed shell (20% infill) with an embedded carbon rod, the internal material and geometric complexity make it difficult to isolate E or I. However, the effective EI value determined from testing is still valuable for comparison with numerical simulations and for evaluating future design iterations. The applied beam theory follows standard assumptions for small deflections and linear-elastic behavior, as found in for example Hibbeler (2018).

Tip deflections for increasing loads were calculated from beam theory and are listed in table 4.3. These values can be compared to equivalent thrust predictions from figure 4.17a. The maximum expected thrust at 1 m/s inflow and a TSR of 7 is about 202 N, while the blade was tested up to 264 N without failure. Even 15kg, or 441 N of thrust did not break the blade, although the deflection would likely significantly alter the results. From figure 4.19 it can be seen that the maximum velocity at hub height can reach 1.28 m/s, which gives a corresponding thrust of 331 N.

At 15kg, the blade showed no failure and returned to its original shape after unloading, indicating elastic behavior. A slight visual deformation (color difference) was observed near the point where the 6mm carbon rod ends, suggesting a region of high strain. However, no visible damage or permanent deformation occurred.

This prototype used only six inserts, although the final hub design was updated to eight (section 4.9). Despite the reduced number, all inserts withstood the maximum load without damage.

Table 4.3: Measured and estimated blade deflections under static loads. Estimates are from cantilever beam theory; measured values were taken at $r/R = 0.2$.

Load (kg)	Force per blade (N)	Thrust (N)	Measured defl. (mm)	Estimated tip defl. (mm)
1.0	9.81	29.43	0.88	1.70
2.0	19.62	58.86	1.92	3.39
3.0	29.43	88.29	2.96	5.09
4.0	39.24	117.72	4.06	6.79
5.0	49.05	147.15	5.25	8.48
6.0	58.86	176.58	6.45	10.18
7.0	68.67	206.01	7.96	11.87
8.0	78.48	235.44	9.35	12.72
9.0	88.29	264.87	10.85	15.27

4.9. Improving the hub

The hub design was slightly adjusted for the final version, mainly by changing the hole patterns at both the blade-to-flange and hub-to-flange connections. The key change was increasing the number of blade inserts from six to eight, motivated by analytical load estimates, followed by a verification of the flange stresses.

4.9.1. Insert load calculation and hub redesign

To estimate axial insert forces under worst-case bending, an analytical model was developed using the bending moment generated by either thrust or torque acting at a known moment arm:

$$M = F \cdot r_{\text{arm}} \tag{4.37}$$

For thrust loading, the maximum expected force per blade of $F = 67$ N from BEMT was applied at a distance of $r_{\text{arm}} = 0.197$ m (see section 4.6.7), resulting in a total moment of $M = 13.2$ Nm. Assuming the bending axis at the middle of the blade root (from $\theta_i = 0°$to 180°), only the two bolts located above the bending axis ($\theta_i = 60°$and 120°) were assumed to carry axial tension, leading to a conservative estimate. Through these assumptions, the problem basically becomes a beam problem, with a connection to the wall via bolts. The respective lever arms per bolt were computed as:

$$r_i = R_b \cdot \sin(\theta_i) \tag{4.38}$$

With $R_b = 0.0175\,\text{m}$ denoting the radius of the bolt circle and θ_i representing the angular position of each bolt in radians (see figure 4.22).

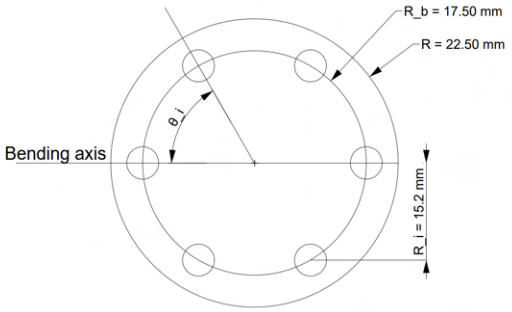

Figure 4.22: Insert hole geometry and parameters used in the hub load analysis.

The axial force F_i in bolt i due to a bending moment M was estimated using the following expression:

$$F_i = \frac{M \cdot r_i}{\sum r_j^2} \tag{4.39}$$

The denominator $\sum r_j^2$ is the sum of the squares of the vertical lever arms for all bolts assumed to be carrying tensile load (those located above the bending axis). The applied moment M is assumed to be entirely resisted by the axial forces in the active bolts, and this formula distributes the load according to the contribution of each bolt to the moment equilibrium. This relation is commonly used in bolt pattern force distribution analyses, as described in standard design texts such as Budynas et al. (2015) and supported by online engineering references like Mechanicalc (2025).

This yielded a maximum axial force of 435 N per insert (454 N including torque), well above the 300 N determined in pull-out tests (section 4.2). With eight inserts, loads reduced to 324 N, only slightly above the tested strength. Following Payne et al. (2017), inserts were placed more densely in the thrust direction, which also improved assembly by limiting blade orientations to two positions.

To cross-check, a simplified SolidWorks simulation was run with the eight-hole configuration (figure 4.23). Standard mesh settings were used, and circular holes replaced kidney slots. The maximum axial bolt forces were 88% lower than predicted analytically, reflecting the additional support provided by compression on the pressure side and a different effective rotation axis. The flange strength was also tested in the same simulation. The highest von Mises stress in the flange was 2.1×10^7 N/m^2, giving a safety factor of 8.1 relative to stainless steel yield strength. The 3D-printed blade therefore remains the weakest link in the system.

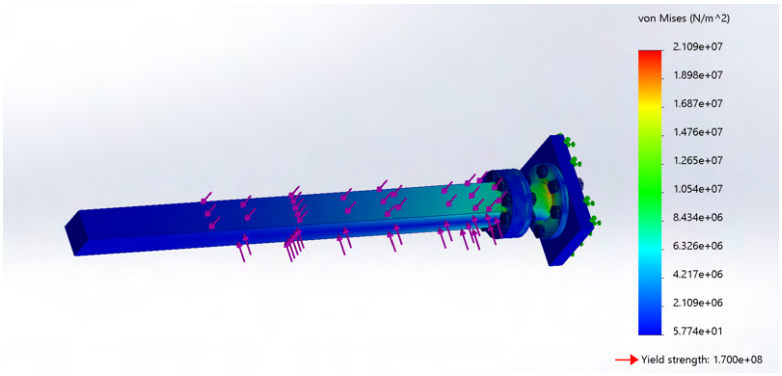

Figure 4.23: Simulation setup used in SolidWorks to evaluate bolt loading under bending.

While the simulation results suggested that the insert loads would remain within safe limits, the analytical model was used as the primary reference to ensure a conservative safety margin. With six inserts, predicted loads exceed the tested limit (section 4.2) at inflow velocities above 1 m/s. BEMT may also underestimate the hydrodynamic loads slightly. Combined with unsteady loading conditions (see section 4.7), this uncertainty could lead to significantly higher forces on the inserts under certain testing conditions. Increasing to eight inserts reduced the maximum load per insert by ≈30%, providing a safer margin for testing at higher flow speeds.

The updated hub design with eight insert holes replaced the original six-hole layout inspired by the Payne et al. (2017) turbine. This change was made after the initial blade had already been printed, which explains why the static strength test (see chapter 4.8) was performed using the six-insert configuration. While that configuration did not fail under load, demonstrating a robust connection in combination with the carbon rod, it was decided to proceed with the eight insert design for added structural redundancy and long-term reliability under fatigue loading.

For safety, the maximum inflow velocity during testing was limited to 0.9 m/s. Analytical estimates showed that higher velocities could bring insert forces close to the 300 N pull-out strength. At the same time, tip deflections already became significant at this velocity (table 4.3), which could affect turbine performance (requirement 2.2). The conservative velocity limit therefore ensured safe testing while maintaining realistic operating conditions.

4.9.2. Hole pattern on triangular hub

The hub-to-flange hole pattern was also revised following manufacturer feedback. Like explained in section 4.4, the available thread depth in the original design was only about 7 mm, which was marginal for reliable tapping. Shifting the holes toward the front and rear edges increased the effective depth to at least 9 mm, ensuring stronger threads. Since the hub-to-flange interface is significantly more rigid than the blade insert connections, this change is not expected to affect the structural performance.

Additionally, the updated hole locations are now better aligned with the main thrust loading direction. The revised pattern also simplifies assembly: similar to the blade-to-flange interface (see section 4.9.1), the parts can now only be mounted in two possible orientations, reducing the risk of incorrect installation.

Centrifugal force

In addition to hydrodynamic loads, the rotating blades experience centrifugal forces. Although small due to the low rotational speed and low blade mass, they still introduce a tensile load on the root inserts. The total centrifugal force per blade is given by (Hibbeler 2016):

$$F_{\text{centrifugal}} = m \cdot r \cdot \Omega^2 \tag{4.40}$$

where m is the blade mass, r is the distance from the rotation axis to the center of mass of the blade, and Ω is the angular velocity in radians per second. The mass of the blade including the carbon rod and the insert is $m = 0.12$ kg, a center of mass at $r = 0.150$ m, and a rotational speed of $n = 181$ rpm (i.e., $\Omega \approx 18.95$ rad/s), the resulting centrifugal force then becomes 6.46 N.

Equally distributing the force over the eight inserts results in a maximum extra pulling force of 0.8 N per insert, which is negligible compared to the forces resulting from torque and thrust.

4.9.3. Final blade design

The blade design is finalized with the parameters listed in table 4.2. Eight holes are used for the hub flange to blade connection, see figure 5.2b for the constructed flange that will be used in the experiments. The working drawing of both the triangular hub and the flanges are provided in Appendix C.2 and C.3.

A 3D printed blade is shown in figure 4.24. A carbon rod with differing thicknesses along the blade length is inserted. Different tubes are joined together, with dimensions given in figure C.1. This design is considered robust, manufacturable, and ready for the experimental validation phase described in the next chapter.

Figure 4.24: 3D printed blade

5

Experimental validation

In the preceding chapters, the turbine was designed and its expected performance was established. Chapter 2 introduced and validated the BEMT predictions, which were then used to guide the sensor and motor selection. Chapter 3 presented the nacelle concept and structural considerations, resulting in a feasible design. However, due to budget constraints the nacelle was not manufactured and the current experiments were instead carried out using the existing TU Delft gondola, which was designed to test ship propellers at model scale. Finally, chapter 4 focused on the design of the blades and hub, including predictions of thrust and torque under operating conditions. Together, these chapters provided the theoretical and design basis for testing the model-scale turbine. This chapter addresses the sub-question:

How can the constructed turbine blades and hub be tested and evaluated to validate structural integrity and assess the accuracy of performance predictions, ensuring readiness for future experiments?

The main goals of the experimental tests are:

- Confirming the structural integrity of the turbine and its blades, including visualizing tip deflection and checking that no parts fail under load.
- Comparing measured thrust, torque, and power coefficients with BEMT predictions made earlier in the project (see section 4.6.7).
- Assessing whether the current gondola mounting setup is suitable for further experiments, or whether the dedicated nacelle design described in section 3 should be developed instead.
- Quantify the effect of waves on the performance of the turbine.

By meeting these goals, the tests will show whether the turbine in combination with the gondola is ready for future campaigns, including more detailed work on, for example, unsteady inflows and dynamic stall.

Based on the static test results described in section 4.8, the blades are not expected to fail during operation. The stainless steel hub has a significantly higher strength than the blades and is therefore also not expected to fail. Tip deflection is expected to differ from the static test predictions, as the operational loading will be distributed along the blade length rather than applied as a point load. Performance-wise, BEMT is expected to predict torque and thrust within approximately 10% of the experimental values, as the method is validated in section 2.6. The gondola setup should, in theory, provide accurate measurements while allowing control over the rotational speed to achieve different tip-speed ratios. The installed sensor has a sufficiently large range to accommodate the expected loads (see section 5.1.3).

5.1. Experimental setup

The following subsections describe the facility, turbine model, instrumentation, and measurement procedures that together form the experimental setup. The goal is to provide sufficient detail for replication and to explain how the setup enables the validation objectives outlined in section 1.6.1.

5.1.1. Test facility

The experiments were carried out in the towing tank at TU Delft (*Towing tank No.1* 2025). The tank measures 142 m in length, 4.22 m in width, and 2.3 m in maximum depth. For these tests, the water depth was set to 2.19 m. The carriage can reach towing speeds of up to 7 m/s. The water temperature during testing was approximately $26°C$ and consisted of fresh water at atmospheric pressure. At this temperature, the density is $\rho = 996.79\ \mathrm{kg/m^3}$ and the kinematic viscosity is $\nu \approx 8.72 \times 10^{-7}\ \mathrm{m^2/s}$ (Lemmon et al. 2025).

One advantage of this facility is its relatively large cross-section, which allows testing of turbine models with diameters closer to those used in full-scale designs. Based on the reviewed literature, towing tanks are generally associated with larger model diameters than flume tanks, with averages of about 0.84 m and 0.54 m, respectively, as calculated from the studies summarized in table 1.1.

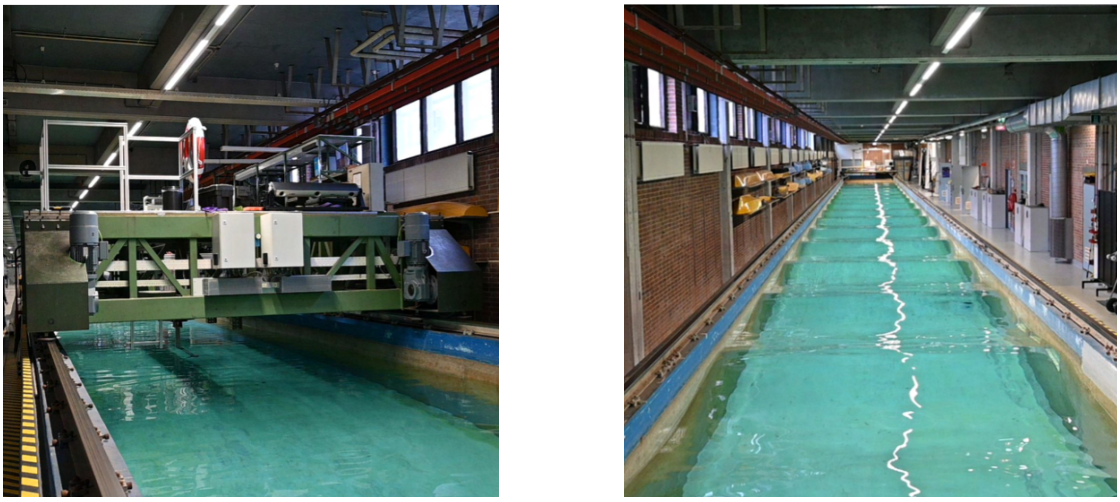

(a) Towing carriage.

(b) Waves in the towing tank

Figure 5.1: Test facility at the TU Delft.

The turbine was mounted to the towing carriage via a hexapod, which allowed adjustment of its vertical position. The rotor axis was set at a depth of 0.62 m below the free surface, corresponding to a blade tip submergence of 0.25 m, which is more than the minimum of $0.5R$ submergence recommended by the literature (Kolekar et al. 2015, Guo et al. 2018). This depth was chosen to place the rotor sufficiently close to the surface to capture wave effects, while ensuring the blade tips did not emerge in the largest tested waves. Alignment in the yaw direction (rotation around the vertical z-axis) was performed using a rope with a weight, ensuring that the rotor faced the incoming flow without any yaw angle.

5.1.2. Turbine model

The turbine used in this study consists of three blades mounted to a triangular hub, connected via a shaft to the gondola. The details on the design of the blades can be found in section 4.6. The turbine used in this study has a diameter of 0.74 m, resulting in a blockage ratio of approximately 4.5%, which is below the commonly accepted 5% threshold for minimizing blockage effects (see section 1.3.8). The blade geometry, including chord distribution, twist angles, and radial stations, is defined in table 4.2.

The blades were 3D-printed in Polylactic Acid (PLA) using a print orientation of $30°$ relative to the build plate. This orientation improves strength along the span while maintaining dimensional accuracy. After printing, the blades were post-processed by sanding the surface and applying a thin layer of epoxy resin to improve water resistance and decrease surface roughness (see figure 4.24). Each blade has an internal carbon rod to increase stiffness, with approximately 30 mm of the rod extending beyond the blade root for insertion into the flange connection (see figure 5.2a). Between the flange and the blade, a 3D-printed pitch plate was inserted to define the blade pitch angle (see figure 5.2c).

The hub has a triangular shape, originally designed to be manufactured from stainless steel for maximum strength. Due to manufacturing issues, the hub was instead fabricated from PVC to ensure the

experimental campaign could proceed as scheduled. Figure 5.2b shows the hub with the three flanges mounted to the triangular part. The hub connects to the turbine shaft via a keyway, allowing transmission of torque and thrust to the gondola assembly. As shown in figure 5.3, the grey hub cap and orange transition piece were added to smooth the flow over the hub region and to provide a smooth interface between the blades and the nacelle of the gondola. The gondola was originally designed for propellers with a smaller hub diameter of 35 mm; however, the current 120 mm hub design fits securely using this transition arrangement.

(a) Blade root with carbon rod extension. **(b)** PVC triangular hub with flanges. **(c)** Pitch plate 0 degrees.

Figure 5.2: Turbine components: (a) blade root with carbon rod extension, (b) triangular PVC hub used in experiments (c) pitch plate.

5.1.3. Instrumentation

Torque and thrust were measured using a strain gauge based dynamometer (type 232S), custom-made by MARIN. The turbine rotor was mounted directly on the shaft of the sensor, eliminating intermediate components such as bearings and thereby avoiding any losses. The sensor has a torque range of 14 Nm with a safe overload capacity of 18 Nm, and a thrust range of 340 N with safe overload up to 430 N. Based on the predictions shown in section 4.6.7, the sensor range covers the entire operating envelope of the turbine, and no test conditions need to be excluded at this stage.

Calibration data from earlier tests were available and still valid, so a new calibration was not required for these experiments. The calibration coefficients used are 214.164 N/(mV/V) for thrust and 8.839 Nm/(mV/V) for torque.

Rotational speed was measured with a $10,000$ ppr encoder mounted on the shaft. Data from the rotating shaft were transferred via a slip ring, after which the cables exited through the gondola strut and were routed to the data acquisition system on the towing carriage.

5.1.4. Control & operating conditions

The gondola houses two in-line motors that regulate the rotational speed of the rotor. A PI controller was implemented (Appendix E.1), with all parameters fixed during the campaign except for the proportional gain K_p, which was adjusted in some cases to improve performance. In most conditions, $K_p = 0.651$ was applied, while for tests at 0.5 m/s and the first few runs at low TSR the gain was halved ($K_p = 0.325$). This reduced cogging at low rotational speeds and provided more stable control, although some cogging remained visible.

Three inflow velocities were selected for the steady-state experiments: 0.5 m/s, 0.75 m/s, and 0.9 m/s. These values were chosen based on earlier research and to represent realistic inflow conditions (see section 1.6.2). Within each velocity, TSR values between 3 and 7 were tested in increments of 0.5, with additional runs near the optimum to better identify the maximum power coefficient.

Following the steady inflow campaign, wave conditions were introduced. Prior to turbine-wave runs, wave-only tests (carriage velocity 0 m/s) were performed to establish the undisturbed wave characteristics. The measured wave parameters are summarized in table 5.1. All turbine runs with waves were

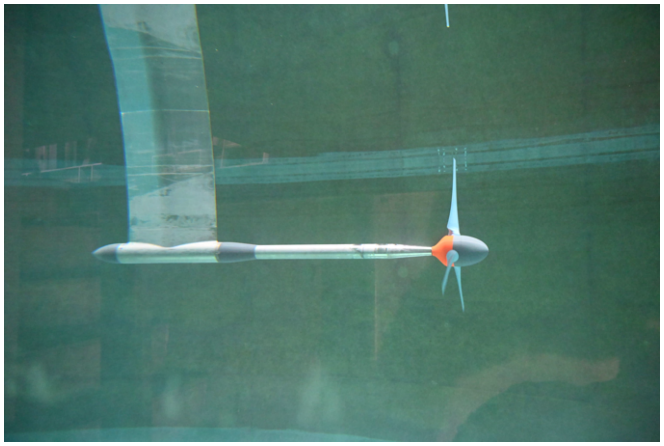

Figure 5.3: Turbine setup underwater photograph.

carried out at $0°$ pitch and at optimal TSR, determined from the steady inflow conditions. Not all combinations of steepness and inflow velocity were tested; in particular, the largest wave cases at 0.75 m/s were omitted (see table 5.1), as they would have produced excessive hydrodynamic loading and risked damaging the setup. The wave length is defined as λ, wave amplitude as A_ω, wave period as T_ω and the steepness as ε. The velocity conditions listed in the table correspond to the operating points used in the subsequent turbine experiments in following wave conditions.

Table 5.1: Measured wave conditions used in the experiments. Wave periods (T_ω) were calculated using linear wave theory. Each case was tested under following wave conditions.

T_ω [s]	λ [m]	ε [-]	A_ω [m]	U_∞ [m/s]
1.13	2.00	0.024	0.024	0.5, 0.75
1.13	2.00	0.046	0.045	0.5, 0.75
1.13	2.01	0.064	0.064	0.5, 0.75
1.60	4.00	0.021	0.041	0.5, 0.75
1.60	3.99	0.040	0.080	0.5, 0.75
1.61	4.03	0.045	0.091	0.5
1.94	5.89	0.020	0.059	0.5, 0.75
1.94	5.89	0.041	0.120	0.5

Finally, the blade pitch was adjusted to $5°$ using the pitch plates, which is the maximum achievable setting for this model. This condition was included to assess whether BEMT predictions capture the performance changes due to blade pitch variations.

5.1.5. Measurement protocol

For the steady inflow conditions, four different quantities were measured; torque, thrust, rotational speed and carriage velocity (see figure 5.4). Here, negative torque means the turbine is in generator mode. For the wave conditions, two wave probe locations were added: one in the middle of the tank in front of the turbine, and one near the wall of the tank, in the rotation plane of the turbine.

Each steady inflow run lasted 50 s, while wave tests were 120 s in duration.Approximately 20 minutes were taken between runs to allow for steady conditions to settle, and 30 minutes for unsteady conditions. The complete TSR range at 0.75 m/s was repeated twice, yielding consistent results and verifying the reliability of the measurements.

During steady inflow runs, TSR was held constant using the motors as a brake. The rotor was first brought up to speed in motor mode, after which the carriage was accelerated and the motors switched to generator mode, dissipating the generated energy in a resistor. This procedure allowed the rotational speed to be held constant throughout each run, see figure 5.4.

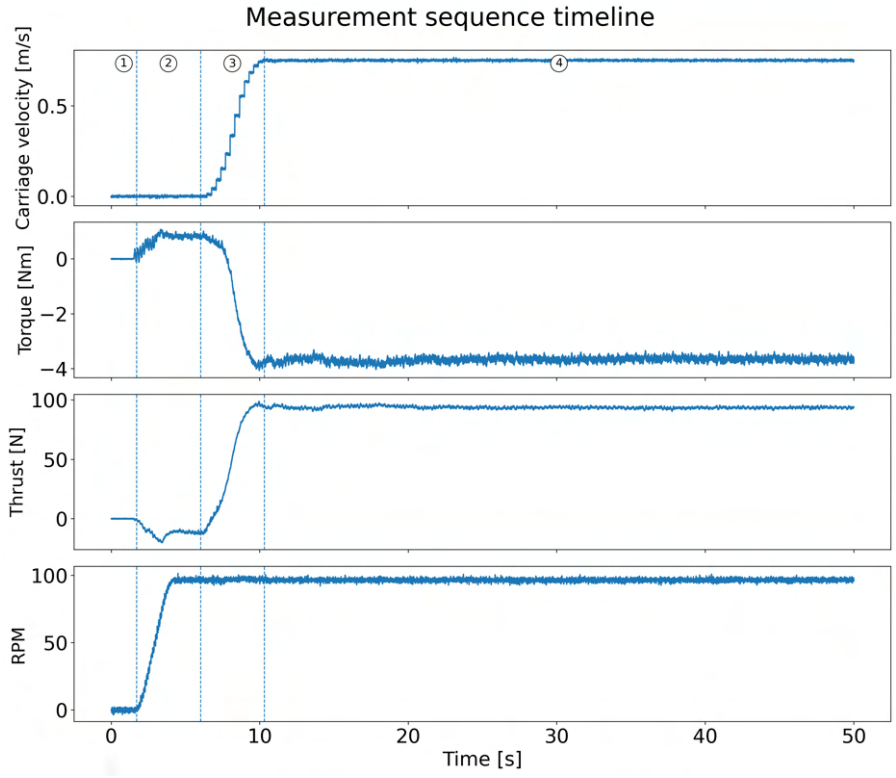

Figure 5.4: Stacked time series for carriage velocity, torque, thrust, and rpm at $U_\infty = 0.75$ m/s, TSR$= 5$, without waves. Vertical dashed lines mark phase boundaries; numbers on the top panel indicate: (1) 0-2 s standstill, (2) 2-6 s rotor acceleration, (3) 6-10 s carriage acceleration, (4) $t > 10$ s steady inflow (measurement window).

5.2. Data processing & analysis

This section describes the procedures applied to the raw measurements in order to obtain consistent performance data, extract wave-induced fluctuations, and estimate uncertainties. The steps include subtracting the zero measurements of the actual signals, analysis methods for steady and unsteady conditions and the definition of error bars.

5.2.1. Pre-processing of signals

All signals were corrected for sensor offsets using zero measurements taken prior to each test. This consists of a run of 50 s at standstill, and taking the average. The first part of every run was discarded to remove carriage acceleration and rotor spin-up. Figure 5.5a illustrates this procedure for a run at 0.75 m/s, with a TSR of 5, where the red interval indicates the stable portion of the record that was retained for the analysis.

For thrust measurements, extreme peaks were occasionally observed, leading to a noisy signal, see figure 5.5b. This was likely due to some technical issue with either the sensor or the slip ring. Most peaks were upwards, meaning that the average is not reliable anymore. To remove these outliers, a median filter was applied with a window size of 71 samples. This number gave smooth results by removing the peaks, but keeping the general trend. After the first few testing days this noise disappeared and the filtering was not needed anymore. A median filter works by replacing each data point with the median value of its neighboring samples within a chosen window. This makes it well suited for removing sharp outliers or spikes, while still preserving the overall signal shape. For a more detailed discussion of median filtering and its applications, see Pitas et al. (1990).

Figure 5.5b shows an example of the thrust signal before and after filtering, highlighting the removal of noise while preserving the actual mean level and actual fluctuations. A short time frame of 5 seconds was chosen for this figure, so it is easier to see the effect.

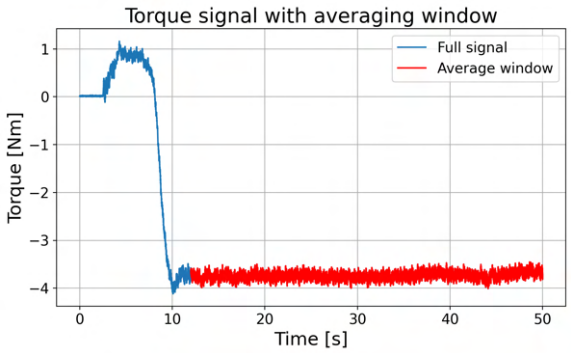

(a) Torque signal with averaging window highlighted.

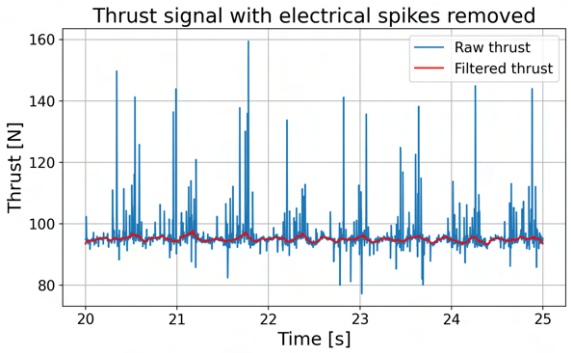

(b) Thrust signal after applying median filter.

Figure 5.5: Signal processing examples: (a) torque averaging window, (b) thrust signal filtering. Both for an inflwo velocity of 0.75 m/s, at a TSR of 5.

5.2.2. Signal analysis

For steady inflow conditions, mean values of torque, thrust, and rotational speed were calculated over the stable time interval. Standard deviations were also determined to quantify the scatter of the signal. For wave conditions, both the mean value and the oscillation amplitude were determined, providing a measure of the unsteady load variations induced by the waves.

A sine fit was applied to the wave probe signals in order to characterize the actual undisturbed wave conditions used in the experiments (see figure 5.6b). For the torque and thrust signals in wave conditions, a median filter was applied to remove noise in the signal, after which the maxima and minima of the time series were taken to quantify the load fluctuations induced by the waves (see figure 5.6a for an example).

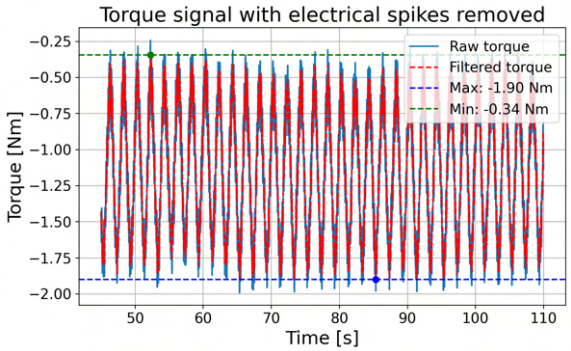

(a) Torque signal with minima and maxima indicated.

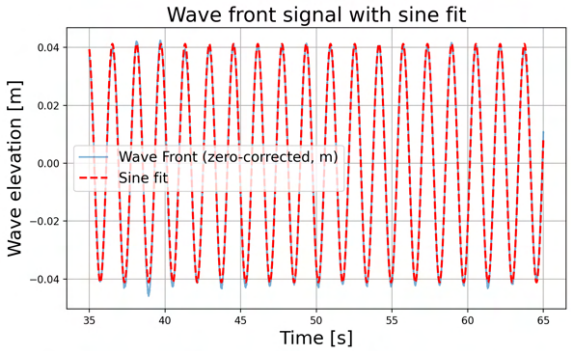

(b) Wave front signal with fitted sine curve.

Figure 5.6: Signal processing examples: (a) torque signal analysis, (b) wave signal with sine fitting. Both for a wave with $\lambda = 4$ m, and ε =0.02.

5.2.3. Uncertainty estimation

Uncertainty bounds are reported as $\pm 2\sigma$, where σ is the standard deviation of the time series. For a normal distribution this interval corresponds approximately to a 95% confidence range (Coleman et al. 2018), but here it is used as a conventional measure of variability, independent of the exact distribution of the signal.

To see how much each input contributes to the total uncertainty, a first-order (small-perturbation) sensitivity analysis is used. For a quantity $y = f(x_i)$ with independent inputs:

$$\left(\frac{\sigma_y}{y}\right)^2 = \sum_i \left(S_i \frac{\sigma_{x_i}}{x_i}\right)^2, \qquad S_i \equiv \frac{\partial \ln y}{\partial \ln x_i},$$

where S_i is the sensitivity: the percent change in y caused by a one-percent change in x_i. For products

and quotients it equals the variable's exponent (with a minus sign if in the denominator). Each input's percentage contribution is obtained from the squared terms in the sum.

TSR
For the tip-speed ratio, uncertainty arises from scatter in both the inflow velocity U_∞ and the rotational speed Ω. Assuming the fluctuations in U_∞ and n are independent, the relative uncertainty follows as:

$$\frac{\sigma_{TSR}}{TSR} = \sqrt{\left(\frac{\sigma_n}{n}\right)^2 + \left(\frac{\sigma_{U_\infty}}{U_\infty}\right)^2},$$

where σ denotes the (1σ) standard deviation of each quantity and $\Omega = 2\pi n$.

As a representative worst case, consider the lowest tested velocity ($U_\infty = 0.5\,\mathrm{m/s}$) and rotational speed ($n = 38.71$ rpm), with $\sigma_{U_\infty} = 0.002\,\mathrm{m/s}$ and $\sigma_n = 0.601$ rpm. Substitution gives

$$\frac{\sigma_{TSR}}{TSR} = \sqrt{\left(\frac{0.601}{38.71}\right)^2 + \left(\frac{0.002}{0.5}\right)^2} \approx 0.016,$$

so for $TSR = 3.0$ the absolute uncertainty is $\sigma_{TSR} \approx 0.048$ (1σ), i.e. a plotted band of $\pm 2\sigma \approx \pm 0.096$. Thus, even in the worst case, TSR uncertainty stays below ± 0.1. At higher inflow velocities and rotational speeds the relative terms $\sigma_{U_\infty}/U_\infty$ and σ_n/n decrease, so horizontal error bars would be smaller than the symbol size and are therefore omitted.

Performance coefficients.
Vertical error bars are shown for C_p and C_t. They are obtained by propagating the measured scatter in torque Q and thrust T through the coefficient definitions, while also accounting for the smaller contributions from inflow-velocity and rpm fluctuations. In practice, since $C_p \propto Q\,n\,U_\infty^{-3}$ (see equation 1.1), its relative uncertainty combines three terms in quadrature:

$$\left(\frac{\sigma_{C_p}}{C_p}\right)^2 = \left(\frac{\sigma_Q}{Q}\right)^2 + \left(\frac{\sigma_n}{n}\right)^2 + \left(3\frac{\sigma_{U_\infty}}{U_\infty}\right)^2,$$

and for $C_t \propto T\,U_\infty^{-2}$ (see equation (1.2)), its relative uncertainty combines two terms in quadrature:

$$\left(\frac{\sigma_{C_t}}{C_t}\right)^2 = \left(\frac{\sigma_T}{T}\right)^2 + \left(2\frac{\sigma_{U_\infty}}{U_\infty}\right)^2,$$

with ρ and A treated as constants and $\sigma_\Omega/\Omega = \sigma_n/n$.

For most operating points, the absolute uncertainty in torque remained fairly constant across the tested range. Only under the two most critical conditions did the scatter increase noticeably, which can be attributed to the cogging motion at low rotational speeds. Figure 5.7 clearly shows the increased error bars for the 0.5 m/s case at low rotational speeds. This also explains why the corresponding C_p values show larger error bars in these cases, while for most other conditions the uncertainties are of comparable magnitude.

At this highest uncertainty operating point ($U_\infty = 0.5$ m/s, $n = 38.71$ rpm), the coefficients are $C_p =$ 0.248 and $C_t =$ 0.517. The corresponding relative uncertainties are $\sigma_{C_p}/C_p \approx$ 14.1% and $\sigma_{C_t}/C_t \approx$ 7.5% (both at 1σ). The corresponding uncertainty analysis shows that C_p is almost entirely set by torque scatter, while C_t is dominated by thrust scatter. The velocity and rpm terms are present but comparatively small. The contributions with intermediate values are summarized in table 5.2.

Table 5.2: Error budget for C_p and C_t at the worst-case condition ($U_\infty = 0.5$ m/s, $n = 38.71$ rpm). Percentages indicate each input's share of the total variance (1σ).

Metric	Input	S_i	σ_{x_i}/x_i	$\lvert S_i\rvert\,\sigma_{x_i}/x_i$	Contribution [%]
C_p	Q	$+1$	0.14000	0.14000	98.2
C_p	Ω	$+1$	0.01553	0.01553	1.2
C_p	U_∞	-3	0.00400	0.01200	0.7
C_t	T	$+1$	0.07464	0.07464	98.9
C_t	U_∞	-2	0.00400	0.00800	1.1

As a consistency check at a second operating point without torque ripple ($U_\infty = 0.5$ m/s, $n = 51.62$ rpm; $Q = 1.352 \pm 0.101$ Nm, $T = 32.181 \pm 0.790$ N, $\sigma_U = 0.0019$ m/s, $\sigma_n = 0.607$ rpm), the totals reduce to $\sigma_{C_p}/C_p \approx 7.64\%$ and $\sigma_{C_t}/C_t \approx 2.57\%$ (1σ). The pattern remains the same: C_p is torque-dominated (95%) and C_t is thrust-dominated (91%), with the velocity and rpm terms contributing only a few percent in total. The C_p and C_t error bars reported in the figures include the contributions from U_∞ and n; these are small (order 1-9%) compared to Q and T, but are still included to provide a realistic uncertainty range.

5.3. Results

This section first examines thrust and torque under steady inflow conditions, followed by the related performance coefficients C_p and C_t. The influence of waves will then be analyzed and compared with the potential flow wave prediction model (see section 4.7.1). Finally, the measured tip deflection will be discussed and compared to the static predictions from section 4.8. These results will show whether the turbine design was successful and how well the different prediction methods performed. The practical use of the gondola can then also be evaluated to see whether a more advanced setup, as proposed in chapter 3, is necessary for future work.

5.3.1. Steady inflow conditions

For constant inflow conditions, thrust and torque were measured at four test cases: three reference conditions of $U_\infty = 0.5$ m/s, 0.75 m/s, and 0.9 m/s at the optimal pitch angle ($0°$), and one off-design case with $U_\infty = 0.75$ m/s at a pitch angle of $5°$.

As detailed in section 2.6, QBlade is the open-source BEMT code used in this thesis. Here the steady BEMT solver is used. A multi-polar simulation was performed using input polars at Reynolds numbers between 45,000 and 200,000. These values correspond to the Reynolds number at 75% blade radius for TSR = 3 at $U_\infty = 0.5$ m/s (lowest condition) and TSR = 7 at $U_\infty = 0.9$ m/s (highest condition). Three intermediate Reynolds numbers were also included, corresponding to a TSR of 5 for each inflow condition. QBlade interpolated between these values and across the different polar definitions.

For the simulations, the original foil shapes were used rather than the modified versions with truncated trailing edges required for 3D printing (see section 4.6.6). Using the unmodified foils gave better agreement, likely because BEMT does not handle the straight trailing edge geometry accurately. It is also uncertain whether the printed blade geometry is an exact match to the CAD model; small differences due to tolerances and post-processing could exist (see section 5.1.2).

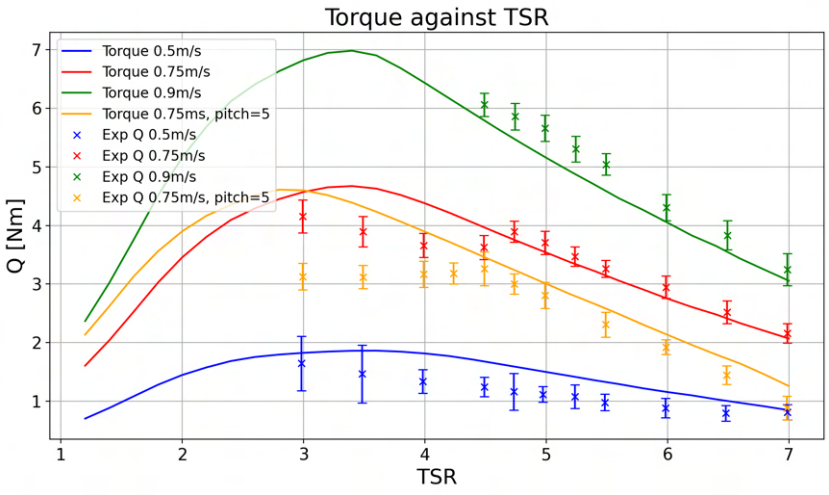

Figure 5.7: Torque comparison between BEMT and experimental results.

Overall, the measured and predicted thrust and torque compare well, see figure 5.7 and 5.8. In particular, the agreement is good for the zero-pitch cases at higher TSR, and thus at higher Reynolds numbers. The main discrepancies appear at lower Reynolds numbers, namely for the $U_\infty = 0.5$ m/s

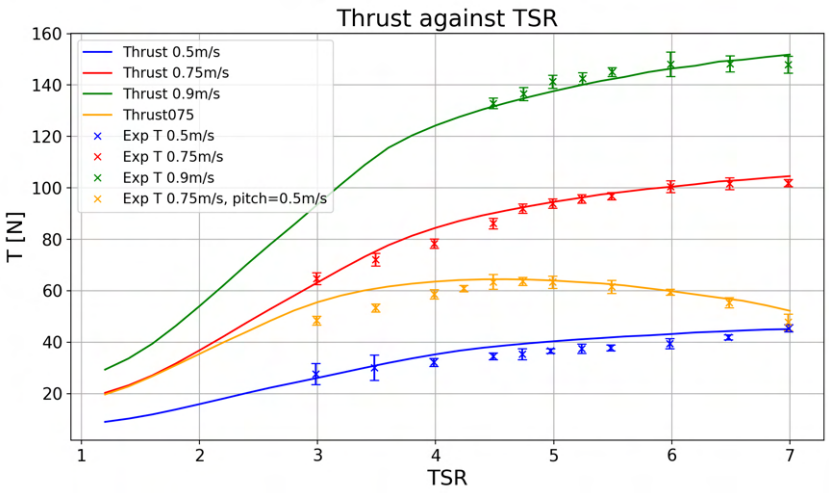

Figure 5.8: Thrust comparison between BEMT and experimental results.

case and the lower TSR values of the $U_\infty = 0.75$ m/s case, where BEMT systematically overpredicts the measurements. This trend is less pronounced in thrust but still visible. Since all $U_\infty = 0.75$ m/s conditions were repeated twice, it is likely that the discrepancy originates from the BEMT predictions rather than an experimental error.

Two possible explanations were considered: blade bending or low Reynolds number related flow effects. Blade bending is more severe at higher rotational speeds, where the agreement is actually better, making this an unlikely primary cause. Instead, the discrepancies show a clear dependence on Reynolds number. To investigate this further, figure 5.9 shows torque plotted directly against Reynolds number. A vertical line marks the maximum Reynolds number reached at $U_\infty = 0.5$ m/s ($Re \approx 1.1 \times 10^5$). This value also coincides with the transition point in the 0.75 m/s data: above $Re \approx 1.1 \times 10^5$, predictions and measurements align closely, while below this threshold the model consistently overestimates performance. At this threshold, the torque experiences a dip, before rising again at even lower Reynolds numbers, a feature not observed in previous studies. In every plot, the $U_\infty = 0.5$ m/s case at TSR = 7 aligns closely with the predictions, indicating that it has also entered the regime where QBlade's predictions are reliable.

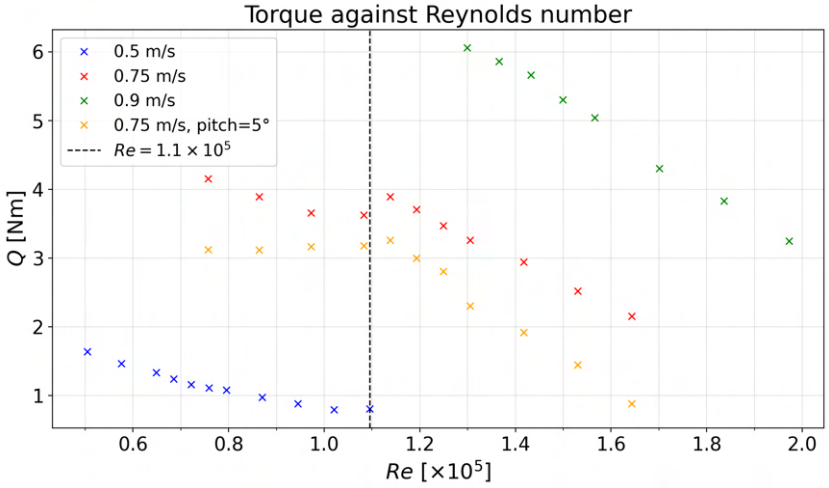

Figure 5.9: Torque vs Reynolds number. Re is evaluated at $r/R = 0.75$ using the local chord (0.041 m) as length scale and the local relative velocity $U_{\text{rel}} = \sqrt{U_\infty^2 + (\Omega r)^2}$. The dashed line marks the approximate transition Reynolds number.

Limitations of BEMT predictions at low Reynolds numbers

The observed discrepancy at Reynolds numbers below approximately $Re \approx 1.1 \times 10^5$ can be explained by the limitations of BEMT as it relies on XFOIL-generated polars. BEMT itself is not inherently inaccurate, its predictive accuracy depends directly on the quality of the lift and drag input data. At higher Reynolds numbers, foil performance is well captured by XFOIL, and the resulting BEMT predictions agree closely with experiments. However, at lower Reynolds numbers, systematic overprediction of lift and underprediction of drag can be observed.

The underlying reason likely lies in the characteristics of the boundary layer. At high Reynolds numbers, transition from laminar to turbulent flow occurs relatively early along the chord. The turbulent boundary layer is more resistant to adverse pressure gradients, making it less prone to early separation and easier to predict with simplified models (Drela et al. 1987). By contrast, at low Reynolds numbers the boundary layer remains laminar over a larger fraction of the chord. Laminar flow is far more sensitive to adverse pressure gradients, and separation can occur upstream of the natural transition point (Drela et al. 1987). In such cases, a laminar separation bubble may form, in which the flow separates, transitions within the separated shear layer, and then reattaches downstream (Chen et al. 2008). The size and location of this bubble strongly influence lift and drag, and small changes in Reynolds number, angle of attack, or surface roughness can lead to highly nonlinear performance shifts (Traub 2019).

When the separated shear layer fails to reattach quickly, the laminar separation bubble can “burst”, stretching into a long bubble or even developing into a fully detached shear layer. For foils this creates a large recirculation zone, which flattens the pressure distribution, reduces lift, and increases drag (Jahanmiri 2011). At very low Reynolds numbers, the flow may not reattach at all, so no bubble forms, the separated shear layer simply persists downstream. This leads to a sudden loss of performance, effectively the onset of stall (Genç et al. 2012). The sharp drop in torque and thrust seen in the present experiments below $Re \approx 1.1 \times 10^5$ is consistent with this behavior, where the flow separates and does not reattach.

Predicting these phenomena reliably is challenging. XFOIL employs an e^n transition model and an integral boundary-layer formulation (Drela 1989). While effective at higher Reynolds numbers, these models cannot fully capture the complex dynamics of laminar separation and reattachment. In practice, XFOIL often predicts later separation and earlier reattachment than observed in experiments, effectively assuming that the flow remains attached for longer than it does in reality (Chen et al. 2008). This results in optimistic lift predictions and drag levels that are too low, which is consistent with the overprediction of torque and thrust observed below $Re \approx 1.1 \times 10^5$

Power and thrust coefficients

The non-dimensional performance coefficients C_t and C_p largely follow the same trends observed in thrust and torque, respectively. For C_t, the agreement between BEMT predictions and experiments is generally good, especially at higher TSR’s. The overall shape of the C_t curves is also captured well, confirming that QBlade can reproduce the thrust behavior with reasonable accuracy.

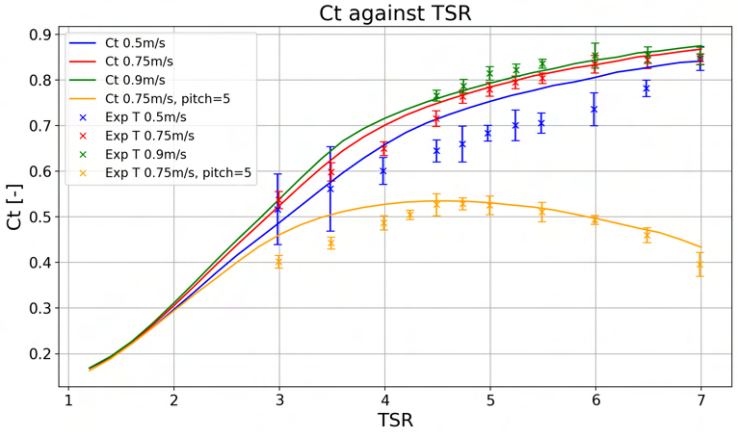

Figure 5.10: C_t comparison between BEMT and experimental results.

For C_p, a similar trend is observed, but with slightly larger discrepancies. The error bars for C_p are also noticeably larger, as shown in figure 5.11a and 5.11b, which is consistent with the uncertainty analysis described in 5.2.3. Despite these uncertainties, the general behavior of the curves is reproduced, and the predicted efficiency levels are in the correct order of magnitude. The discrepancies happen at the same locations as for the torque pot, but more pronounced. The C_p curves are split into two plots to avoid overlap. Figure 5.11a shows the $U_\infty = 0.75$ m/s cases at two pitch angles, and figure 5.11b shows the $U_\infty = 0.9$ m/s and $U_\infty = 0.5$ m/s cases.

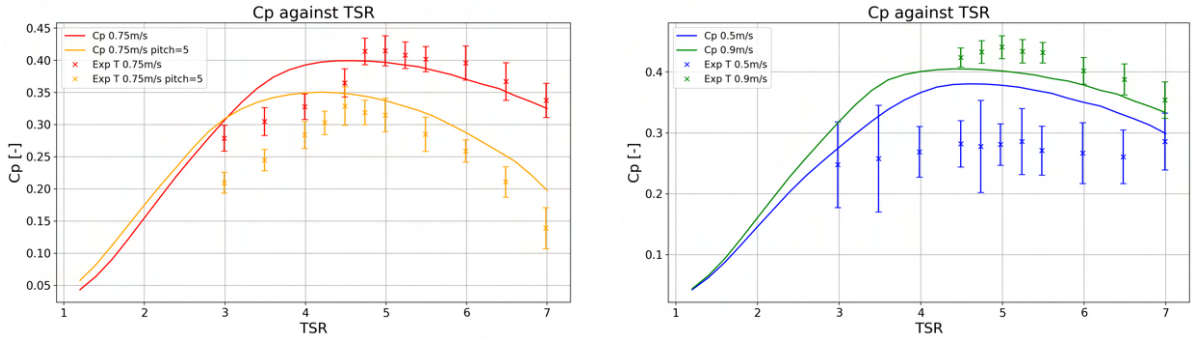

(a) 0.75 m/s with $0°$ pitch and 0.75 m/s with $5°$ pitch.

(b) 0.5 m/s with $0°$ pitch and 0.9 m/s with $0°$ pitch.

Figure 5.11: C_p comparison between BEMT and experimental results.

The off-design case at $U_\infty = 0.75$ m/s with a pitch angle of $5°$ shows larger discrepancies. Here, QBlade does not capture the performance reduction accurately, which suggests that the method is better suited for predicting near-design operating conditions than for off-design cases. This is likely related to QBlade's reliance on XFOIL polars, which are less reliable at large angles of attack, where flow separation and stall dominate the behavior.

A key parameter for turbine design is the maximum power coefficient C_p and the TSR at which it occurs. These values are summarized in table 5.3. For the $U_\infty = 0.75$ m/s and $U_\infty = 0.9$ m/s cases, the optimal C_p is predicted within 10% of the experimental value, which aligns with the accuracy expected based on previous with Guo et al. (2018), in section 2.6. However, in all cases the predicted optimal TSR is slightly lower than observed experimentally. The most likely explanation for this systematic offset is blade bending: even small changes in effective twist angle or angle of attack due to deflection can shift the operating point, and a few degrees of deviation can already move the peak efficiency location.

For the steady inflow cases of 0.5 m/s, it is hard to determine the exact optimal TSR location, as the C_p values are fluctuating around an optimal point. Therefore, no single optimal TSR is reported for this case. The peak C_p is substantially overpredicted, likely due to the low Reynolds number effects discussed above.

Table 5.3: Comparison of optimal C_p between BEMT predictions and experimental results.

Condition	$C_{p,\text{BEMT}}$	TSR (BEMT)	$C_{p,\text{Exp}}$	TSR (Exp)	Relative difference C_p
$U_\infty = 0.9$ m/s, pitch $0°$	0.405	4.4	0.441	5.0	-8.2%
$U_\infty = 0.75$ m/s, pitch $0°$	0.400	4.5	0.415	5.0	-3.6%
$U_\infty = 0.5$ m/s, pitch $0°$	0.381	4.6	0.286	4.5–5.25	25.0%
$U_\infty = 0.75$ m/s, pitch $5°$	0.351	4.2	0.329	4.5	6.3%

The results suggest that full Reynolds independence has not yet been reached, since there is still a difference between the $U_\infty = 0.75$ m/s and $U_\infty = 0.9$ m/s case. The difference is already smaller than the difference with the $U_\infty = 0.5$, indicating that Reynolds independence is approaching.

Full-scale performance estimate

To provide an estimate of the power production capability of the turbine at full scale, the measured performance was extrapolated using Froude scaling. With a scale factor of 21.5, the modeled inflow

velocities of 0.5 m/s, 0.75 m/s and 0.9 m/s correspond to full-scale velocities of 2.32 m/s, 3.48 m/s and 4.17 m/s, respectively. The full-scale rotor diameter of 16 m (table 1.4) gives an area of:

$$A = \pi R^2 = \pi \cdot 8^2 \approx 201 \text{ m}^2.$$

The turbine power is estimated using the standard power equation:

$$P = \tfrac{1}{2}\rho A C_p U^3,$$

where $\rho = 1000$ kg/m^3 is the water density, A_t the rotor swept area, C_p the power coefficient, and U_∞ the inflow velocity. For this case, a single value of $C_p = 0.441$ (corresponding to the $U_\infty = 0.9$ m/s case) was used for all cases. This choice is justified because the 0.9 m/s case is closest to the Reynolds-independent regime and therefore most representative for full-scale performance. The results are shown in table 5.4 for different inflow conditions that were used.

Table 5.4: Estimated full-scale power output of a 16 m turbine at maximum efficiency.

$U_{\infty,\text{model}}$ (m/s)	$U_{\infty,\text{full}}$ (m/s)	C_p	P_{full} (kW)
0.50	2.32	0.441	552
0.75	3.48	0.441	1,863
0.90	4.17	0.441	3,382

It can be seen that at full scale, the turbine would be capable of producing power in the range of several hundred kilowatts to several megawatts, depending on the inflow velocity. This is the power that the turbine delivers to the axis, without any losses. Nevertheless, they provide a realistic order of magnitude indication of the expected power output at full scale.

5.3.2. Wave conditions

Table 5.5 summarizes the results obtained under wave conditions. The different waves conditions that were applied are provided in table 5.1. The listed rotational speeds are the average measured values. In the table, $\bar{Q}$ and $\bar{T}$ denote time-averaged torque and thrust, C_p the mean power coefficient, and A_Q and A_T the fluctuation amplitudes (half peak-to-peak) over the steady part of each record. The percentage column is obtained from:

$$\Delta T(\%) = 100 \cdot \, A_T/\bar{T}, \qquad \Delta Q(\%) = 100 \cdot \, A_Q/\bar{Q},$$

To compare the time averages ($\bar{Q}, \bar{T}$) in table 5.5 with steady state experimental averages, the values for this were; $Q = 3.71$ Nm, $T = 93.92$ N, and $C_p = 0.42$ at $U_\infty = 0.75$ m/s, and $Q = 1.12$ Nm, $T = 36.61$ N, and $C_p = 0.29$ at $U_\infty = 0.5$ m/s.

Table 5.5: Experimental results for wave conditions. $\bar{Q}, \bar{T}$ are time averages; A_Q, A_T are fluctuation amplitudes (half of peak-to-peak). Δ uses the steady-inflow baselines at the same U_∞.

U_∞ [m/s]	n [rpm]	λ [m]	a [m]	$\bar{Q}$ [Nm]	$\bar{T}$ [N]	C_p [–]	A_T [N]	ΔT [%]	A_Q [Nm]	ΔQ [%]
0.75	96.69	2.00	0.024	3.75	94.99	0.42	5.47	5.8	0.39	10.4
0.75	96.68	2.00	0.046	3.71	95.11	0.42	14.15	14.9	1.07	28.7
0.75	96.66	2.01	0.064	3.88	96.46	0.43	22.38	23.2	1.70	43.7
0.75	96.66	4.00	0.021	3.77	95.67	0.42	17.25	18.0	1.39	36.8
0.75	96.66	3.99	0.040	3.98	97.01	0.45	34.08	35.1	2.62	65.7
0.75	96.68	5.89	0.020	3.89	95.85	0.44	28.35	29.6	2.14	55.2
0.50	64.34	2.00	0.024	1.12	36.32	0.28	5.37	14.8	0.43	38.1
0.50	64.34	2.00	0.046	1.18	36.69	0.30	10.82	22.3	0.63	53.4
0.50	64.34	2.00	0.064	1.18	36.84	0.30	10.39	29.4	0.83	70.1
0.50	64.37	4.00	0.021	1.15	36.40	0.29	10.39	28.5	0.78	67.7
0.50	64.36	3.99	0.040	1.25	37.24	0.31	12.78	50.3	1.40	112.4
0.50	64.37	4.03	0.045	1.46	38.53	0.37	30.51	79.2	2.21	151.0
0.50	64.36	5.89	0.020	1.22	36.90	0.31	15.84	42.9	1.17	96.0
0.50	64.36	5.89	0.041	1.50	38.56	0.38	30.46	79.0	2.22	148.4

The table confirms the expectation of the literature that average performance values barely change under regular waves: $\bar{Q}$, $\bar{T}$, and C_p remain close to the corresponding steady-inflow values at the same U_∞. The only real discrepancies for the mean values appear in the three cases where the change in torque exceeds 100%. In these cases, the turbine briefly entered motor mode rather than generator mode, as shown in figure 5.12, where negative torque values indicate generator operation. Consequently, the corresponding C_p values are not representative. For all other cases, the averaged performance values remain reliable.

However, the fluctuations can become severe for certain waves. Fluctuation amplitudes grow with wave amplitude and are larger for longer waves at comparable steepness. For example: at $U_\infty = 0.75$ m/s, increasing A_ω from 0.024 to 0.064 m at $\lambda \approx 2$ m raises A_T from 5.5 N to 22.4 N and A_Q from 0.39 to 1.70 Nm (i.e. $\Delta T \approx$ 6-23%, $\Delta Q \approx$ 10-44%). At $U_\infty = 0.50$ m/s the most severe cases yield $\Delta T \approx 80\%$ and $\Delta Q > 100\%$.

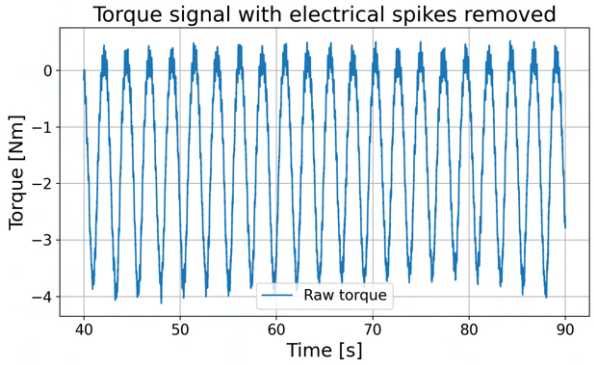

Figure 5.12: Torque signal entering motor mode for waves with $\lambda = 5.89$ m, $A_\omega = 0.120$ m.

The amplitudes A_T and A_Q in the table were calculated as the average amplitude from the maximum and minimum values observed (see figure 5.6a). Interestingly, the torque fluctuations were approximately twice as large as the thrust fluctuations. This provides valuable insight for future experiments in waves, as it quantifies the type of unsteady loads that can be expected on the turbine.

One final observation is that in the most extreme cases the efficiency, as expressed by C_p, increases slightly. A plausible explanation is that the strongly unsteady inflow promotes earlier transition to turbulence in the boundary layer, effectively increasing the local Reynolds number and improving performance.

Dynamic turbine response under wave loading

Figure 5.13 shows the measured time histories of shaft torque, thrust, and rotational speed under wave loading for a representative case. The signals clearly demonstrate that the passage of waves induces cyclic oscillations in all three quantities. The torque oscillates between approximately -0.5 and -2 Nm, while the thrust varies between 30 and 40 N. The rotational speed fluctuates around a mean of 64.5 rpm, with small amplitudes of about 0.5 rpm.

The oscillations occur at the wave frequency, with torque, thrust, and rotational speed all exhibiting the same fundamental frequency as the incoming waves. The phase relation with the wave elevation is evident in the left panels: the thrust, torque and rotational speed maxima occur close to the wave crests and troughs. This behavior is consistent with linear wave theory, where the horizontal orbital velocity is in phase with the free-surface elevation. The small lag observed in the measurements can be attributed to rotor inertia and flow dynamics, but overall the three quantities remain closely in phase with one another and with the wave elevation. The corresponding plots on the right further highlight these relations by showing the turbine response directly as a function of wave elevation. Elliptical loops are visible, where multiple values per wave elevation correspond to the increasing and decreasing wave height cases. The rotational speed also exhibits a consistent dependence on the wave elevation, underlining its sensitivity to the instantaneous flow velocity. Overall, these results confirm that the turbine response is strongly modulated by the passing waves, with wave-induced oscillations clearly having effect on the hydrodynamic loads.

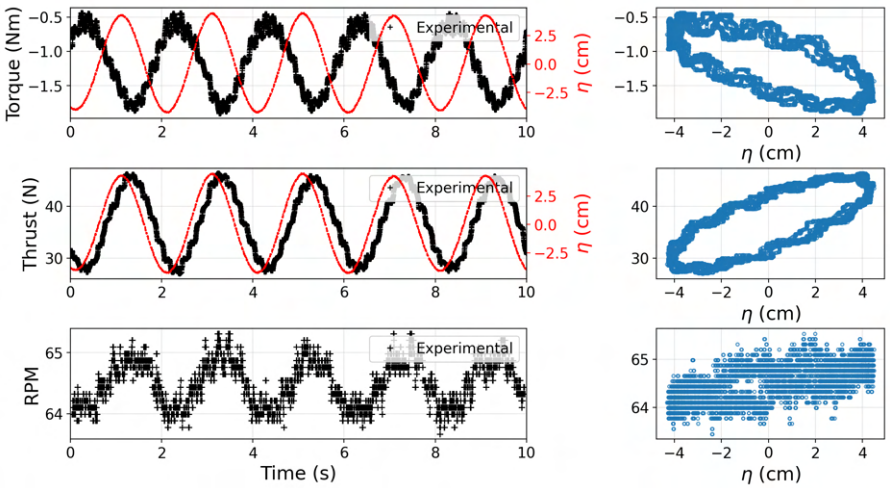

Figure 5.13: Left: time histories of the torque, thrust and rotational speed. Right: the torque, thrust and rotational speed as a function as a function of the encounter wave elevation, for $U_\infty = 0.5$ m/s, $\Omega \approx 64.5$ rpm $\lambda = 4$ m, and $\varepsilon = 0.02$.

While Figure 5.13 highlights the detailed response of the turbine to a single wave condition, figure 5.14 extends this view by comparing three different wave steepnesses to assess how the load amplitudes scale with wave intensity. In contrast to the maximum amplitudes reported in table 5.5, this figure shows the full dynamic response over time. To reduce measurement noise and highlight the underlying trends, the data were again processed using a median filter, resulting in the smooth solid lines shown.

The results demonstrate that both torque and thrust scale almost linearly with wave steepness, as visible from the systematic increase in amplitude across the three cases. Furthermore, torque and thrust exhibit nearly in-phase behavior with each other, though their signs are opposite due to the definition of negative torque in generator mode. A slight phase lag with respect to the wave motion can be observed here as well, like in figure 5.13. This lag may be attributed to a physical response delay of the turbine to the changing inflow velocity.

On the right-hand side of figure 5.14, the same quantities are shown after phase-averaging over the 10 s time window (solid lines), together with the corresponding standard deviations (dashed lines). This representation provides a clearer comparison of the trends across the different wave steepnesses.

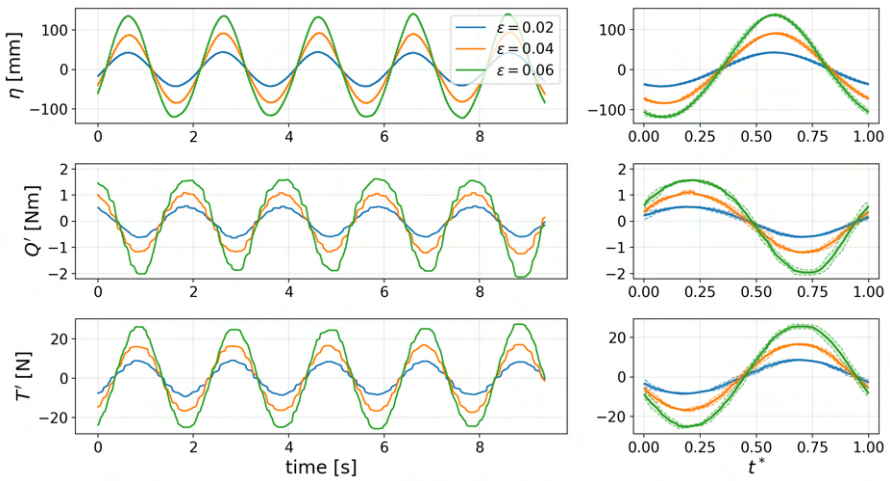

Figure 5.14: Wave coupled loads for $U_\infty = 0.5$ m/s, $\Omega \approx 64.5$ rpm, $\lambda = 4$ m, and ε =0.02, 0.04, 0.06. Left: time histories over a representative window of the free-surface elevation (η), torque fluctuation (Q') and thrust fluctuation (T'). Right: phase-averaged responses over 10 s time frame, as a function of the non-dimensional time.

Validation of wave load prediction method

The prediction method described in section 4.7 was applied to estimate turbine load fluctuations under wave conditions. The validation was performed for the $U_\infty = 0.75$ m/s cases, as these provided the most reliable experimental dataset and generally showed the best agreement.

One modification to the original method was introduced. In the described approach, the inflow velocity variation was determined at hub depth. When applied here, this resulted in underpredicted fluctuation amplitudes, so the method was too conservative. Improved results were obtained when the velocity was instead taken at a depth corresponding to half a blade radius above the center of the hub, which in this setup corresponds to $z = -0.44$ m. This adjustment provided significantly better agreement with the experimental data, although the physical reason for this improvement is not yet fully understood.

The procedure was as follows. First, the maximum inflow velocity was determined using the method from 4.7 at the adjusted depth. This velocity was then used as input in QBlade to simulate turbine performance at the corresponding operational point of approximately $n = 96.7$ rpm. The resulting thrust and torque values were compared to the steady inflow predictions at $U_\infty = 0.75$ m/s, yielding an amplitude for each load. This amplitude was subsequently expressed as a percentage of the mean values, providing the predicted relative change in torque and thrust.

The results of this procedure are summarized in table 5.6. The predicted percentage changes are generally in good agreement with the experimental measurements, supporting the validity of the method as a first-order estimation tool. However, the method is not straightforward to apply, as it it not possible to apply wave conditions in QBlade directly, and its improved accuracy at $z = -0.44$ m lacks a clear theoretical explanation. It is also only able to provide information for certain conditions rather than an entire curve, which makes it only suitable for predicting maximum forces. For future studies, the experimental results obtained here are recommended as a more reliable reference for predicting turbine load fluctuations under wave conditions.

Table 5.6: Wave cases at $U_\infty = 0.75$ m/s: comparison of fluctuation metrics between experiment and BEMT.

λ [m]	A_ω (m)	A_T Exp [N]	A_T BEMT [N]	A_Q Exp [Nm]	A_Q BEMT [Nm]
2.00	0.024	5.47	7.03	0.39	0.55
2.00	0.046	14.15	13.41	1.07	1.06
2.01	0.064	22.38	19.68	1.70	1.66
4.00	0.021	17.25	17.60	1.39	1.44
3.99	0.040	34.08	34.92	2.62	3.16
5.89	0.020	28.35	25.87	2.14	2.27

5.3.3. Tip deflection

A final point of interest from the experiments is the tip deflection of the blades. The bending of the tips was clearly visible by eye and became especially pronounced at higher inflow velocities and rotational speeds. The backwards bending changes the local angle of attack and can thereby influence turbine performance.

To estimate the magnitude of the tip deflection, a visual method was employed using a fixed camera placed above the turbine. Photographs were taken at the highest tip-speed ratios for the three flow conditions, where the effect is most noticeable. These photographs were then overlaid, as shown in figure 5.7, to visualize the relative displacement of the blade tip. A ruler was used to determine the displacement relative to the stationary ($U_\infty = 0$ m/s) case. The scaling of the images was obtained from the known hub length, after which the approximate tip deflections were measured. The resulting values are reported in table 5.7. The values are rounded to integers, as it is not possible to get higher accuracy from the photographs.

As seen in table 5.7, the tip deflections determined from the photographs are substantially larger than those obtained in the earlier point load experiments (see section 4.8). While the trend with increasing thrust is consistent, the tip deflections from the photographic measurements are approximately three times higher than the point load predictions. Several factors may explain this discrepancy. First, the photographic method involves visual approximation through water, possibly under a small angle, which

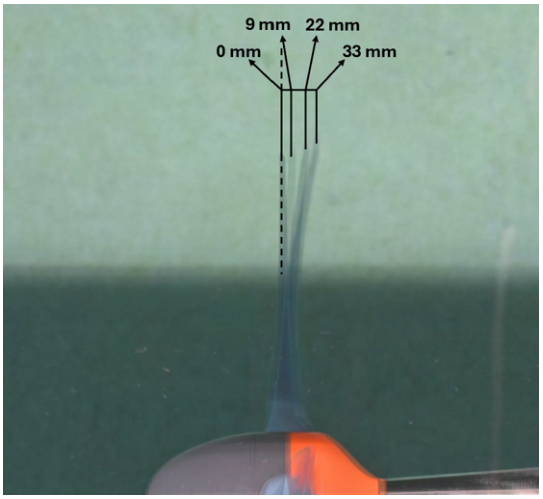

Figure 5.15: Tip deflection photos for TSR 7 at 0 m/s, 0.5 m/s, 0.75 m/s and 0.9 m/s

introduces refraction and measurement uncertainty. Second, in the static point load experiments, the load was applied at an estimated equivalent point (based on BEMT), coincidentally corresponding to the tip of the 6mm carbon rod. This location may not accurately represent the distributed loading experienced by the blade in water. In reality, the tip section of the blade experiences the highest hydrodynamic loading and is also structurally the weakest region, which makes it far more susceptible to bending. The point-load method therefore likely underestimated the effective tip deflection by not fully capturing this localized deformation.

Table 5.7: Comparison of predicted and experimental blade tip deflections.

U_∞ (m/s)	Rot. speed (rpm)	Thrust (N)	Point load (mm)	Hydrodynamic load (mm)
0.50	90.3	46	3	9
0.75	135.5	102	6	22
0.90	162.6	148	8	33

5.4. Discussion and key findings

The experimental results provide valuable insights into the performance and limitations of the model-scale turbine, as well as the predictive capability of BEMT simulations. While the general agreement between experiments and predictions is encouraging, several important observations and limitations can be drawn.

Predictive accuracy of BEMT at different Reynolds numbers

At Reynolds numbers below approximately $Re \approx 1.1 \times 10^5$, BEMT predictions based on XFOIL polars systematically overpredict the performance. This limitation originates not from BEMT itself, but from the underlying polar data. At low Reynolds numbers, laminar boundary layers separate easily under adverse pressure gradients, forming laminar separation bubbles whose size and reattachment behavior are highly sensitive and difficult to predict. XFOIL's transition and boundary-layer models tend to assume too much attachment in this regime, leading to optimistic lift and drag estimates (Chen et al. 2008). Above this threshold, where turbulent boundary layers dominate, predictions and experiments show much closer agreement.

The value $Re \approx 1.1 \times 10^5$ identified here should be interpreted as an indicative transition for this specific blade geometry, surface finish, and facility turbulence level, rather than a universal cutoff. The current foil NACA 63-8XX is not necessarily designed for low Reynolds number applications, mainly for high lift (see section 4.6.1). Using another foil shape could bring the transition point down. Increased surface roughness or deliberate transition trips can possibly move the effective threshold to higher Re by promoting earlier transition.

The results confirm that the turbine approaches, but does not yet fully reach, Reynolds independence. While the $U_\infty = 0.75$ m/s and $U_\infty = 0.9$ m/s cases show relatively small differences in C_p and C_t, the $U_\infty = 0.5$ m/s case deviates significantly. This highlights the importance of considering Reynolds dependence when interpreting small-scale experimental results and extrapolating to full-scale performance.

Efficiency and comparison with literature

Despite the limitations described above, the measured efficiency of the turbine is relatively high compared to earlier studies. The maximum C_p values obtained are close to 0.44, even with the presence of significant blade bending, geometric tolerances from 3D printing, and the use of modified foils (with truncated trailing edges for manufacturability). In contrast, many studies report substantially lower optimal C_p values (see 1.18).

An important observation is that C_p in this Reynolds number range is strongly dependent on inflow velocity, which was not fully appreciated in the initial design phase. This sensitivity may explain why some previous studies reported relatively low efficiencies, depending on their tested velocity range and blade dimensions. For future experiments, a trade-off between blade efficiency and structural stiffness may be necessary. Reducing bending would require thicker foils and the use of a larger carbon rod, or even different blade materials. The present 4 mm carbon rod provided limited additional stiffness, as indicated by the discrepancy between static point-load tests and dynamic deflections during operation.

Influence of waves

The experiments under regular wave conditions confirmed the general prediction from literature that the averaged thrust, torque, and C_p values remained close to steady inflow conditions. The turbine, however, experienced strong unsteady loads, with relative torque fluctuations roughly twice as large as thrust fluctuations. This result is of practical importance, as it indicates that unsteady torque loading may pose the more critical fatigue design challenge in real sea conditions. For the most extreme cases, torque fluctuations exceeded 100% of the mean value, even briefly driving the turbine into motor mode. These conditions are not captured by BEMT-based predictions, highlighting the need for improved unsteady modeling tools.

Tip deflection and structural flexibility

A key structural observation is the significant tip deflection of the blades under load. The photographic method revealed tip deflections up to 33 mm at $U_\infty = 0.9$ m/s, approximately three times higher than predicted by static point load experiments. While measurement uncertainties likely contributed, a more important explanation is the difference in loading distribution: in static tests, the equivalent load was applied at an estimated point, while in water the hydrodynamic loading acts continuously along the blade span. The structural material properties are not uniform along the blade as the tip section is the weakest part and therefore experiences disproportionately large bending.

Such deformation directly affects the local angle of attack and thus turbine performance. Small changes in twist due to bending can shift the operating point, potentially explaining why the optimal TSR predicted by QBlade was consistently lower than observed experimentally. Future work should therefore include more accurate measurements of blade deformation and consider fluid-structure interaction effects to better capture the coupling between hydrodynamics, blade flexibility and the effect is has on the performance of the turbine.

Evaluation of the gondola setup

Overall, the gondola measurement setup performed well. The proximity of the torque and thrust sensor to the turbine minimized structural compliance and measurement error, ensuring reliable load measurements. However, two main limitations were identified.

First, at rotational speeds below approximately 50 rpm, it became increasingly difficult to maintain stable control of the turbine speed. This restricted testing at the lowest TSR values. Second, the torque limit of the motor setup was reached at approximately 6.8 Nm. While sufficient for the present experiments, this limit could be exceeded relatively easily with slightly larger turbines or higher inflow velocities. Although the load sensor itself can withstand higher loads, the limiting component in the drivetrain requires further investigation.

If this limitation cannot be resolved, a more advanced gondola design, such as proposed in chapter 3, may be preferable for future experiments. In addition, a geared motor may provide improved speed control at lower rpm. The nacelle design is also flexible in adjusting nacelle length, hub shape, strut shape and length, and removing all inner parts like the motor or sensor.

Implications for full-scale performance

Extrapolation of the results to full scale, using Froude scaling and assuming $C_p = 0.441$, indicated that the 16 m turbine would be capable of producing several hundred kilowatts at moderate currents ($U_\infty \approx 2.3$ m/s) and over 3 MW at higher inflow speeds ($U_\infty \approx 4.2$ m/s). Although the extrapolation neglects different kinds of losses, it provides a useful order of magnitude indication of the achievable power levels.

Key findings

In summary, the main findings of this experiments are:

- BEMT predictions are reliable above $Re \approx 1.1 \times 10^5$, but systematically overpredict below this threshold, consistent with limitations of XFOIL polars in the laminar regime.
- The turbine efficiency is relatively high ($C_p \approx 0.44$), even with blade bending and 3D printing constraints, showing potential for further optimization.
- Under wave conditions, mean power remains largely unchanged while unsteady loads increase substantially, with torque fluctuations over 100%.
- Blade tip deflection is significantly larger in operation than predicted by static tests, highlighting the need to account for structural flexibility.
- The gondola performed well overall, but is limited by torque capacity and low-speed control.
- Scaling to 16 m diameter suggests power outputs up to several megawatts at realistic inflow velocities.

6

Conclusion and future research

This thesis set out to answer the main research question:

How can a model-scale hydrokinetic turbine be designed, constructed, and tested to ensure structural integrity, cost-effectiveness, and compatibility with existing experimental studies while enabling accurate performance evaluation for future research?

To address this overarching question, the work was structured around four sub-questions, each guiding a specific design or evaluation stage.

Performance prediction using actuator disc theory and BEMT

Actuator disc theory and BEMT proved to be practical tools for predicting turbine performance during the design phase. While the models simplify the physics and neglect certain low-Reynolds effects, they still captured the main performance trends and provided reliable estimates of thrust and torque across the operating range. This predictive capability was crucial for sizing the drivetrain components. The comparison with experiments also highlights the boundaries of the method's validity, underlining its value as a first-order design tool that should ultimately be complemented with experimental validation.

Nacelle design

The nacelle was designed conceptually to house both the motor and the torque/thrust sensor in a compact and modular way. While financial limitations meant that it could not be built for this project, the design itself proved to be technically sound and flexible enough to be scaled or adapted in the future. For the present experiments, the existing TU Delft gondola was used instead. This provided a practical and reliable test setup, while also demonstrating that the nacelle design can be implemented in future campaigns once resources allow.

Hub and blade design

A modular hub system was developed that allows for easily exchangeable blades and adjustable pitch settings. The blades were designed using BEMT optimization methods and manufactured using 3D printing, which offered a cost-effective and flexible method for rapid prototyping. Several design refinements were made to improve printability and structural robustness, including thickened trailing edges, increased infill, and the integration of a carbon reinforcement rod. Static tests confirmed that the blades withstood loads of up to 441 N equivalent thrust load, well beyond the expected operating range without failure. Together, these design steps provided a rotor that balances hydrodynamic efficiency, manufacturability, robustness, and cost-effectiveness, while remaining compatible with the experimental setup.

Experimental validation of turbine performance and structural integrity

The turbine was tested under both steady and wave conditions in the towing tank. In steady inflow, the measured thrust and torque showed good agreement with BEMT predictions, with a maximum power coefficient of $C_p \approx 0.44$. These values confirm that the chosen blade geometry and hub connection delivered the expected performance despite the constraints of 3D printing. During operation, however,

large blade tip deflections were observed of up to 33 mm, significantly exceeding those predicted by static tests (8 mm maximum). While the blades remained structurally sound, this demonstrated that deformation plays an important role in the turbine's dynamic response and should be considered in future designs.

Under wave forcing, the average power output remained comparable to steady inflow, but the loading became highly unsteady. Both torque and thrust were strongly influenced by the presence of waves, showing clear cyclic variations at the wave frequency. The relative torque oscillations were roughly twice as large as those in thrust, making torque the more sensitive of the two load components. The gondola setup made it possible to capture these dynamics reliably, although its limited torque capacity and difficult control at low speeds restricted the operating range that could be explored.

6.0.1. Answer to the main research question

This thesis has shown that it is possible to design, build, and experimentally validate a model-scale hydrokinetic turbine that satisfies the main requirements of structural integrity, cost-effectiveness, and compatibility with existing research. The use of BEMT and actuator disc theory provided a reliable foundation for the design, giving accurate results when predicting operating loads once the turbine reached sufficiently high Reynolds numbers. A modular nacelle and hub concept was developed that can be scaled and adapted for future campaigns, while the decision to 3D-print the blades allowed rapid prototyping, while providing relatively high stiffness.

The experimental campaign confirmed the feasibility of this approach. The turbine with a diameter of 0.74 m reached a peak power coefficient of $C_p = 0.44$, placing its performance comparable to other model-scale turbines in the literature. The blades withstood forces well beyond the expected range, and the hub connection proved reliable. At the same time, the experiments highlighted important dynamic phenomena: large tip deflections that exceeded static predictions, and strong unsteady loading under waves.

Taken together, these outcomes demonstrate that the design was robust, affordable, and consistent with prior research, while also revealing the limitations and challenges that accompany small-scale hydrokinetic experiments with 3D printed blades. All design requirements defined in chapter 1.6, including structural integrity, performance, and compatibility with the experimental setup, were successfully met, confirming that the turbine fulfilled its intended objectives. Most importantly, the work has delivered a functioning turbine that provides a practical and versatile platform for future studies into wave environments.

6.0.2. Future research

Several opportunities for further research arise directly from the work presented in this thesis. As discussed in chapter 5, BEMT predictions became reliable once the turbine reached Reynolds numbers above $Re \approx 1.1 \cdot 10^5$. To confirm that this marks the true transition from laminar to turbulent behavior, further tests are needed around this threshold. In addition, new experiments at higher inflow speeds (above 0.9 m/s) should be performed to verify whether Reynolds independence is fully reached for this turbine. In parallel, the wave model introduced in chapter 5 requires further validation. The choice of reference depth for orbital velocities, although effective in matching experimental trends, is still empirical and should be tested under a wider range of conditions and against theoretical predictions. A logical next step would be to integrate the wave model directly into the BEMT framework, so that time-resolved performance curves under wave forcing can be predicted and compared to experiments.

To better understand the effect of transition, future tests could make use of small turbulators placed spanwise near the leading edge. These force the boundary layer to become turbulent earlier along the blade. By varying the position and size of the turbulators, and matching the same forced-transition settings in QBlade, the influence on low Reynolds polars and BEMT predictions can be studied. Another complementary approach would be to repeat the tests with alternative blade designs, allowing the Reynolds effect at low Reynolds numbers to be investigated independently of the current blade geometry. In this way, it becomes possible to separate model limitations from surface-condition effects and to refine the Reynolds threshold for this turbine. To ensure consistency between the physical prototype and the BEMT predictions, the final geometry of the 3D-printed blades should be validated against the numerical model.

The nacelle was developed at a conceptual level but not manufactured (chapter 3). Building the nacelle as designed would allow full integration of the drivetrain and sensors, reducing reliance on the gondola. At the same time, improvements in drivetrain torque capacity and low-speed control by the use of a gearbox would expand the accessible operating range, particularly for low rotational speed conditions and high-load scenarios. It also provides a more modular design than the gondola, with possibilities to adjust the length of the nacelle and the shape of the strut. This would then allow testing at larger depths as well.

In chapter 4, static tests showed that the blades withstood loads well beyond the expected operating range. During the experiments in chapter 5, however, large tip deflections were observed, exceeding those predicted by static analysis. Future work should therefore focus on quantifying these deformations more accurately. Optical tracking systems for example would allow blade deflection to be measured in real time, enabling a better understanding of fluid-structure interaction effects and quantify the actual blade deflection effects. The use of 3D printing enabled rapid and cost-effective blade production, but it also introduced geometric constraints and large deflections under load. Future work could also explore alternative manufacturing methods, such as composite layups or reinforced printing techniques, to achieve higher stiffness and durability.

References

Abbott, I. H. A. and A. E. Von Doenhoff (1959). *Theory of Wing Sections: Including a Summary of Airfoil Data*. Dover Publications.

Abutunis, A. and V. G. Menta (Apr. 1, 2022). "Comprehensive Parametric Study of Blockage Effect on the Performance of Horizontal Axis Hydrokinetic Turbines". In: *Energies* 15.7, p. 2585. DOI: 10.3390/en15072585.

Adcock, T. A., S. Draper, R. H. Willden, and C. R. Vogel (Oct. 2, 2020). "The Fluid Mechanics of Tidal Stream Energy Conversion". In: *Annual Review of Fluid Mechanics* 53.1, pp. 287–310. DOI: 10.1146/annurev-fluid-010719-060207.

Adeyeye, K. A., N. Ijumba, and J. Colton (June 1, 2021). "The Effect of the Number of Blades on the Efficiency of A Wind Turbine". In: *IOP Conference Series Earth and Environmental Science* 801.1, p. 012020. DOI: 10.1088/1755-1315/801/1/012020.

Ahmed, M. R. (Mar. 22, 2012). "Blade sections for wind turbine and tidal current turbine applications-current status and future challenges". In: *International Journal of Energy Research* 36.7, pp. 829–844. DOI: 10.1002/er.2912.

Alamian, R., R. Shafaghat, H. A. Amiri, and M. S. Shadloo (Aug. 2020). "Experimental assessment of a 100 W prototype horizontal axis tidal turbine by towing tank tests". In: *Renewable Energy* 155, pp. 172–180. ISSN: 09601481. DOI: 10.1016/j.renene.2020.03.139.

Allmark, M., R. Ellis, C. Lloyd, S. Ordonez-Sanchez, K. Johannesen, C. Byrne, C. Johnstone, T. O'Doherty, and A. Mason-Jones (Aug. 2020). "The development, design and characterisation of a scale model Horizontal Axis Tidal Turbine for dynamic load quantification". In: *Renewable Energy* 156, pp. 913–930. ISSN: 09601481. DOI: 10.1016/j.renene.2020.04.060.

Applied Measurements Ltd. (2020). *Torque Sensor in Tidal Turbine Testing*. Accessed: 2025-06-22. URL: https://appmeas.co.uk/blog/tidal-turbine-testing/.

Badshah, M., S. Badshah, and S. Jan (2017). "Hydrodynamic design of tidal current turbine and the effect of solidity on performance". In: *Journal of Engineering and Applied Sciences* 36.2, pp. 45–54. ISSN: 1023-862X.

Bahaj, A., A. Molland, J. Chaplin, and W. Batten (Mar. 2007). "Power and thrust measurements of marine current turbines under various hydrodynamic flow conditions in a cavitation tunnel and a towing tank". In: *Renewable Energy* 32.3, pp. 407–426. ISSN: 09601481. DOI: 10.1016/j.renene.2006.01.012.

Barber, R. B., C. S. Hill, P. F. Babuska, R. Wiebe, A. Aliseda, and M. R. Motley (Feb. 13, 2017). "Flume-scale testing of an adaptive pitch marine hydrokinetic turbine". In: *Composite Structures* 168, pp. 465–473. DOI: 10.1016/j.compstruct.2017.02.051.

Batten, W., A. Bahaj, A. Molland, and J. Chaplin (Oct. 27, 2005). "Hydrodynamics of marine current turbines". In: *Renewable Energy* 31.2, pp. 249–256. DOI: 10.1016/j.renene.2005.08.020.

Batu, T. and H. G. Lemu (2020). "Comparative Study of the Effect of Chord Length Computation Methods in Design of Wind Turbine Blade". In: *Lecture Notes in Electrical Engineering: IWAMA 2019*. Ed. by Y. W. et al. Singapore: Springer Nature Singapore Pte Ltd., pp. 1–10. DOI: 10.1007/978-981-15-2341-0_14.

Boatto, U., P. A. Bonnet, F. Avallone, and D. Ragni (2023). "Assessment of Blade Element Momentum Theory-based engineering models for wind turbine rotors under uniform steady inflow". In: *Renewable Energy* 214, pp. 307–317. DOI: 10.1016/j.renene.2023.04.050.

Brasil Junior, A. C. P., R. C. F. Mendes, T. Wirrig, R. Noguera, and T. F. Oliveira (May 16, 2019). "On the design of propeller hydrokinetic turbines: the effect of the number of blades". In: *Journal of the Brazilian Society of Mechanical Sciences and Engineering* 41.6. DOI: 10.1007/s40430-019-1753-4.

Budynas, R. G. and J. K. Nisbett (2015). *Shigley's Mechanical Engineering Design*. 10th ed. New York: McGraw-Hill Education.

Burton, T., D. Sharpe, N. Jenkins, and E. Bossanyi (2011). *Wind Energy Handbook*. 2nd ed. John Wiley & Sons.

Byrne, G., T. Persoons, and W. Kingston (Jan. 1, 2019). "Experimental validation of lift and drag forces on an asymmetrical hydrofoil for seafloor anchoring applications". In: *Journal of Ocean and Climate Science Technology and Impacts* 9. DOI: 10.1177/1759313118811979.

Chamorro, L., C. Hill, S. Morton, C. Ellis, R. Arndt, and F. Sotiropoulos (Feb. 10, 2013a). "On the interaction between a turbulent open channel flow and an axial-flow turbine". In: *Journal of Fluid Mechanics* 716, pp. 658–670. ISSN: 0022-1120, 1469-7645. DOI: 10.1017/jfm.2012.571.

Chamorro, L., C. Hill, V. Neary, B. Gunawan, R. Arndt, and F. Sotiropoulos (May 2015). "Effects of energetic coherent motions on the power and wake of an axial-flow turbine". In: *Physics of Fluids* 27.5, p. 055104. ISSN: 1070-6631, 1089-7666. DOI: 10.1063/1.4921264.

Chamorro, L., D. Troolin, S. Lee, R. Arndt, and F. Sotiropoulos (Jan. 2013b). "Three-dimensional flow visualization in the wake of a miniature axial-flow hydrokinetic turbine". In: *Experiments in Fluids* 54.2. DOI: 10.1007/s00348-013-1459-9.

Chen, L., P. A. J. Bonar, C. R. Vogel, and T. A. A. Adcock (2019). "A note on the tuning of tidal turbines in channels". In: *Journal of Ocean Engineering and Marine Energy* 5.1, pp. 85–98. ISSN: 2198-6444, 2198-6452. DOI: 10.1007/s40722-019-00132-z.

Chen, L. and W. Lam (2015). "A review of survivability and remedial actions of tidal current turbines". In: *Renewable and Sustainable Energy Reviews* 43, pp. 891–900. DOI: 10.1016/j.rser.2014.11.071.

Chen, W. and L. P. Bernal (2008). "Design and Performance of Low Reynolds Number Airfoils for Solar-Powered Flight". In: *46th AIAA Aerospace Sciences Meeting and Exhibit*. American Institute of Aeronautics and Astronautics. Reno, Nevada. DOI: 10.2514/6.2008-316.

Chen, Y., B. Lin, J. Lin, and S. Wang (June 2017a). "Experimental study of wake structure behind a horizontal axis tidal stream turbine". In: *Applied Energy* 196, pp. 82–96. ISSN: 03062619. DOI: 10.1016/j.apenergy.2017.03.126.

Chen, Y., B. Lin, J. Lin, and S. Wang (June 2017b). "Experimental study of wake structure behind a horizontal axis tidal stream turbine". In: *Applied Energy* 196, pp. 82–96. ISSN: 03062619. DOI: 10.1016/j.apenergy.2017.03.126.

Chihaia, R.-A., G. Oprina, S. Nicolaie, A. El-Leathey, C. Babutanu, and A. Nedelcu (2016). "Assessing the Blade Chord Length Influence on the Efficiency of a Horizontal Axis Hydrokinetic Turbine". In: *Proceedings of the 2016 International Conference on Hydraulics and Pneumatics (HERVEX)*. Fluidas. Baile Govora, Romania, pp. 290–297.

Coleman, H. W. and W. G. Steele (2018). *Experimentation, Validation, and Uncertainty Analysis for Engineers*. 4th. Wiley.

Dassault Systèmes (2025). *SolidWorks Simulation*. Version 2025, https://www.solidworks.com.

De Jesus Henriques, T., S. Tedds, A. Botsari, G. Najafian, T. Hedges, C. Sutcliffe, I. Owen, and R. Poole (Dec. 2014). "The effects of wave–current interaction on the performance of a model horizontal axis tidal turbine". In: *International Journal of Marine Energy* 8, pp. 17–35. ISSN: 22141669. DOI: 10.1016/j.ijome.2014.10.002.

Dean, R. G. and R. A. Dalrymple (1991). *Water Wave Mechanics for Engineers and Scientists*. Vol. 2. Advanced Series on Ocean Engineering. Singapore: World Scientific Publishing.

Delafin, P., T. Nishino, L. Wang, and A. Kolios (Sept. 1, 2016). "Effect of the number of blades and solidity on the performance of a vertical axis wind turbine". In: *Journal of Physics Conference Series* 753, p. 022033. DOI: 10.1088/1742-6596/753/2/022033.

Doman, D. A., R. E. Murray, M. J. Pegg, K. Gracie, C. M. Johnstone, and T. Nevalainen (Sept. 2015). "Tow-tank testing of a 1/20th scale horizontal axis tidal turbine with uncertainty analysis". In: *International Journal of Marine Energy* 11, pp. 105–119. ISSN: 22141669. DOI: 10.1016/j.ijome.2015.06.003.

Draycott, S., J. Steynor, A. Nambiar, B. Sellar, and V. Venugopal (May 2019). "Experimental assessment of tidal turbine loading from irregular waves over a tidal cycle". In: *Journal of Ocean Engineering and Marine Energy* 5.2, pp. 173–187. ISSN: 2198-6444, 2198-6452. DOI: 10.1007/s40722-019-00136-9.

Drela, M. (1989). "XFOIL: An Analysis and Design System for Low Reynolds Number Airfoils". In: *Conference on Low Reynolds Number Airfoil Aerodynamics*. Notre Dame, Indiana, USA.

Drela, M. and M. B. Giles (1987). “Viscous-inviscid analysis of transonic and low Reynolds number airfoils”. In: *AIAA Journal* 25.10, pp. 1347–1355. DOI: 10.2514/3.9789.

Ellis, R., M. Allmark, T. O’Doherty, A. Mason-Jones, S. Ordonez-Sanchez, K. Johannesen, and C. Johnstone (2018). “Design Process for a Scale Horizontal Axis Tidal Turbine Blade”. In: *Proceedings of the 4th Asian Wave and Tidal Energy Conference (AWTEC)*. Taipei, Taiwan. URL: https://www.researchgate.net/publication/328432584_Design_Process_for_a_Scale_Horizontal_Axis_Tidal_Turbine_Blade.

Encarnacion, J. I., C. Johnstone, and S. Ordonez-Sanchez (June 27, 2019). “Design of a Horizontal Axis Tidal Turbine for Less Energetic Current Velocity Profiles”. In: *Journal of Marine Science and Engineering* 7.7, p. 197. DOI: 10.3390/jmse7070197.

EurObserv’ER (Sept. 2022). *Ocean Energy Barometer*. Accessed: 2024-03-14. EurObserv’ER. URL: https://www.eurobserv-er.org/ocean-energy-barometer-2022/.

Farhoody, A., R. Shafaghat, and B. Alizadeh Kharkeshi (Sept. 2023). “An experimental study to investigate the effect of pitch angle and wave characteristics on the performance of a horizontal axis tidal turbine”. In: *Applied Ocean Research* 138, p. 103646. ISSN: 01411187. DOI: 10.1016/j.apor.2023.103646.

Faudot, C. and O. G. Dahlhaug (2012). “Prediction of Wave Loads on Tidal Turbine Blades”. In: *Energy Procedia* 20, pp. 116–133. ISSN: 18766102. DOI: 10.1016/j.egypro.2012.03.014.

Ferraiuolo, R., A. Gharib-Yosry, A. Fernández-Jiménez, R. Espina-Valdés, E. Álvarez-Álvarez, G. Del Giudice, and M. Giugni (Nov. 1, 2022). “Design and Experimental Performance Characterization of a Three-Blade Horizontal-Axis Hydrokinetic Water Turbine in a Low-Velocity Channel”. In: *EWaS5 International Conference: “Water Security and Safety Management: Emerging Threats or New Challenges? Moving from Therapy and Restoration to Prognosis and Prevention”* EWaS International Conference. MDPI, p. 62. DOI: 10.3390/environsciproc2022021062. (Visited on 11/28/2024).

Ferraiuolo, R., F. Pugliese, E. Álvarez Álvarez, A. G. Yosry, M. Giugni, and G. Del Giudice (Dec. 2024). “Experimental and numerical investigation of a three-blade horizontal axis hydrokinetic water turbine (HAHWT) in high blockage conditions”. In: *Renewable Energy* 237, p. 121640. ISSN: 09601481. DOI: 10.1016/j.renene.2024.121640.

Galloway, P. W., L. E. Myers, and A. S. Bahaj (Oct. 6–8, 2010). “Studies of a scale tidal turbine in close proximity to waves”. In: *Proceedings of the Third International Conference and Exhibition on Ocean Energy (ICOE 2010)*. Bilbao, Spain. URL: https://eprints.soton.ac.uk/333950/.

Galloway, P. W., L. E. Myers, and A. S. Bahaj (Mar. 2014). “Quantifying wave and yaw effects on a scale tidal stream turbine”. In: *Renewable Energy* 63, pp. 297–307. ISSN: 09601481. DOI: 10.1016/j.renene.2013.09.030.

Gambuzza, S., P. Sunil, M. Felli, A. M. Young, R. Broglia, E. D. McCarthy, and I. M. Viola (Feb. 2025). “Power and thrust control by passive pitch for tidal turbines”. In: *Renewable Energy* 239, p. 121921. ISSN: 09601481. DOI: 10.1016/j.renene.2024.121921.

Garrett, C. and P. Cummins (Oct. 10, 2007). “The efficiency of a turbine in a tidal channel”. In: *Journal of Fluid Mechanics* 588, pp. 243–251. ISSN: 0022-1120, 1469-7645. DOI: 10.1017/S0022112007007781.

Gasch, R. and J. Twele (2012). *Wind Power Plants: Fundamentals, Design, Construction and Operation*. 2nd. Berlin, Heidelberg: Springer-Verlag Berlin Heidelberg. DOI: 10.1007/978-3-642-22938-1.

Gaurier, B., G. Germain, J. Facq, C. Johnstone, A. Grant, A. Day, E. Nixon, F. Di Felice, and M. Costanzo (Dec. 2015). “Tidal energy “Round Robin” tests comparisons between towing tank and circulating tank results”. In: *International Journal of Marine Energy* 12, pp. 87–109. ISSN: 22141669. DOI: 10.1016/j.ijome.2015.05.005.

Gaurier, B., P. Davies, A. Deuff, and G. Germain (Nov. 2013). “Flume tank characterization of marine current turbine blade behaviour under current and wave loading”. In: *Renewable Energy* 59, pp. 1–12. ISSN: 09601481. DOI: 10.1016/j.renene.2013.02.026.

Genç, M. S., İ. Karasu, and H. H. Açıkel (2012). “An experimental study on aerodynamics of NACA2415 hydrofoil at low Reynolds numbers”. In: *Experimental Thermal and Fluid Science* 39, pp. 252–264. DOI: 10.1016/j.expthermflusci.2012.01.029.

Gigue‘re, P. and M. S. Selig (May 1, 1998). “New Airfoils for Small Horizontal Axis Wind Turbines”. In: *Journal of Solar Energy Engineering* 120.2, pp. 108–114. DOI: 10.1115/1.2888052.

Glauert, H. (1935). “Airplane Propellers”. In: *Aerodynamic Theory*. Ed. by W. F. Durand. Vol. IV. Aerodynamic Theory. Berlin, Heidelberg: Julius Springer, pp. 169–360.

Gordon, F., K. Grattan, H. Jeffrey, A. Brito e Melo, E. Buck, and Ocean Energy Systems (Sept. 23, 2023). *Ocean Energy and Net Zero: An International Roadmap to Develop 300GW of Ocean Energy by 2050*.

Greenwood, C., A. Vogler, V. Venugopal, Marine Energy Research Group, Institute for Energy Systems, University of the Highlands and Islands, and The University of Edinburgh (Feb. 19, 2019). “On the Variation of Turbulence in a High-Velocity Tidal Channel”. In: *Energies* 12, pp. 672–. DOI: 10.3390/en12040672.

Grogan, D., S. Leen, C. Kennedy, and C. Ó. Brádaigh (Feb. 24, 2013). “Design of composite tidal turbine blades”. In: *Renewable Energy* 57, pp. 151–162. DOI: 10.1016/j.renene.2013.01.021.

Guo, X., J. Yang, Z. Gao, T. Moan, and H. Lu (Mar. 2018). “The surface wave effects on the performance and the loading of a tidal turbine”. In: *Ocean Engineering* 156, pp. 120–134. ISSN: 00298018. DOI: 10.1016/j.oceaneng.2018.02.033.

Gupta, M. K. and P. Subbarao (Feb. 1, 2020). “Development of a semi-analytical model to select a suitable airfoil section for blades of horizontal axis hydrokinetic turbine”. In: *Energy Reports* 6, pp. 32–37. DOI: 10.1016/j.egyr.2019.08.014.

Hibbeler, R. C. (2016). *Engineering Mechanics: Dynamics*. 14th. Harlow, England: Pearson Education.

Hibbeler, R. C. (2018). *Mechanics of Materials*. 10th ed. Harlow, England: Pearson Education.

Horwitz, R. M. and A. E. Hay (Mar. 21, 2017). “Turbulence dissipation rates from horizontal velocity profiles at mid-depth in fast tidal flows”. In: *Renewable Energy* 114, pp. 283–296. DOI: 10.1016/j.renene.2017.03.062.

Huang, B., B. Zhao, L. Wang, P. Wang, H. Zhao, P. Guo, S. Yang, and D. Wu (Jan. 2022). “The effects of heave motion on the performance of a floating counter-rotating type tidal turbine under wave-current interaction”. In: *Energy Conversion and Management* 252, p. 115093. ISSN: 01968904. DOI: 10.1016/j.enconman.2021.115093.

International Electrotechnical Commission (2013). *IEC 60529: Degrees of protection provided by enclosures (IP Code)*.

Jahanmiri, M. (2011). *Laminar Separation Bubble: Its Structure, Dynamics and Control*. Tech. rep. Research Report 2011:06. Chalmers University of Technology.

Jing, F., Y. Mei, Q. Lu, L. Yang, and B. Guo (Apr. 1, 2024). “Study on the performance of a floating horizontal-axis tidal turbine with pitch motion under wave–current interaction”. In: *Physics of Fluids* 36.4, p. 047122. ISSN: 1070-6631, 1089-7666. DOI: 10.1063/5.0206049.

Khan, M., M. Iqbal, and J. Quaicoe (June 27, 2007). “River current energy conversion systems: Progress, prospects and challenges”. In: *Renewable and Sustainable Energy Reviews* 12.8, pp. 2177–2193. DOI: 10.1016/j.rser.2007.04.016.

Khchine, Y. E. and M. Sriti (Jan. 1, 2018). “Improved Blade Element Momentum Theory (BEM) for predicting the aerodynamic performances of horizontal axis Wind turbine blade (HAWT)”. In: *Technische Mechanik* 38.2, pp. 191–202. DOI: 10.24352/ub.ovgu-2018-028.

Kinsey, T. and G. Dumas (Apr. 2017). “Impact of channel blockage on the performance of axial and cross-flow hydrokinetic turbines”. In: *Renewable Energy* 103, pp. 239–254. ISSN: 09601481. DOI: 10.1016/j.renene.2016.11.021.

Kolekar, N. and A. Banerjee (June 2015). “Performance characterization and placement of a marine hydrokinetic turbine in a tidal channel under boundary proximity and blockage effects”. In: *Applied Energy* 148, pp. 121–133. ISSN: 03062619. DOI: 10.1016/j.apenergy.2015.03.052.

Kumar, A. and R. Saini (2016). “Performance parameters of Savonius type hydrokinetic turbine – A Review”. In: *Renewable and Sustainable Energy Reviews* 64, pp. 289–310. DOI: 10.1016/j.rser.2016.06.005.

Lande-Sudall, D., S. Tolleifsen, K. Gravelsæter, H. Moen, and J. Bartl (Sept. 2, 2023). “Preliminary performance assessment from towing tank testing of a horizontal-axis turbine”. In: *Proceedings of the European Wave and Tidal Energy Conference* 15. ISSN: 2706-6940, 2706-6932. DOI: 10.36688/ewtec-2023-545.

Lemmon, E., M. McLinden, and D. Friend (2025). *Thermophysical Properties of Fluid Systems*. National Institute of Standards and Technology, retrieved 2025-08-13.

Lock, C. (1924). *Experiments to Verify the Independence of the Elements of an Airscrew Blade*. Technical Report No. 953. ARCR R&M.

Lust, E. E., L. Luznik, K. A. Flack, J. M. Walker, and M. C. Van Benthem (Dec. 2013). “The influence of surface gravity waves on marine current turbine performance”. In: *International Journal of Marine Energy* 3-4, pp. 27–40. ISSN: 22141669. DOI: 10.1016/j.ijome.2013.11.003.

Luznik, L., K. A. Flack, E. E. Lust, and K. Taylor (Oct. 2013). “The effect of surface waves on the performance characteristics of a model tidal turbine”. In: *Renewable Energy* 58, pp. 108–114. ISSN: 09601481. DOI: 10.1016/j.renene.2013.02.022.

Madsen, H. A., T. J. Larsen, G. Pirrung, A. Li, and F. Zahle (2020). “Implementation of the Blade Element Momentum Model on a Polar Grid and Its Aeroelastic Load Impact”. In: *Wind Energy Science* 5, pp. 1–27. DOI: 10.5194/wes-2019-53.

Manwell, J., J. McGowan, A. Rogers, DNV – Global Energy Concepts, and University of Massachusetts (2009). *Wind Energy Explained: Theory, Design, and Application*. Second. John Wiley & Sons Ltd.

Marten, D., J. Saverin, R. B. de Luna, and S. Perez-Becker (2024). *QBlade Documentation, Release 2.0.8*. Accessed: 2025-06-16. URL: https://docs.qblade.org.

Martinez, R. et al. (Apr. 14, 2021). “Tidal Energy Round Robin Tests: A Comparison of Flow Measurements and Turbine Loading”. In: *Journal of Marine Science and Engineering* 9.4, p. 425. ISSN: 2077-1312. DOI: 10.3390/jmse9040425.

Mason-Jones, A., D. O’Doherty, C. Morris, T. O’Doherty, C. Byrne, P. Prickett, R. Grosvenor, I. Owen, S. Tedds, and R. Poole (Aug. 2012). “Non-dimensional scaling of tidal stream turbines”. In: *Energy* 44.1, pp. 820–829. ISSN: 03605442. DOI: 10.1016/j.energy.2012.05.010.

Mechanicalc (2025). *Bolt Pattern Force Distribution*. Accessed July 2025. URL: https://mechanicalc.com/reference/bolt-pattern-force-distribution.

Mei, Y., F. Jing, Q. Lu, and B. Guo (Sept. 2024). “Experimental study on power characteristics of a horizontal-axis tidal turbine under pitch motion”. In: *Ocean Engineering* 307, p. 118184. ISSN: 00298018. DOI: 10.1016/j.oceaneng.2024.118184.

Milne, I., A. Day, R. Sharma, and R. Flay (Mar. 2013). “Blade loads on tidal turbines in planar oscillatory flow”. In: *Ocean Engineering* 60, pp. 163–174. ISSN: 00298018. DOI: 10.1016/j.oceaneng.2012.12.027.

Mohd Badrul Salleh Noorfazreena M. Kamaruddin, Z. M.-K. (Dec. 2019). “Savonius hydrokinetic turbines for a sustainable river-based energy extraction: A review of the technology and potential applications in Malaysia”. In: *Sustainable Energy Technologies and Assessments* 36, p. 100554. DOI: 10.1016/j.seta.2019.100554.

Montgomerie, B. (2004). *Methods for Root Effects, Tip Effects and Extending the Angle of Attack Range to 6180, With Application to Aerodynamics for Blades on Wind Turbines and Propellers*. Technical Report. FOI, Swedish Defence Research Agency. URL: https://foi.se/en/foi/reports/report-summary.html?reportNo=FOI-R--1305--SE.

Multon, B. (2012). *Marine Renewable Energy Handbook*. Wiley.

Munson, B. R., A. P. Rothmayer, T. H. Okiishi, and W. W. Huebsch (May 2012). *Fundamentals of Fluid Mechanics*. 7th ed. Wiley.

Muratoglu, A., R. Tekin, and Ö. F. Ertuğrul (Dec. 9, 2020). “Hydrodynamic optimization of high-performance blade sections for stall regulated hydrokinetic turbines using Differential Evolution Algorithm”. In: *Ocean Engineering* 220, p. 108389. DOI: 10.1016/j.oceaneng.2020.108389.

Muratoglu and Yuce (2015). “Performance analysis of hydrokinetic turbine blade sections”. In: *Advances in Renewable Energy* 2.

Mycek, P., B. Gaurier, G. Germain, G. Pinon, and E. Rivoalen (June 2014). “Experimental study of the turbulence intensity effects on marine current turbines behaviour. Part I: One single turbine”. In: *Renewable Energy* 66, pp. 729–746. ISSN: 09601481. DOI: 10.1016/j.renene.2013.12.036.

NASA Glenn Research Center (2023). *Shape Effects on Drag*. Accessed: July 2025. URL: https://www1.grc.nasa.gov/beginners-guide-to-aeronautics/shape-effects-on-drag/.

NASA OpenVSP (2024). *Open Vehicle Sketch Pad (OpenVSP)*. Accessed: 2024-03-03. URL: https://openvsp.org/.

National Renewable Energy Laboratory (2025). *OpenFAST for Marine Energy Technologies*. URL: https://www.nrel.gov/water/open-fast.

Neill, S. P., A. Angeloudis, P. E. Robins, I. Walkington, and S. L. Ward (May 2018a). *Tidal range energy resource and optimization: Past perspectives and future challenges*. Tech. rep. DOI: 10.1016/j.renene.2018.05.007.

Neill, S. P. and M. R. Hashemi (2018b). “Tidal Energy”. In: *Fundamentals of Ocean Renewable Energy: Generating Electricity from the Sea*. Academic Press. Chap. 3, pp. 47–81.

Newman, J. N. (Jan. 1977). *Marine Hydrodynamics*. The MIT Press. DOI: 10.7551/mitpress/4443.001.0001.

Nuernberg, M. and L. Tao (Nov. 2018). “Experimental study of wake characteristics in tidal turbine arrays”. In: *Renewable Energy* 127, pp. 168–181. ISSN: 09601481. DOI: 10.1016/j.renene.2018.04.053.

Orbital Marine Power (Oct. 2024). *O2-X*. Accessed: 2024-10-26. URL: https://www.orbitalmarine.com/technology/.

Ordonez-Sanchez, S., M. Allmark, K. Porter, R. Ellis, C. Lloyd, I. Santic, T. O’Doherty, and C. Johnstone (Jan. 24, 2019). “Analysis of a Horizontal-Axis Tidal Turbine Performance in the Presence of Regular and Irregular Waves Using Two Control Strategies”. In: *Energies* 12.3, p. 367. ISSN: 1996-1073. DOI: 10.3390/en12030367.

Ouro, P., P. Dené, P. Garcia-Novo, T. Stallard, Y. Kyozuda, and P. Stansby (Sept. 7, 2022). “Power density capacity of tidal stream turbine arrays with horizontal and vertical axis turbines”. In: *Journal of Ocean Engineering and Marine Energy* 9.2, pp. 203–218. DOI: 10.1007/s40722-022-00257-8.

Ozturk, M., N. C. Bezir, and N. Ozek (2009). “Hydropower–water and renewable energy in Turkey: Sources and policy”. In: *Renewable and Sustainable Energy Reviews* 13.3, pp. 605–615. DOI: 10.1016/j.rser.2007.11.008.

Payne, G. S., T. Stallard, and R. Martinez (July 2017). “Design and manufacture of a bed supported tidal turbine model for blade and shaft load measurement in turbulent flow and waves”. In: *Renewable Energy* 107, pp. 312–326. ISSN: 09601481. DOI: 10.1016/j.renene.2017.01.068.

Pitas, I. and A. N. Venetsanopoulos (1990). “Median Filters”. In: *Nonlinear Digital Filters*. Vol. 84. The Springer International Series in Engineering and Computer Science. Springer, pp. 63–116. DOI: https://doi.org/10.1007/978-1-4757-6017-0_4.

Polagye, B. L., J. Epler, and J. Thomson (Sept. 2010). “Limits to the predictability of tidal current energy”. In: *Proceedings of the 2014 Oceans Conference* 77, pp. 1–9. DOI: 10.1109/oceans.2010.5664588.

Porter, K. E., S. E. Ordonez-Sanchez, R. E. Murray, M. Allmark, C. M. Johnstone, T. O’Doherty, A. Mason-Jones, D. A. Doman, and M. J. Pegg (Feb. 2020). “Flume testing of passively adaptive composite tidal turbine blades under combined wave and current loading”. In: *Journal of Fluids and Structures* 93, p. 102825. ISSN: 08899746. DOI: 10.1016/j.jfluidstructs.2019.102825.

Prandtl, L. (1921). *Applications of Modern Hydrodynamics to Aeronautics*. Tech. rep. NACA Report No. 116. Translated from the original German publication. Washington, DC: National Advisory Committee for Aeronautics. URL: https://ntrs.nasa.gov/citations/19930091180.

REN21 (2024). *Renewables Global Status Report 2024*. Accessed: 2024-11-14. URL: https://www.ren21.net/gsr-2024/.

Ross, H. and B. Polagye (June 2020). “An experimental assessment of analytical blockage corrections for turbines”. In: *Renewable Energy* 152, pp. 1328–1341. ISSN: 09601481. DOI: 10.1016/j.renene.2020.01.135.

RS Components Nederland (2025). *RS Online Webwinkel*. Accessed: 2025-06-24. URL: https://nl.rs-online.com/web/.

Schmitt, P., S. Fu, I. Benson, G. Lavery, S. Ordoñez-Sanchez, C. Frost, C. Johnstone, and L. Kregting (Aug. 24, 2022). “A Comparison of Tidal Turbine Characteristics Obtained from Field and Laboratory Testing”. In: *Journal of Marine Science and Engineering* 10.9, p. 1182. ISSN: 2077-1312. DOI: 10.3390/jmse10091182.

Selig, M. and B. McGranahan (2012). “Wind Tunnel Aerodynamic Tests of Six Airfoils for Use on Small Wind Turbines”. In: *42nd AIAA Aerospace Sciences Meeting and Exhibit*. DOI: 10.2514/6.2004-1188.

Seo, J., S.-J. Lee, W.-S. Choi, S. T. Park, and S. H. Rhee (Nov. 2016). “Experimental study on kinetic energy conversion of horizontal axis tidal stream turbine”. In: *Renewable Energy* 97, pp. 784–797. ISSN: 09601481. DOI: 10.1016/j.renene.2016.06.041.

El-Shahat, S. A. (2020). “Investigation of parameters affecting horizontal axis tidal current turbines modeling by blade element momentum theory”. In: *Ocean Engineering*.

Shahsavarifard, M., E. L. Bibeau, and V. Chatoorgoon (Mar. 2015). “Effect of shroud on the performance of horizontal axis hydrokinetic turbines”. In: *Ocean Engineering* 96, pp. 215–225. ISSN: 00298018. DOI: 10.1016/j.oceaneng.2014.12.006.

Shi, W., M. Atlar, R. Norman, B. Aktas, and S. Turkmen (Oct. 2016). “Numerical optimization and experimental validation for a tidal turbine blade with leading-edge tubercles”. In: *Renewable Energy* 96, pp. 42–55. ISSN: 09601481. DOI: 10.1016/j.renene.2016.04.064.

SIMEC Atlantis Energy (Sept. 26, 2024). *MEYGEN - SAE Renewables*. URL: https://saerenewables.com/tidal-stream/meygen/.

Slama, M. et al. (Aug. 2021). “Turbine design dependency to turbulence: An experimental study of three scaled tidal turbines”. In: *Ocean Engineering* 234, p. 109035. ISSN: 00298018. DOI: 10.1016/j.oceaneng.2021.109035.

Snel, H., R. Houwink, and W. J. Piers (1992). “Sectional Prediction of 3D Effects for Separated Flow on Rotating Blades”. In: *Proceedings of the European Community Wind Energy Conference*. Lübeck - Travemünde.

Song, M.-S., M.-C. Kim, I.-R. Do, S.-H. Rhee, J.-H. Lee, and B.-S. Hyun (Sept. 30, 2012). “Numerical and experimental investigation on the performance of three newly designed 100 kW-class tidal current turbines”. In: *International Journal of Naval Architecture and Ocean Engineering* 4.3, pp. 241–255. ISSN: 2092-6782. DOI: 10.3744/JNAOE.2012.4.3.241.

Stallard, T., T. Feng, and P. Stansby (Apr. 2015). “Experimental study of the mean wake of a tidal stream rotor in a shallow turbulent flow”. In: *Journal of Fluids and Structures* 54, pp. 235–246. ISSN: 08899746. DOI: 10.1016/j.jfluidstructs.2014.10.017.

Subramanya, R., T. Ravikumar, G. Gnaendra Reddy, K. Manjunatha, and S. Madhusudhana (2020). “Design of wind blades for the development of low-power wind turbines using Betz and Schmitz methods”. In: *Advances in Materials and Processing Technologies* 6.4, pp. 357–376. DOI: 10.1080/2374068X.2020.1833605.

Tangler, J. L. and D. M. Somers (Jan. 1, 1995). *NREL airfoil families for HAWTs*. DOI: 10.2172/10106095.

Tian, W., Z. Mao, and H. Ding (Nov. 2018). “Design, test and numerical simulation of a low-speed horizontal axis hydrokinetic turbine”. In: *International Journal of Naval Architecture and Ocean Engineering* 10.6, pp. 782–793. ISSN: 20926782. DOI: 10.1016/j.ijnaoe.2017.10.006.

Towing tank No.1 (2025). URL: https://www.tudelft.nl/me/over/afdelingen/maritime-and-transport-technology/research/ship-hydromechanics/facilities/towing-tank-no-1 (visited on 01/23/2025).

Traub, L. W. (2019). “Efficient low-Reynolds-number airfoils”. In: *Journal of Aircraft* 56.4, pp. 1524–1532. DOI: 10.2514/1.C035515.

UNFCCC (2024). *The Paris Agreement*. Accessed: 2024-10-26. URL: https://unfccc.int/process-and-meetings/the-paris-agreement.

Vennell, R. (July 2013). “Exceeding the Betz limit with tidal turbines”. In: *Renewable Energy* 55, pp. 277–285. ISSN: 09601481. DOI: 10.1016/j.renene.2012.12.016.

Viterna, L. A. and D. C. Janetzke (1982). *Theoretical and Experimental Power From Large Horizontal-Axis Wind Turbines*. Technical Report. NASA. DOI: 10.2172/6763041.

Vogel, C. and R. Willden (Sept. 2017). “Multi-rotor tidal stream turbine fence performance and operation”. In: *International Journal of Marine Energy* 19, pp. 198–206. ISSN: 22141669. DOI: 10.1016/j.ijome.2017.08.005.

Wang, D., M. Atlar, and R. Sampson (Mar. 1, 2007). “An experimental investigation on cavitation, noise, and slipstream characteristics of ocean stream turbines”. In: *Proceedings of the Institution of Mechanical Engineers, Part A: Journal of Power and Energy* 221.2, pp. 219–231. ISSN: 0957-6509, 2041-2967. DOI: 10.1243/09576509JPE310.

Watanabe, S., M. M. Kamra, and C. Hu (June 2023). “An experimental study of surface wave effects on two interacting tidal turbines”. In: *Journal of Marine Science and Technology* 28.2, pp. 387–398. ISSN: 0948-4280, 1437-8213. DOI: 10.1007/s00773-023-00929-6.

Whelan, J. I. and T. J. Stallard (2011). “Arguments for modifying the geometry of a scale model rotor”. In: *Proceedings of the 9th European Wave and Tidal Energy Conference (EWTEC)*. EWTEC.

Wilden, R. H. J. et al. (Sept. 2023). “Tidal Turbine Benchmarking Project: Stage I - Steady Flow Blind Predictions”. In: *Proceedings of the 15th European Wave and Tidal Energy Conference*. Vol. 15. EWTEC. Preprint, NREL/CP-5700-86715, National Renewable Energy Laboratory, Golden, CO. Bilbao, Spain: European Wave and Tidal Energy Conference. DOI: 10.36688/ewtec-2023-553.

Yadav, P. K., A. Kumar, and S. Jaiswal (Jan. 13, 2023). “A critical review of technologies for harnessing the power from flowing water using a hydrokinetic turbine to fulfill the energy need”. In: *Energy Reports* 9, pp. 2102–2117. DOI: 10.1016/j.egyr.2023.01.033.

Yuce, M. I. and A. Muratoglu (2015). “Hydrokinetic energy conversion systems: A technology status review”. In: *Renewable and Sustainable Energy Reviews* 43, pp. 72–82. DOI: 10.1016/j.rser.2014.10.037.

Zhang, Y., W. Zang, J. Zheng, L. Cappietti, J. Zhang, Y. Zheng, and E. Fernandez-Rodriguez (Mar. 2021). “The influence of waves propagating with the current on the wake of a tidal stream turbine”. In: *Applied Energy* 290, p. 116729. ISSN: 03062619. DOI: 10.1016/j.apenergy.2021.116729.

Zhong, W., T. Wang, W. Z. Shen, and W. J. Zhu (2024). “A Function Improving Tip Loss Correction of Blade-Element Momentum Theory for Wind Turbines”. In: *International Journal of Sustainable Energy* 43.1, pp. 2395–2418. DOI: 10.1080/14786451.2024.2352794.

A

Chapter 1 extra figures

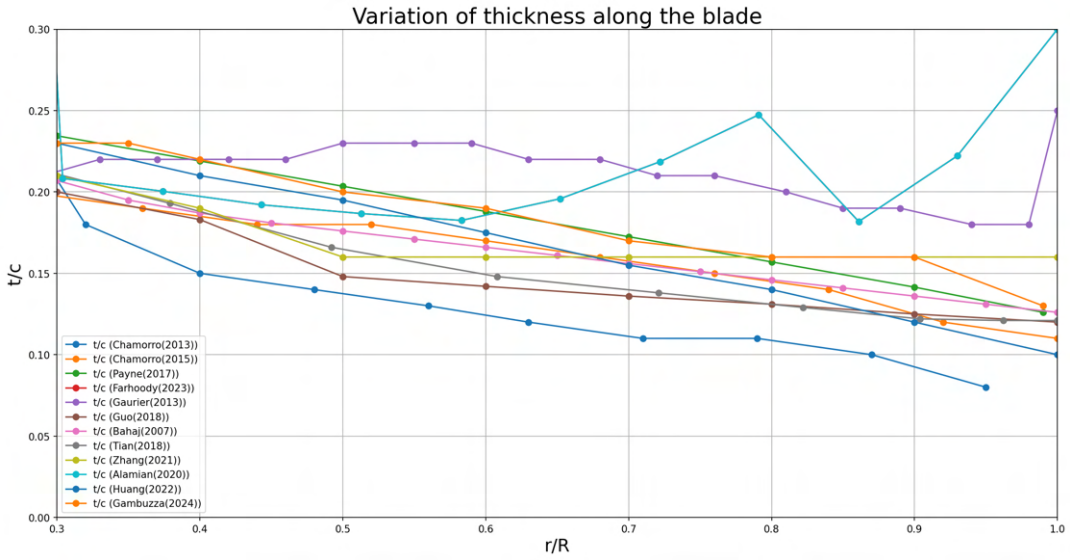

Figure A.1: Zoomed in thickness distribution along the normalized blade radius, for $r/R > 0.3$.

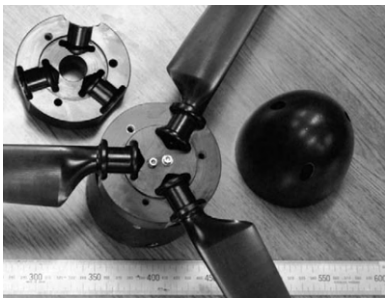

(a) The pitching system of Bahaj et al. (2007).

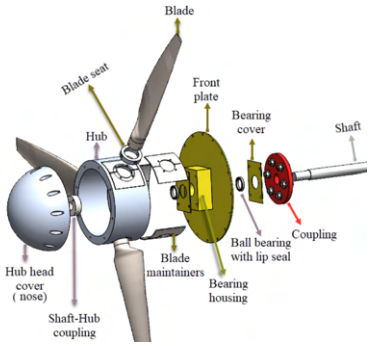

(b) The pitching mechanism of Farhoody et al. (2023).

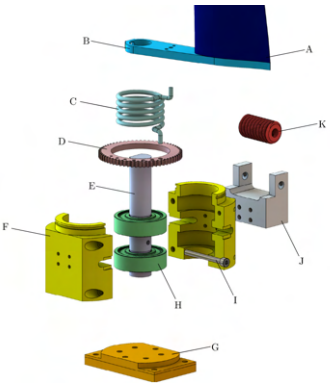

(c) The passive pitching system of Gambuzza et al. (2025).

Figure A.2: Comparison of different design with a circular root section and their pitching systems.

B

Actuator disc code

```python
import numpy as np
import matplotlib.pyplot as plt

# Define a2 fit function (approximating a at the tip)
def a2_fit_function(lmbda):
    a1 = 0.3324
    b = 0.0123
    c = 0.7415
    d = -0.0679
    return a1 + b / (lmbda + c) + d / (lmbda + c)**2

# Define the relationship for a'
def tangential_induction_factor(a):
    denominator = 4 * a - 1
    # Avoid singularities by returning 0 for small denominators
    return np.where(np.abs(denominator) < 1e-3, 0, (1 - 3 * a) / denominator)

def tip_loss_factor(B, R, r, phi):
   f = (B / 2) * (R - r) / (r * np.sin(phi))
   F = (2 / np.pi) * np.arccos(np.exp(-f))
   return F

# Input parameters
B=3 # number of blades
D = 0.74 # Rotor diameter (m)
hub_diameter = 0.12 # Hub diameter (m)
U_infinity = 0.75 # Free-stream velocity (m/s)
lambda_value = 5 # Tip Speed Ratio (TSR)
rho = 1000  # Density of water (kg/m^3)
include_tip_loss = True  # Set to False to disable tip loss
```

Figure B.1: Actuator disc code part 1

```
# Recalculate values
R = D/2  # Rotor radius (m)
omega = lambda_value * U_infinity / R  # Rotational speed (rad/s)
hub_radius = hub_diameter / 2  # Hub radius (m)

# Blade span discretization, excluding hub region
r_R_values = np.linspace(hub_radius / R, 1, 100)  # Radial positions (normalized r/R)
r_values = r_R_values * R  # Actual radial positions

# Calculate lambda_r
lambda_r_values = lambda_value * r_R_values  #local tip speed ratio

# Step 1: Calculate raw a and a'
a_raw = a2_fit_function(lambda_r_values)
a_prime_raw = tangential_induction_factor(a_raw)

# Step 2: Estimate phi and compute tip loss factor
phi_values = np.arctan2(U_infinity * (1 - a_raw), omega * r_values * (1 + a_prime_raw))
F_values = tip_loss_factor(B, R, r_values, phi_values)

# Step 3: Apply tip loss or not based on toggle
if include_tip_loss:
    a_values = F_values * a_raw
    a_prime_values = F_values * a_prime_raw
else:
    a_values = a_raw
    a_prime_values = a_prime_raw
```

Figure B.2: Actuator disc code part 2

```
# Step 4: (Optional) Recompute phi for use in plotting or analysis
phi_values = np.arctan2(U_infinity * (1 - a_values), omega * r_values * (1 + a_prime_values))

# Calculate elemental torque dQ
dr = (R - hub_radius) / len(r_values)  # Width of each annular ring
dQ_values = 4 * rho * U_infinity * a_prime_values * (1 - a_values) * np.pi * r_values**3 * omega * dr

# Total torque Q
total_torque = np.sum(dQ_values)

# Calculate power and power coefficient
power_extracted = total_torque * omega  # P = Q * Omega
swept_area = np.pi * R**2  # Swept area
effective_swept_area = np.pi * R**2 - np.pi * hub_radius**2  # Effective swept area, excluding hub
power_available = 0.5 * rho * swept_area * U_infinity**3
Power_available_minus_hub = 0.5 * rho * effective_swept_area * U_infinity**3
cp = power_extracted / power_available
cp_minus_hub = power_extracted / Power_available_minus_hub
# Plot the results
plt.figure(figsize=(10, 6))

# Plot a vs r/R
plt.plot(r_R_values, a_values, label="a (Axial Induction Factor)", color="blue")
# Plot a' vs r/R
plt.plot(r_R_values, a_prime_values, label="a' (Tangential Induction Factor)", color="orange")

plt.title(f"Induction factors (a and a') vs r/R for λ = {lambda_value}", fontsize=20)
plt.xlabel("r/R (Normalized blade span)", fontsize=18)
plt.ylabel("Induction factors", fontsize=18 )
plt.legend(fontsize=16)
plt.grid()
plt.ylim(0, 0.45)
plt.show()
```

Figure B.3: Actuator disc code part 3

```
# Print results
print(f"Total Torque (Q): {total_torque:.2f} Nm")
print(f"Power Extracted (P): {power_extracted:.2f} W")
print(f"Available Power (P_available): {power_available:.2f} W")
print(f"Power Coefficient (Cp): {cp:.3f}")
#print(f"Power Coefficient effective (Cp): {cp_minus_hub:.3f}")
# maximum expected Cp
d = 0.6083
e = 0.3421
f = 1.5206
g = -0.2383
Max_Cp = d - e * np.exp(-f * lambda_value) + g / (lambda_value + 1)
#print(f"Maximum_Cp: {Max_Cp:.3f}")
print(f"Rotational speed: {omega:.3f} rad/s" )
print(f"Rotational speed: {omega*60/(2*np.pi):.1f} rpm" )

# Calculate elemental thrust dT
dT_values = 4 * np.pi * rho * U_infinity**2 * a_values * (1 - a_values) * r_values * dr
dT_values2 = 4* a_prime_values *(1+a_prime_values)* rho* omega**2 *r_values**3 *np.pi * dr

# Total thrust T
total_thrust = np.sum(dT_values)
total_thrust2 = np.sum(dT_values2)
# Calculate thrust coefficient (Ct)
ct = total_thrust / (0.5 * rho * np.pi * R**2 * U_infinity**2)
T1= 0.9*(0.5 * rho * np.pi * R**2 * U_infinity**2)
print(T1)

# Print results
print(f"Total Thrust (T): {total_thrust:.2f} N")
print(f"Total Thrust2 (T): {total_thrust2:.2f} N")
print(f"Thrust Coefficient (Ct): {ct:.3f}")
```

Figure B.4: Actuator disc code part 4

C

Working drawings

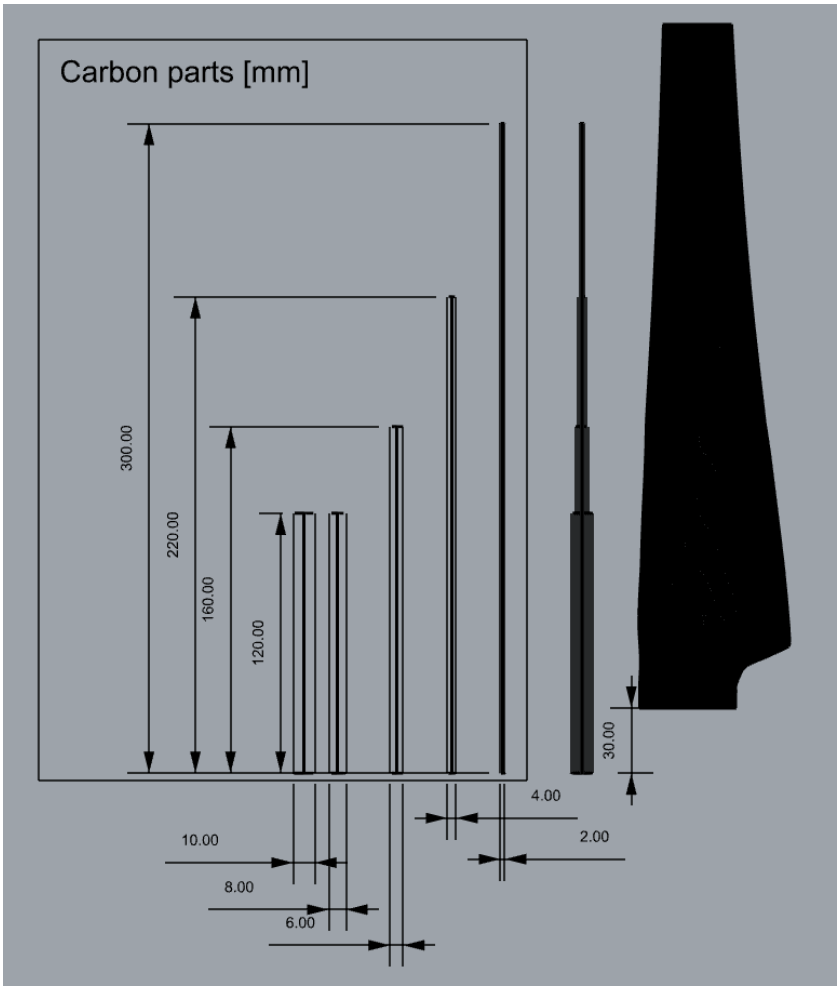

Figure C.1: Carbon rod dimensions.

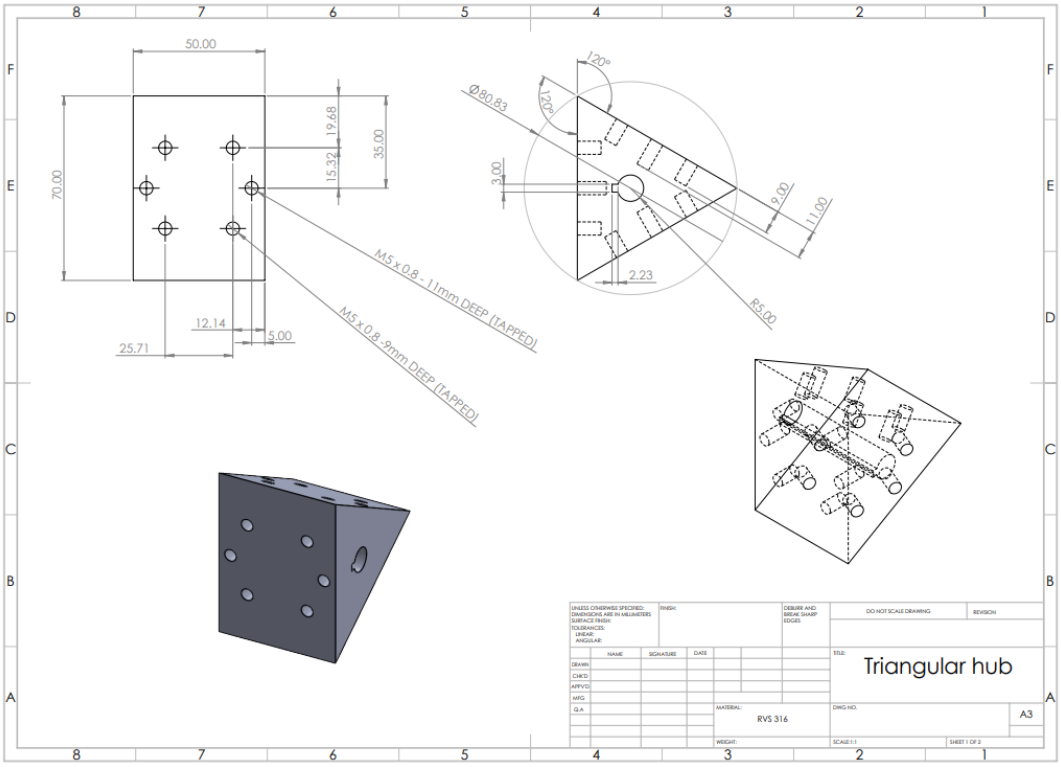

Figure C.2: Working drawing triangular hub.

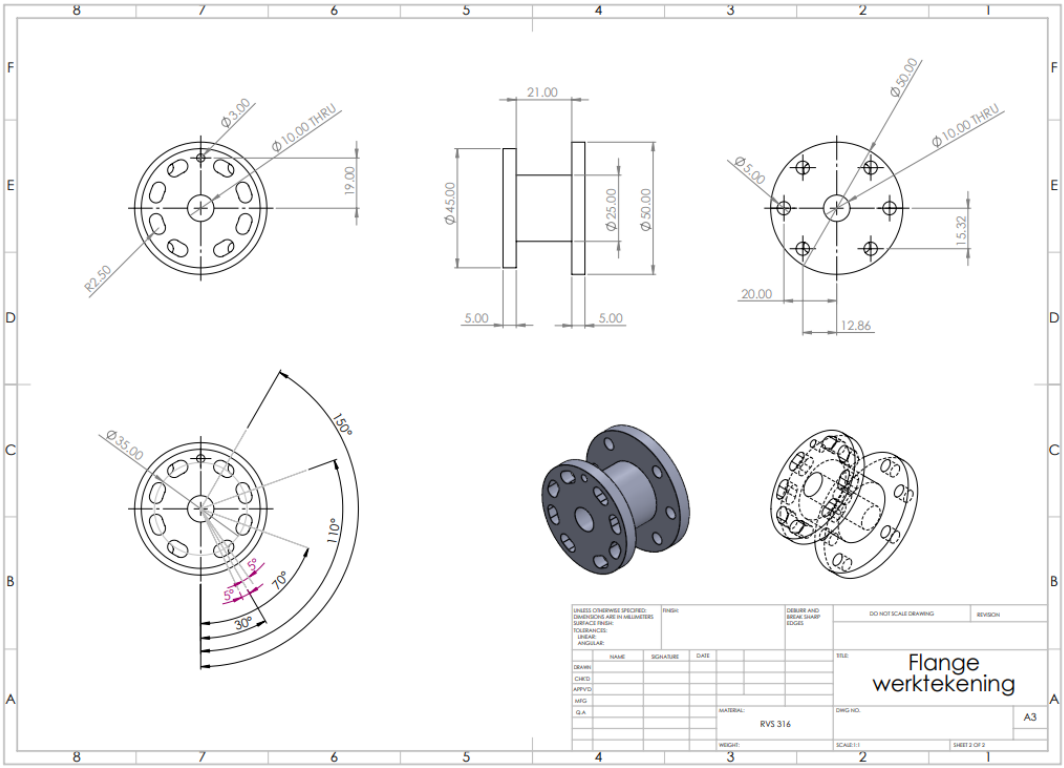

Figure C.3: Working drawing flange.

D

Chapter 4 extra figures

Pos [m]	Chord [m]	Twist [deg]	Foil
0.054	0.045	34.473	Circular foil
0.063	0.045	32.137	Circular foil
0.071	0.054	29.800	Interpolated 64
0.082	0.076	25.221	NACA 63828
0.092	0.074	21.573	NACA 63824
0.106	0.069	19.045	NACA 63824
0.119	0.063	16.710	Interpolated 23.25
0.133	0.058	14.892	Interpolated 22.5
0.146	0.054	13.133	Interpolated 21.75
0.160	0.050	11.585	NACA 63821
0.173	0.046	10.211	Interpolated 19.5
0.187	0.044	9.177	NACA 63818
0.201	0.041	8.231	NACA 63818
0.215	0.039	7.396	NACA 63818
0.229	0.037	6.652	NACA 63818
0.243	0.035	5.987	NACA 63818
0.257	0.033	5.460	Interpolated t16.5
0.271	0.032	5.100	NACA 63815
0.285	0.031	4.750	NACA 63815
0.299	0.029	4.420	NACA 63815
0.313	0.028	4.096	NACA 63815
0.327	0.028	3.865	Interpolated t13.5
0.341	0.027	3.654	NACA 63812
0.355	0.026	3.500	NACA 63812
0.370	0.025	3.250	NACA 63812

Table D.1: Blade geometry output from QBlade, first trial (3 blades, 0.05 m hub radius)

E

Chapter 5 extra figures

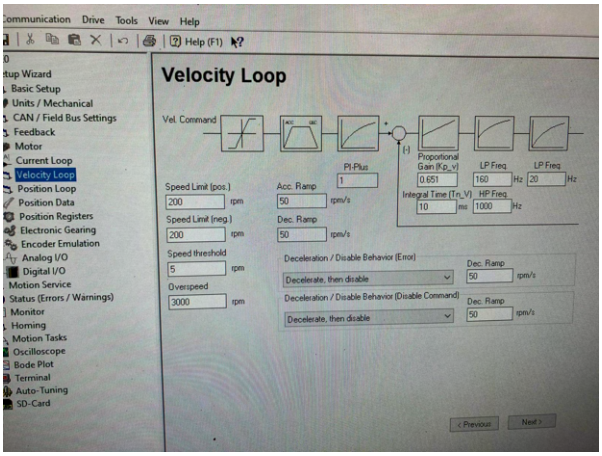

Figure E.1: PI control panel with used values.

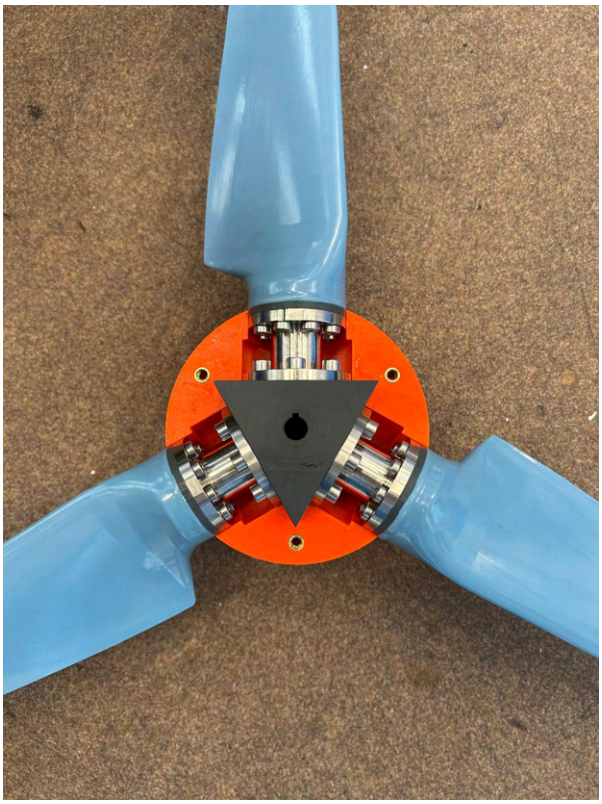

Figure E.2: Hub connection placed into the orange transition piece.

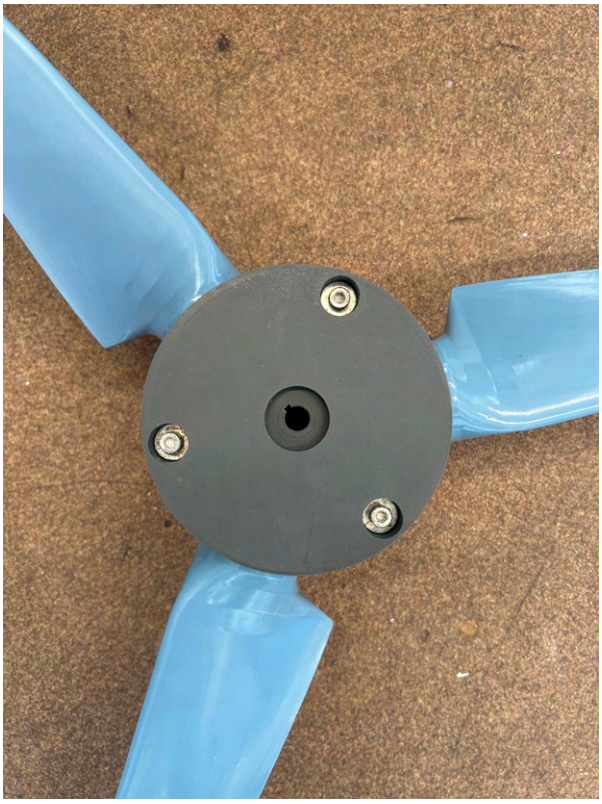

Figure E.3: Enclosed hub connection with second transition piece.